UNIVERSITY OF AMSTERDAM

UvA-DARE (Digital Academic Repository)

The R136 star cluster dissected with Hubble Space Telescope/STIS. I

Far-ultraviolet spectroscopic census and the origin of He II λ1640 in young star clusters

Crowther, P.A.; Caballero-Nieves, S.M.; Bostroem, K.A.; Maíz Apellániz, J.; Schneider, F.R.N.; Walborn, N.R.; Angus, C.R.; Brott, I.; Bonanos, A.; de Koter, A.; de Mink, S.E.; Evans, C.J.; Gräfener, G.; Herrero, A.; Howarth, I. D.; Langer, N.; Lennon, D.J.; Puls, J.; Sana, H.; Vink, J.S.

Link to publication

The R136 star cluster dissected with *Hubble Space Telescope*/STIS. I. Far-ultraviolet spectroscopic census and the origin of He II λ1640 in young star clusters

Paul A. Crowther,[1][*] S. M. Caballero-Nieves,[1] K. A. Bostroem,[2,3] J. Maíz Apellániz,[4]
F. R. N. Schneider,[5,6] N. R. Walborn,[2] C. R. Angus,[1,7] I. Brott,[8] A. Bonanos,[9]
A. de Koter,[10,11] S. E. de Mink,[10] C. J. Evans,[12] G. Gräfener,[13] A. Herrero,[14,15]
I. D. Howarth,[16] N. Langer,[6] D. J. Lennon,[17] J. Puls,[18] H. Sana[2,11] and J. S. Vink[13]

Affiliations are listed at the end of the paper

ABSTRACT

We introduce a *Hubble Space Telescope* (*HST*)/Space Telescope Imaging Spectrograph (STIS) stellar census of R136a, the central ionizing star cluster of 30 Doradus. We present low resolution far-ultraviolet STIS spectroscopy of R136 using 17 contiguous 52 arcsec × 0.2 arcsec slits which together provide complete coverage of the central 0.85 parsec (3.4 arcsec). We provide spectral types of 90 per cent of the 57 sources brighter than $m_{F555W} = 16.0$ mag within a radius of 0.5 parsec of R136a1, plus 8 additional nearby sources including R136b (O4 If/WN8). We measure wind velocities for 52 early-type stars from C IV λλ1548–51, including 16 O2–3 stars. For the first time, we spectroscopically classify all Weigelt and Baier members of R136a, which comprise three WN5 stars (a1–a3), two O supergiants (a5–a6) and three early O dwarfs (a4, a7, a8). A complete Hertzsprung–Russell diagram for the most massive O stars in R136 is provided, from which we obtain a cluster age of $1.5^{+0.3}_{-0.7}$ Myr. In addition, we discuss the integrated ultraviolet spectrum of R136, and highlight the central role played by the most luminous stars in producing the prominent He II λ1640 emission line. This emission is totally dominated by very massive stars with initial masses above ∼100 M$_\odot$. The presence of strong He II λ1640 emission in the integrated light of very young star clusters (e.g. A1 in NGC 3125) favours an initial mass function extending well beyond a conventional upper limit of 100 M$_\odot$. We include montages of ultraviolet spectroscopy for Large Magellanic Cloud O stars in the appendix. Future studies in this series will focus on optical STIS medium resolution observations.

Key words: stars: early-type – stars: massive – stars: winds, outflows – Magellanic Clouds – galaxies: star clusters: individual: R136a.

1 INTRODUCTION

The formation of massive stars remains an unsolved problem in astrophysics. This is especially challenging since very massive stars (VMS, ≥100 M$_\odot$) are usually located within young massive star clusters (≥10^4 M$_\odot$) with small core radii ($r_c \sim 0.1$–0.2 pc; Portegies Zwart, McMillan & Gieles 2010). The short lifetime of such stars (2–3 Myr; Yusof et al. 2013) restricts suitable Milky Way star clusters to only a handful, including the Arches (Martins et al. 2008) and NGC 3603 (Schnurr et al. 2008), both of which are

highly reddened. Therefore, observations of young star clusters at ultraviolet (UV) wavelengths – corresponding to the peak output of hot, luminous stars – are largely restricted to extragalactic cases.

R136 was included in the census of optically bright Magellanic Cloud stars by Feast, Thackeray & Wesselink (1960), and subsequently resolved into three components, a, b and c (Feitzinger et al. 1980), with component a subsequently shown to be multiple (Weigelt & Baier 1985). R136a is the closest example of an extragalactic young massive star cluster (Hunter, Shaya & Holtzman 1995). It is the central cluster of the NGC 2070 complex within the 30 Doradus star-forming region in the Large Magellanic Cloud (LMC; Massey & Hunter 1998; Doran et al. 2013), and is relatively lightly reddened, facilitating study at UV wavelengths (de Marchi

[*] E-mail: Paul.crowther@sheffield.ac.uk

et al. 1993). However, the 0.1 pc core radius of R136a (Portegies Zwart et al. 2010; Selman & Melnick 2013) subtends only 0.41 arcsec at the 50 kpc distance to the LMC (Pietrzyński et al. 2013), which led to the cluster at one time being mistaken for a $\geq$1000 M$_\odot$ star (Cassinelli, Mathis & Savage 1981; Feitzinger, Hanuschik & Schmidt-Kaler 1983), although Walborn (1973) had earlier predicted that R136a would have a structure analogous to the core of NGC 3603. Consequently, observations at high spatial resolution are required to resolve individual stars within the core of R136a, requiring either *Hubble Space Telescope* (*HST*) or large ground-based telescopes with adaptive optics (VLT/MAD; Campbell et al. 2010).

The star formation history of NGC 2070 has recently been investigated by Cignoni et al. (2015) using Hubble Tarantula Treasury Project imaging, revealing an upturn in star formation ∼7 Myr ago, peaking 2–3 Myr ago, and a total stellar mass of 9×10^4 M$_\odot$ assembled within 20 pc of R136. The mass function for intermediate- and low-mass stars in R136 have been obtained from *HST* imaging (Hunter et al. 1995; de Marchi et al. 2011). However, the colour/reddening degeneracy of hot massive stars at UV and optical wavelengths necessitates spectroscopy for robust physical properties, and in turn, masses, measuring present-day mass functions (though see Maíz Apellániz et al. 2014). To date, Koornneef & Mathis (1981) and Vacca et al. (1995) have presented UV scans across NGC 2070 with the International Ultraviolet Explorer (IUE), while UV spectroscopy of individual stars of R136a has been limited to the brightest members with *HST*/GHRS (de Koter, Heap & Hubeny 1997, 1998).

Meanwhile, Massey & Hunter (1998) have obtained optical spectroscopy for dozens of stars within NGC 2070 using *HST*/FOS, which revealed large numbers of very early O stars, indicating a young cluster age (<1–2 Myr). More recently Schnurr et al. (2009) used VLT/SINFONI to obtain spatially resolved *K*-band spectroscopy of the brightest sources, namely R136a1, a2, a3 and c, which are WN-type emission-line stars. Analysis of the VLT and *HST* spectroscopy plus VLT/MAD imaging led Crowther et al. (2010) to conclude that such stars possess very high (initial) stellar masses of 160–320 M$_\odot$, results largely supported by Bestenlehner et al. (2011) and Hainich et al. (2014).

The existence of such high-mass stars in R136 challenges the previously accepted ∼150 M$_\odot$ upper stellar mass limit (Figer 2005), unless they are products of stellar mergers (Banerjee, Kroupa & Oh 2012; Schneider et al. 2014b). If such stars are indeed merger remnants one would expect younger apparent ages for this with respect to lower mass stars, and differences in the present day mass function with respect to a Salpeter slope (Schneider et al. 2014b; Schneider et al. 2015). Massey & Hunter (1998) suggested that the mass function of R136 is normal, although their study only included a subset of the brightest stars in the vicinity of R136a.

A census of the hot, luminous stars in R136a with Space Telescope Imaging Spectrograph (STIS) is the focus of the present series of papers. We discuss the suitability of UV spectroscopy for spectral classification of O stars, based in part upon spectroscopic data sets in the usual blue visual wavelength range. Wind velocities for O stars can uniquely be obtained from P Cygni profiles in the far-UV (e.g. Groenewegen, Lamers & Pauldrach 1989; Prinja, Barlow & Howarth 1990). Comparisons of empirical (reduced) wind momenta[1] with theoretical predictions usually rely on approximate v_∞ calibrations (e.g. Lamers, Snow & Lindholm 1995). Indeed,

high-quality far-UV spectroscopy has been restricted to relatively few LMC O stars to date (Prinja & Crowther 1998; Walborn et al. 1995; Massey et al. 2005). One byproduct of this study is a calibration of wind velocities for (mostly) early O dwarfs at the ∼0.5 Z$_\odot$ metallicity of the LMC.

In the first study in this series, we introduce our new STIS observations of R136a in Section 2. We present and analyse UV STIS/Multi-Anode Microchannel Array (MAMA) spectroscopy of individual stars in Section 3, including approximate spectral types and estimates of terminal wind velocities. An UV spectral atlas of LMC O stars is compiled using literature spectra, in a few instances complemented with new STIS/Charged Couple Device (CCD) spectroscopic data sets to provide templates of missing spectral types. The current data set also allows the contributions from individual stars to its integrated UV spectrum to be quantified. This is discussed in Section 4, of relevance for other young massive star clusters in the local universe (e.g. Chandar, Leitherer & Tremonti 2004; Leitherer et al. 2011) and the integrated rest-frame UV spectrum of high-redshift star-forming galaxies (e.g. Shapley et al. 2003). Finally, brief conclusions are drawn in Section 5.

2 OBSERVATIONS

Here we present our new long-slit *HST* STIS observations of R136, and use of archival WFC3/UVIS imaging discussed by de Marchi et al. (2011).

2.1 UV spectroscopy

We have obtained UV STIS/G140L spectroscopy using the far-UV MAMA detector and a 52 arcsec × 0.2 arcsec slit at 17 contiguous pointings in R136, identified by their position within the cluster, namely SE9, SE8, ...SE1, NW1, ...NW7, NW8 (Fig. 1). The spectral coverage of the G140L grating is $\lambda\lambda$1150–1700 Å, with a pixel scale of 0.6 Å pixel^{-1}, and notional point source resolving power of 1250 at $\lambda = 1500$ Å. Since the MAMA plate scale is 0.024 arcsec pixel^{-1}, a slit length of ∼25 arcsec is sampled in all cases. All MAMA exposures were obtained in two visits, 4 and 5 from GO 12465, totalling 6 orbits, as set out in Table 1. All observations were obtained at a fixed position angle 64° (E of N), to ensure that R136a1 and R136a2 lie within the same slit position (NW1) as shown in Fig. 1. For each visit, the nearby isolated star Melnick 34 was acquired using the CCD and F28X50LP aperture, followed by a peakup with the CCD and 52 arcsec × 0.1arcsec aperture, followed by an offset to individual pointings, with two exposures acquired per pointing, the second spatially offset along the slit by 11 pix (0.27 arcsec), with integration times shown in Table 1.

MAMA exposures were combined and extracted using the specialized STISTOOLS package (Bostroem & Proffitt 2011). No automated wavelength correction was made for sources not centred in individual slits, while standard CALSTIS slit loss corrections were applied. Therefore, absolute wavelength scales may be incorrect by up to ±2 pixel (0.56 Å pixel^{-1}) while absolute far-UV fluxes will be underestimated by up to a factor of 2 in extreme cases.

Extractions were also independently made using MULTISPEC (Maíz Apellániz 2005; Knigge et al. 2008) which is particularly suited to the crowded region at the geometric centre of the cluster. Fig. 2 shows 2D spectral data sets for particularly crowded slits NW1 (a1, a2 and a5) and NW3 (a4 and a8), including collapsed spectral images between $\lambda\lambda$1475–1525. MULTISPEC extractions relied upon empirical point spread functions for G140L/MAMA spectroscopy employing the position of individual sources in slits from short

---

[1] Reduced wind momenta $\dot{M}v_\infty R^{1/2}$, where $\dot{M}$ is the mass-loss rate, v_∞ is the terminal wind velocity and R is the stellar radius.
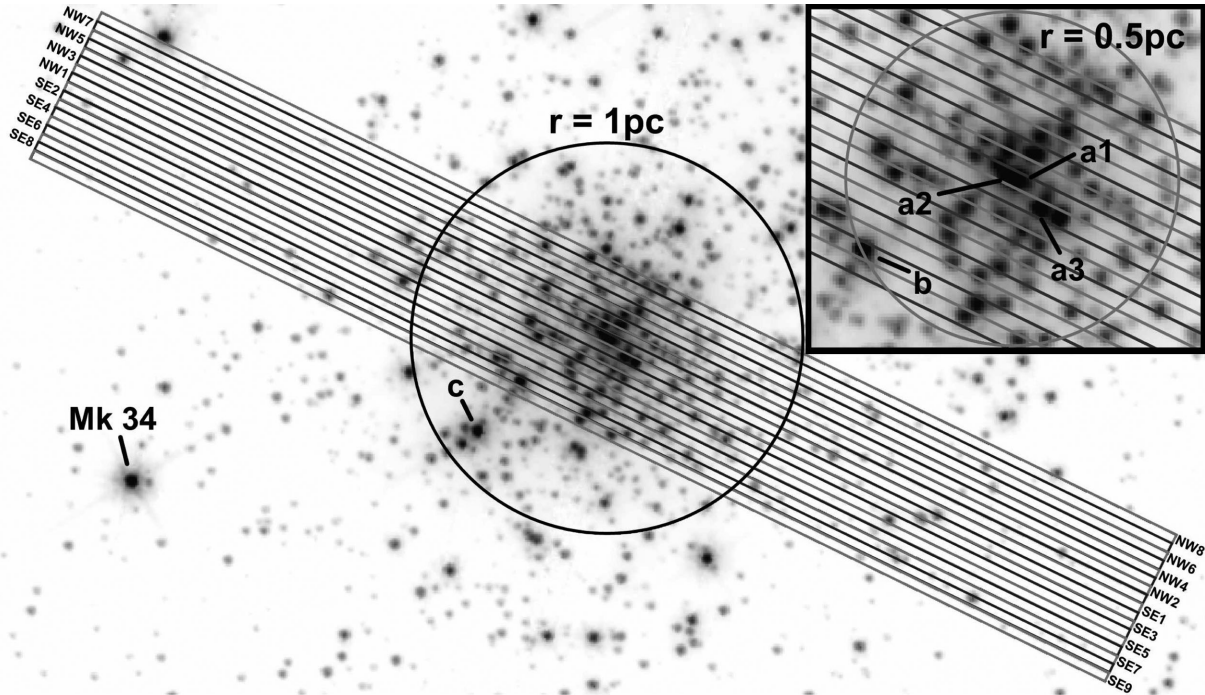
Figure 1. *HST*/STIS slits (52 arcsec × 0.2 arcsec) superimposed upon an F336W WFC3/UVIS image of R136 (de Marchi et al. 2011), oriented with north up and east to left, together with a circle of radius 4.1 arcsec (1 parsec) and identification of the acquisition star Melnick 34. The active slit length for MAMA observations is the central 25 arcsec. The zoom highlights the central region, including identification of individual slits and the integrated R136a cluster (2.05 arcsec radius circle, centred upon R136a1 equivalent to 0.5 parsec at the distance of the LMC).

Table 1. Log of *HST*/STIS spectroscopic observations of R136 from Cycles 19 (GO 12465) and 20 (GO 13052).

GO /visit	Orbits	Target	Detector	Grating /position	PA °	T_{exp} (sec)	Date
12465/1	4	SE9... NW1	CCD	G430M/3936	64	2 × (440–570)	2012 April 6
12465/2	4	SE9...NW1	CCD	G430M/4451	64	2 × (440–570)	2012 April 4
12465/3	4	SE9...NW1	CCD	G430M/4706	64	2 × (440–570)	2012 April 6
12465/4	4	SE9...NW3	MAMA	G140L	64	2 × (400–470)	2012 April 7
12465/5	2	NW4...NW8	MAMA	G140L	64	2 × (470–520)	2012 April 8
12465/6	5	SE9...NW8	CCD	G750M/6581	244	2 × (350–370)	2012 October 23
12465/7	3	NW2...NW8	CCD	G430M/3936	244	2 × 540	2012 October 20
12465/8	3	NW2...NW8	CCD	G430M/4451	244	2 × 540	2012 October 20
12465/9	3	NW2...NW8	CCD	G430M/4706	244	2 × 540	2012 October 20
13052/1	4	SE9...NW1	CCD	G430M/4194	244	2 × (440–570)	2012 October 21
13052/2	3	NW2...NW8	CCD	G430M/4194	64	2 × 540	2013 April 3

exposure *HST* WFC3/UVIS F336W imaging of R136 from 2009 October (for details, see de Marchi et al. 2011). The latter provided wavelength corrections if sources were not centred in individual slits, but a standard slit loss correction is again adopted.

For relatively isolated sources, CALSTIS and MULTISPEC extractions agree extremely well, while the latter approach usually performed better in situations where sources were closely spaced within individual slits. For consistency, spectroscopic data sets presented here were extracted with MULTISPEC, except for R136 H70, 141, 149 for which MULTISPEC extractions were problematic.

2.2 Optical spectroscopy

We have obtained optical STIS spectroscopy using the CCD detector and identical 52 arcsec × 0.2 arcsec slit at identical positions and position angle (or PA + 180°) to the UV spectroscopy, although the coarser plate scale of 0.05 arcsec pixel^{-1} provided complete spatial

coverage of the slit length. In total, two exposures at four grating positions with the G430M grating provided complete blue coverage λλ3793–4849 Å, with a pixel scale of 0.28 Å pixel^{-1}, and point source resolving power of 7700 at λ = 4400 Å. A single grating position with the G750M grating provided λλ6482–7054 Å spectroscopy, with a pixel scale of 0.56 Å pixel^{-1}, and point source resolving power of 6000 at Hα. For all CCD observations, the second exposure was offset spatially along the slit by 7 pixel (0.35 arcsec). Three of the four G430M observations were taken over the course of a few days, with the fourth (G430M/4194) obtained approximately 6 months later to enable to search for low-period binaries. All G750M exposures were taken at a single epoch.

In total, CCD exposures were split between six visits during Cycle 19 (GO 12465, 26 orbits), plus two visits during Cycle 20 (GO 13052, 7 orbits), also set out in Table 1. MULTISPEC and CALSTIS extractions of CCD observations will be the focus of the next paper in this series (Caballero-Nieves et al., in preparation).
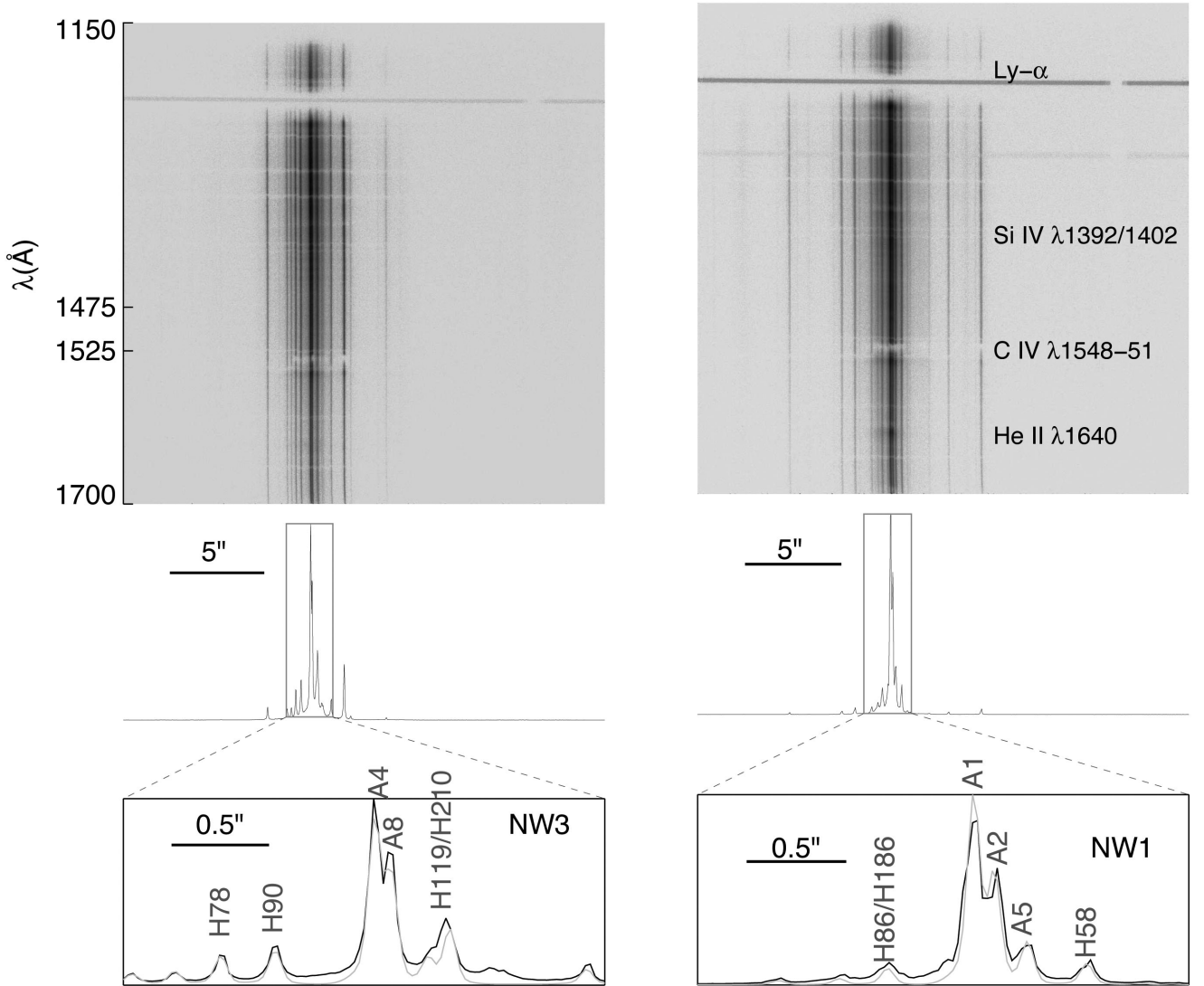
Figure 2. (Top): 2D spectral data set for NW3 (left) and NW1 (right) slits, oriented such that the $\lambda\lambda$1150–1700 dispersion axis runs from top to bottom (horizontal line near top is geocoronal Ly α emission, occulting bar lies to the right of each image) and the (25 arcsec = 6.2 pc) spatial axis is oriented from left (SW) to right (NE). Prominent (stellar plus interstellar) absorption features include Lyα (top) and C IV λ1548–51 (bottom); (centre): collapsed spectral image for NW3 (left) and NW1 (right) between $\lambda\lambda$1475–1525; (bottom) 2.5 arcsec (0.62 pc) zoom of collapsed spectral image for NW3 (left) and NW1 (right) indicating the dense cores, resolving R136a1 and a2, and R136a4 and a8, respectively, together with MULTISPEC fits (faint grey line).

LMC stars that have been observed in the UV and for which reliable optical classifications are available are fairly scarce. Our sample allows 10 stars with robust optical classifications spanning the full O2–O9.5 subtype sequence, which are included here as LMC templates (see Section 3).

2.3 Stellar census of R136

Hunter et al. (1995) have used *HST*/WFPC2 to identify the visually brightest sources in R136, while deeper HST/WFC3 images have been analysed by de Marchi et al. (2011) to derive multicolour photometry. We compare WFPC2 and WFC3/UVIS photometry in F336W, F555W and F814W filters for all sources in common within 10 arcsec (2.4 pc) of R136a1 in Fig. 3. Overall, the earlier WFPC2 results are confirmed by WFC3, albeit with modest systematic offsets of m_{F336W}(WFPC2)–m_{F336W}(WFC3) = +0.15 ± 0.20 mag, m_{F555W}(WFPC2)–m_{F555W}(WFC3) = +0.17 ± 0.21 mag, m_{F814W}(WFPC2)–m_{F814W}(WFC3) = +0.18 ± 0.22 mag. In sources

for which de Marchi et al. (2011) photometry is unavailable, we have substituted Hunter et al. (1995) results to which these offsets have been applied. Overall, agreement between early WFPC2 and new WFC3 photometry is generally very good, with a few notable exceptions – WFC3 photometry from de Marchi et al. (2011) is significantly brighter for R136a1, a2 and a6.

In Table 2, we provide a catalogue of all 55 sources within 2.05 arcsec (0.5 pc) of R136a1 brighter than m_{F555W} = 16.0 mag, while an additional 8 bright sources observed with STIS/MAMA are presented in Table 3. Additional sources brighter than m_{F555W} = 17.0 mag within 4.1 arcsec (1 pc) are listed in Appendix D (Table D1). There is evidence for a non-standard extinction law in 30 Doradus, and significant variation thereof (Maíz Apellániz et al. 2014). Specifically for R136, Doran et al. (2013) favoured $R_V \sim 4.2$ mag for individual stars based on a combination of optical (WFC3/UVIS) and near-IR (VLT/MAD, Campbell et al. 2010) photometry. We have applied CHORIZOS to 41 O stars with WFC3 photometry and approximate spectral types, and obtained good fits in 34 cases,
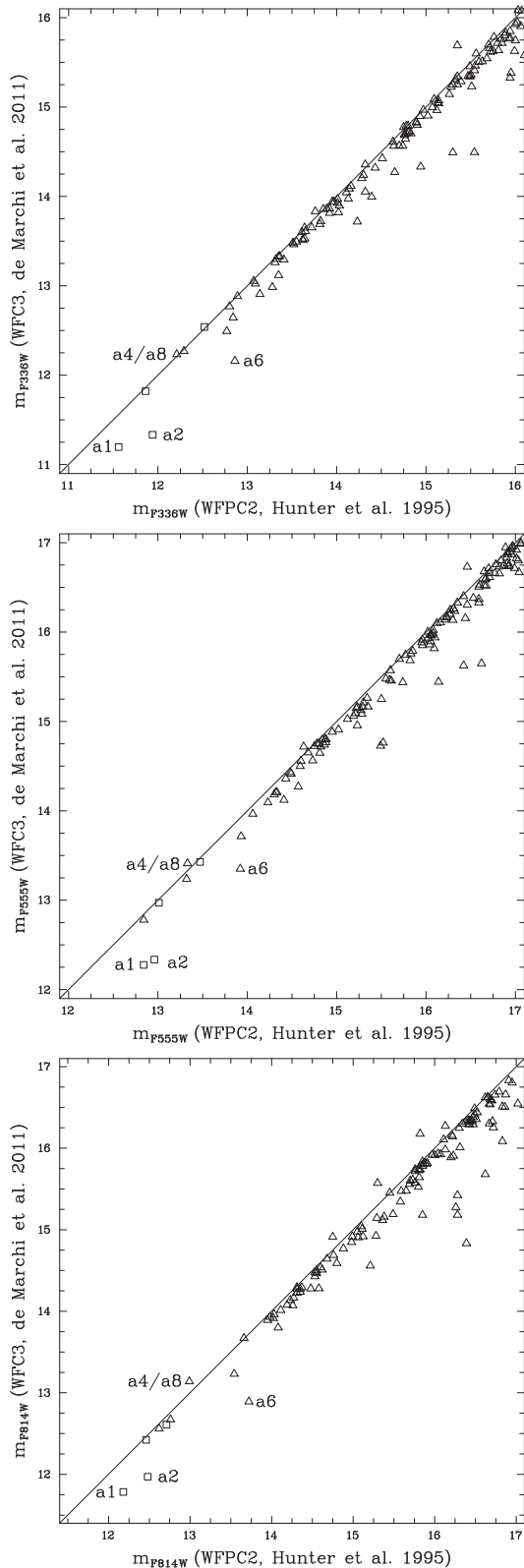
from which average values of $R_{5495} = 4.1 \pm 0.5$ and $A_{\mathrm{F555W}} = 1.72 \pm 0.25$ mag is obtained, in good agreement with the Tatton et al. (2013) near-IR study, for which $A_V = 1.75$ mag was inferred for R136. Here, we adopt tailored extinctions of WN5 stars from Crowther et al. (2010), while for the O stars we adopt a reddening law of $R_{5495} = 4.1$ and individual extinctions based upon temperature dependent F336W–F555W intrinsic colours from multicolour CHORIZOS (Maíz Apellániz 2004):

$$(m_{\mathrm{F336W}} - m_{\mathrm{F555W}})_0 = -1.475 - 0.155(T_{\mathrm{eff}}/10\,000\,)\mathrm{mag},$$

plus $A_{\mathrm{F555W}} = R_{5495}E_{\mathrm{F336W-F555W}}/2.28$ from the Seaton (1979)/Howarth (1983) LMC extinction law, plus an LMC distance modulus of 18.49 mag (Pietrzyński et al. 2013). For stars without UV derived spectral types, we adopt O6 V ($T_{\mathrm{eff}} = 39\,900$ K) for stars brighter than $m_{\mathrm{F555W}} = 16.0$ mag, and O9.5 V ($T_{\mathrm{eff}} = 32\,900$ K) for fainter stars. We adopt $A_{\mathrm{F555W}} = 1.72$ mag for all sources without WFC3 photometry.

Severe crowding results in significant differences in photometry between Hunter et al. (1995) and de Marchi et al. (2011) for some of the brightest sources in the core of R136a. *HST*/WFC3 photometry implies F336W/F555W/F814W flux ratios of 0.88/0.95/0.84 for a2/a1, while *K*-band VLT/SINFONI observations favour a significantly lower ratio of 0.76 (Crowther et al. 2010). From our STIS/MAMA spectroscopy, the 1500 Å flux ratio inferred from the MULTISPEC extraction is lower still (0.56), while Gaussian fits to spatial profiles in our 2D UV NW1 data set (lower left panel in Fig. 2) favour 0.62. We adopt this flux ratio, so $m_{\mathrm{F555W}}^{a1} - m_{\mathrm{F555W}}^{a2} = 0.52$ under the reasonable assumption that their interstellar extinctions are equivalent. From comparison between the UV fluxes of a1 and a2 and relatively isolated sources in the NW1 slit, we support WFC3/F555W photometry of a1, resulting in a revised a2 apparent magnitude of $m_{\mathrm{F555W}} = 12.80$ mag in Table 2. This leads to a downward revision of 0.18 dex in stellar luminosity, and corresponding 20 per cent lower mass estimate.

In addition, WFC3 photometry of a6 from de Marchi et al. (2011) is significantly brighter than Hunter et al. (1995). From our MAMA SE1 data set, we obtain a 1500 Å flux ratio of 0.70 for a6/a3, in perfect agreement with $m_{\mathrm{F555W}}^{a3} - m_{\mathrm{F555W}}^{a6} = -0.38$ from WFC3, so adopt photometry from de Marchi et al. Finally, de Marchi et al. (2011) provide a single photometric measurement for a4+a8, which agrees satisfactorily with the combination of these sources in Hunter et al. (1995). Again, we utilize UV data sets (lower right panel in Fig. 2) to verify their relative fluxes. From our MULTISPEC extraction, we obtain a 1500 Å flux ratio of 0.66 for a8/a4, in good agreement with 0.65 from Gaussian fits to their spatial profiles in the NW3 slit. We obtain $m_{\mathrm{F555W}}^{a4} - m_{\mathrm{F555W}}^{a8} = 0.46$, again assuming identical interstellar extinctions for these stars. From the combined WFC3 photometry of $m_{\mathrm{F555W}}^{a4+a8} = 13.41 \pm 0.01$, we obtain revised a4 and a8 apparent magnitudes of $m_{\mathrm{F555W}} = 13.91$ and 14.42 mag (Table 2).

3 SPATIALLY RESOLVED FAR-UV SPECTROSCOPY

We have classified individual R136 stars, based upon a comparison between their UV morphology and LMC template stars with reliable optical classifications. As noted above, we have incorporated 10 reference O2–O9.5 stars based on optical classifications provided in Caballero-Nieves et al. (in preparation) which are indicated in Tables 2 and 3. Our approach therefore complements the UV classification system of LMC OB stars by Smith Neubig & Bruhweiler (1999) using IUE SWP/LORES spectroscopy. We

Figure 3. Comparison between WFPC2 (Hunter et al. 1995) and WFC3/UVIS photometry (de Marchi et al. 2011) for all sources in common within 10 arcsec of R136a1 (O stars: triangles, WN stars: squares) for F336W (top), F555W (middle) and F814W (bottom). Agreement is generally excellent aside from R136a1, a2 and a6 (see Section 2.3).

Table 2. *HST*/WFC3 photometry (de Marchi et al. 2011) for sources ($m_{F555W} \leq 16.0$ mag). within a projected distance of 2.05 arcsec (0.5 parsec) from R136a1. In case WFC3 photometry is unavailable, WFPC2 photometry from Hunter et al. (1995) is used, albeit offset in F555W by −0.17 mag (indicated in italic font, see Section 2.3). Identifications are from Weigelt & Baier (1985, WB85) or Hunter et al. (1995, HSH95), while spectral types are obtained from optical spectroscopy. A_{F555W} is either obtained via the observed $m_{F336W} - m_{F555W}$ colour plus $R_{5495} = 4.1$, or $A_{F555W} = 1.72$ mag is adopted (values for WN5 stars are from Crowther et al. 2010).

WB85	HSH95	Spectral type	Ref	r (arcsec)	m_{F555W} (mag)	$m_{F336W-F438W}$ (mag)	$m_{F438W-F555W}$ (mag)	$m_{F555W-F814W}$ (mag)	A_{F555W} (mag)	M_{F555W} (mag)	Slit
a1	3	WN5h	b	0.00	12.28 ± 0.01	-1.25 ± 0.01	0.17 ± 0.01	0.49 ± 0.01	1.88	−8.09	NW1
a2	5	WN5h	b	0.08	$12.80 \pm 0.01^{\ddagger}$	-1.23 ± 0.01	0.23 ± 0.01	0.37 ± 0.01	1.83	$-7.52^{\ddagger}$	NW1
a5	20	O2 If*	e	0.28	13.71 ± 0.01	-1.28 ± 0.02	0.06 ± 0.01	0.48 ± 0.01	1.87	−6.65	NW1
a7	24	O3 III(f*)	a	0.36	13.97 ± 0.01	-1.28 ± 0.02	-0.04 ± 0.02	0.30 ± 0.02	1.58	−6.10	NW3
a8	27			0.39	$14.42 \pm 0.01^{\ddagger}$	-1.30 ± 0.01	0.12 ± 0.01	0.27 ± 0.01	1.98	$-6.05^{\ddagger}$	NW3
a4	21			0.43	$13.96 \pm 0.01^{\ddagger}$					$-6.51^{\ddagger}$	
	186			0.43	15.63 ± 0.02	-1.23 ± 0.03	0.10 ± 0.03	0.35 ± 0.04	1.75	−4.62	NW1
	86			0.45	14.73 ± 0.01	-1.42 ± 0.02	0.41 ± 0.02		2.15	−5.91	NW1
a3	6	WN5h	b	0.49	12.97 ± 0.01	-1.31 ± 0.01	0.16 ± 0.01	0.55 ± 0.01	1.87	−7.39	SE1
	66	O3 V	a	0.49	15.06 ± 0.02	-1.29 ± 0.02	0.17 ± 0.02	0.29 ± 0.03	1.95	−5.38	SE2
	119			0.51	*15.75*				1.72	−4.46	NW3
	58	O3 III(f*)	a	0.59	14.80 ± 0.01	-1.30 ± 0.02	0.11 ± 0.02	0.34 ± 0.02	1.96	−5.65	NW1
	30	O7 V	a	0.62	14.21 ± 0.01	-1.31 ± 0.01	0.13 ± 0.01	0.29 ± 0.01	1.61	−5.89	NW4
	70	O5 Vz	f	0.62	14.96 ± 0.01	-1.27 ± 0.02	0.13 ± 0.02	0.37 ± 0.03	1.79	−5.32	NW2
	89			0.66	14.76 ± 0.01	-1.11 ± 0.02	0.34 ± 0.02	0.20 ± 0.02	2.52	−6.25	SE2
	62			0.66	14.91 ± 0.01	-1.36 ± 0.02	0.11 ± 0.02	0.31 ± 0.02	1.85	−5.43	SE3
a6	19			0.73	13.35 ± 0.01	-1.26 ± 0.01	0.07 ± 0.01	0.46 ± 0.01	1.82	−6.96	SE1
	50			0.74	14.65 ± 0.01	-1.25 ± 0.01	0.11 ± 0.01	0.37 ± 0.02	2.05	−5.89	SE3
	90	O5 V::	a	0.77	15.48 ± 0.02	-1.36 ± 0.03	0.12 ± 0.03	0.34 ± 0.04	1.67	−4.68	NW3
	149			0.78	15.44 ± 0.02	-1.28 ± 0.03	0.17 ± 0.03	0.26 ± 0.04	1.96	−5.01	SE2
	141			0.78	15.82 ± 0.03	-1.35 ± 0.03	0.09 ± 0.03	0.29 ± 0.05	1.55	−4.22	SE4
	80	O8 V	f	0.87	15.17 ± 0.02	-1.30 ± 0.02	0.11 ± 0.02	0.25 ± 0.03	1.53	−4.85	SE3
	35	O3 V	f	0.88	14.32 ± 0.01	-1.43 ± 0.01	0.11 ± 0.01		1.64	−5.81	NW5
	78	O4: V	f	0.97	15.26 ± 0.02	-1.33 ± 0.02	0.11 ± 0.02	0.29 ± 0.03	1.70	−4.93	NW3
	73	O9 V	a	1.01	15.13 ± 0.02	-1.12 ± 0.02	0.11 ± 0.02		1.78	−5.14	SE4
	92	O3 V	a	1.05	15.46 ± 0.02	-1.36 ± 0.02	0.10 ± 0.03	0.30 ± 0.04	1.52	−4.55	NW6
	143			1.05	15.94 ± 0.03	-1.30 ± 0.04	0.19 ± 0.04	0.36 ± 0.06	1.70	−4.25	SE2
	112	O8.5 III(f)	a	1.06	15.74 ± 0.03	-1.25 ± 0.04	0.12 ± 0.04	0.29 ± 0.05	1.65	−4.40	NW2/3
	135			1.08	15.90 ± 0.03	-1.20 ± 0.04	0.13 ± 0.04		1.67	−4.26	NW5
	69	O3–6 V	a	1.09	*15.05*	-1.32 ± 0.04			1.72	−5.16	SE5
	52	O3 V	a	1.13	14.72 ± 0.01	-1.34 ± 0.01	0.09 ± 0.01	0.22 ± 0.02	1.71	−5.48	SE5
	48	O2–3 III(f*)	f	1.22	14.75 ± 0.01	-1.26 ± 0.01	0.10 ± 0.01	0.46 ± 0.02	2.01	−5.75	SE2
	77	O5.5 V+O5.5 V	d	1.29	15.21 ± 0.01	-1.31 ± 0.02	0.04 ± 0.02	0.30 ± 0.02	2.87	−6.15	SE6
	94	O3 V	a	1.31	15.57 ± 0.02	-1.31 ± 0.03	0.10 ± 0.03	0.28 ± 0.04	1.69	−4.61	SE6
	115			1.41	15.76 ± 0.02	-1.32 ± 0.03	0.12 ± 0.03	0.28 ± 0.04	1.44	−4.17	NW8
	132			1.48	15.86 ± 0.03	-1.35 ± 0.03	0.13 ± 0.03	0.22 ± 0.04	1.40	−4.03	NW8
	36	O2 If*	f	1.51	14.41 ± 0.01	-1.26 ± 0.01	0.11 ± 0.01	0.48 ± 0.01	1.89	−5.97	SE3
	173			1.53	15.98 ± 0.03	-1.32 ± 0.04	0.19 ± 0.04	0.25 ± 0.05	1.56	−4.07	NW8
	75			1.56	15.08 ± 0.01	-1.32 ± 0.02	0.10 ± 0.01	0.18 ± 0.02	1.70	−5.11	NW8
	114			1.57	15.68 ± 0.02	-1.35 ± 0.03	0.10 ± 0.03	0.21 ± 0.04	1.44	−4.25	SE7
	108			1.59	15.44 ± 0.02	-1.35 ± 0.02	0.18 ± 0.02	0.25 ± 0.03	1.60	−4.65	NW8
	31			1.64	14.12 ± 0.01	-1.31 ± 0.01	0.10 ± 0.01	0.32 ± 0.01	1.92	−6.29	SE8
	49	O3 V	a	1.67	14.75 ± 0.01	-1.41 ± 0.01	0.15 ± 0.01	0.27 ± 0.02	1.60	−5.34	NW8
	207			1.72	15.65 ± 0.02		0.09 ± 0.02	0.47 ± 0.03	*1.72*	−4.56	SE2
	46			1.73	14.56 ± 0.01	-1.25 ± 0.01	0.21 ± 0.01	0.49 ± 0.01	2.14	−6.07	SE2
	47	O3 III(f*)	a	1.75	14.72 ± 0.01	-1.22 ± 0.01	0.15 ± 0.01	0.45 ± 0.01	2.10	−5.87	NW3
	40	O3 V	a	1.80	14.56 ± 0.01	-1.34 ± 0.01	0.08 ± 0.01	0.29 ± 0.01	1.83	−5.76	NW8
	118			1.81	*15.74*				1.72	−4.49	SE2
	116			1.81	15.79 ± 0.02	-1.32 ± 0.03	0.10 ± 0.03		1.51	−4.21	SE6
	42	O3 V+O3 V	d	1.83	14.72 ± 0.01	-1.36 ± 0.01	-0.03 ± 0.01	0.44 ± 0.01	1.45	−5.22	NW8
	55	O3 V	a	1.84	14.74 ± 0.01	-1.31 ± 0.01	0.09 ± 0.01	0.31 ± 0.01	1.91	−5.66	SE9
	39	O3 V+O5.5 V	d	1.95	14.50 ± 0.01	-1.32 ± 0.01	0.08 ± 0.01	0.21 ± 0.01	1.76	−5.75	–
	137			1.97	15.97 ± 0.02	-1.33 ± 0.03	0.07 ± 0.03	0.23 ± 0.04	1.51	−4.03	–
	71	O3–6 V	a	2.03	15.16 ± 0.01	-1.35 ± 0.01	0.11 ± 0.01		1.67	−5.00	SE9
	121	O9.5 V	f	2.05	15.85 ± 0.02	-1.24 ± 0.03	0.12 ± 0.03		1.58	−4.22	SE8

Notes. (a): Massey & Hunter (1998); (b): Crowther & Dessart (1998); (c): Walborn et al. (2002a); (d): Massey, Penny & Vukovich (2002); (e): Crowther & Walborn (2011); (f): Caballero-Nieves et al. (in preparation).
‡: Absolute magnitudes have been adjusted for R136a2, a4 and a8 (see Section 2.3).

Table 3. *HST*/WFC3 photometry (de Marchi et al. 2011) for additional STIS/MAMA sources ($m_{F555W} \le = 16.0$ mag) beyond a projected distance of 2.05 arcsec (0.5 parsec) from R136a1. In case WFC3 photometry is unavailable, WFPC2 photometry from Hunter et al. (1995) is used, albeit offset in F555W by −0.17 mag (indicated in italic font, see Section 2.3). Identifications are from Weigelt & Baier (1985, WB85) or Hunter et al. (1995, HSH95), while spectral types are obtained from optical spectroscopy. A_{F555W} is either obtained via the observed $m_{F336W}-m_{F555W}$ colour plus $R_{5495} = 4.1$, or $A_{F555W} = 1.72$ mag is adopted (values for WN5 stars are from Crowther et al. 2010).

WB85	HSH95	Spectral type	Ref	r (arcsec)	m_{F555W} (mag)	$m_{F336W-F438W}$ (mag)	$m_{F438W-F555W}$ (mag)	$m_{F555W-F814W}$ (mag)	A_{F555W} (mag)	M_{F555W} (mag)	Slit
b	9	O4 If/WN8	b	2.12	13.24 ± 0.01	−1.14 ± 0.01	0.18 ± 0.01	0.57 ± 0.01	2.10	−7.31	SE8
	65			2.20	*15.01*				1.72	−5.20	SE7
	134	O7 Vz	b	2.28	15.97 ± 0.01	−1.36 ± 0.02	0.10 ± 0.02	0.23 ± 0.03	1.57	−3.97	SE6
	64	O7 V((f))	a	2.44	15.03 ± 0.01	−1.19 ± 0.01	0.14 ± 0.01	0.38 ± 0.01	1.96	−5.42	NW7
	45	O3 V	a	2.45	14.65 ± 0.01	−1.32 ± 0.01	0.15 ± 0.01	0.43 ± 0.01	1.77	−5.61	SE7
	123	O6 V	b	2.47	15.91 ± 0.01	−1.32 ± 0.02	0.10 ± 0.02	0.09 ± 0.03	1.58	−4.16	SE3
	68			4.61	15.15 ± 0.01	−1.24 ± 0.01	0.18 ± 0.01	0.46 ± 0.01	1.88	−5.22	SE4
	102			4.83	15.70 ± 0.01	−1.18 ± 0.02	0.26 ± 0.01	0.66 ± 0.01	2.44	−5.24	NW1

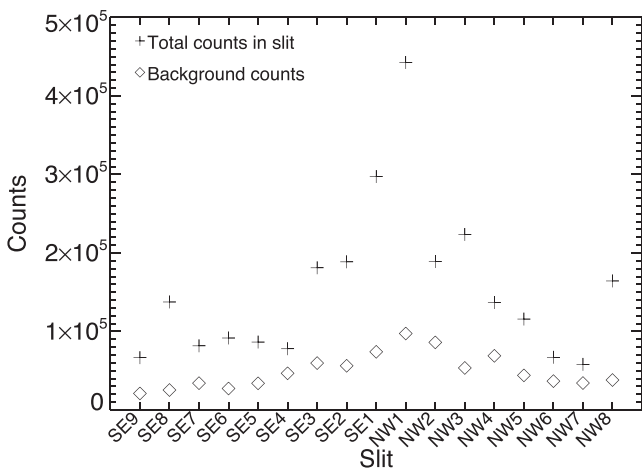*Notes.* (a): Massey & Hunter (1998); (b): Caballero-Nieves et al. (in preparation).

Figure 4. Comparison of the background (diamonds) to total (pluses) far-ultraviolet counts in the central 4 arcsec (∼1 pc) of each slit. This background represents a combination of unresolved cluster members (20 per cent) plus extended emission from bright stars in adjacent slits (15 per cent).

adopt existing (optical) subtypes for the three WN5 stars in R136a (Crowther & Dessart 1998).

In addition to the point sources, a significant fraction of the far-UV spectrum of the central parsec of R136 arises from the intra-cluster background, on the basis of the MULTISPEC fits to the 100 brightest cluster members. This is illustrated in Fig. 4, and represents a combination of unresolved cluster members plus extended emission from bright cluster stars originating in adjacent slits. In Fig. 5, we present the far-UV spectra from the sum of selected background regions of SE3 (1 arcsec E of R136a1) and SE4 (0.7 arcsec SE of R136a1), reminiscent of R136 H70 (O5 Vz), except for extended He II emission originating from either R136a1 or a2. ∼20 per cent of the integrated far-UV continuum arises from the diffuse background, with bright stars in adjacent slits contributing the remaining 15 per cent of the total.

3.1 UV morphology of O stars in the LMC

Walborn, Nichols-Bohlin & Panek (1985) have previously presented an atlas of O stars based on IUE/HIRES spectroscopy. The overwhelming majority of these stars are located in the Milky Way. More recently, Walborn et al. (1995, 2002c, 2004) have presented *HST* and FUSE UV spectroscopy of Magellanic Cloud O stars, although
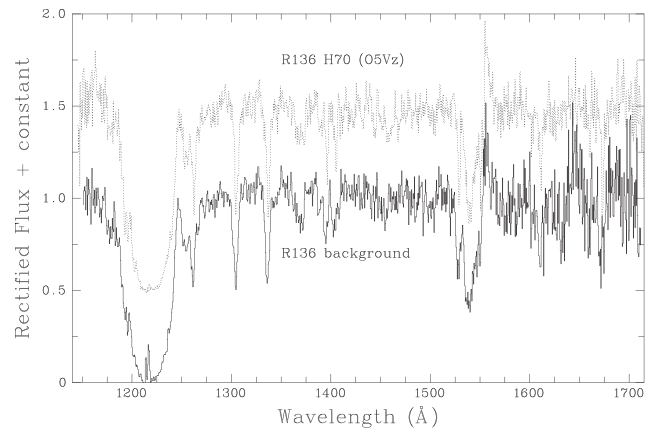

Figure 5. Intra-cluster far-UV spectra of selected inner regions from SE3 and SE4 slits, in close proximity (0.7–1 arcsec, solid) to R136a1 together with R136 H70 (O5 Vz, dotted) for reference. Extended He II λ1640 emission from R136a1 is apparent in the extracted background spectra.

subtypes and luminosity classes are poorly sampled. Since then, a number of *HST* programmes have obtained UV spectroscopy for a range of LMC O stars (e.g. Massey et al. 2004, 2005, 2009). In Appendix A, we present a montage of UV spectroscopic sequences for dwarfs, giants and supergiants (Figs A1–A4), with luminosity sequences shown in Figs A5–A11. A log of observations of these data sets is presented in Table A1.

There is a clear variation in UV morphology amongst O stars from early to late subtypes and from dwarf to supergiant, although we wish to highlight wind line profile variation at an individual subtype/luminosity class. By way of example, we present C IV λλ1548–51 P Cygni line profiles amongst six O4–5.5 dwarfs in the LMC in Fig. 6. Both LH81/W28-5 and R136 H78 possess saturated P Cygni (black) absorption troughs, whereas other stars possess shallow extended absorption troughs which may be flat (e.g. Sk–70° 60, LH 58–496, Sk–70° 69) or deeper at high velocities (R136 H70). Within this sample, P Cygni emission components are relatively weak, with the exception of Sk–70° 69 for which C IV emission is very prominent.

This variation indicates (at least) a third parameter affecting the wind profiles beyond ionization and luminosity class. While further investigation is required, it may well be age, i.e. evolutionary distance from the zero-age main sequence, since some of these stars are in very young regions. While LH 81/W28–5 does have a strong
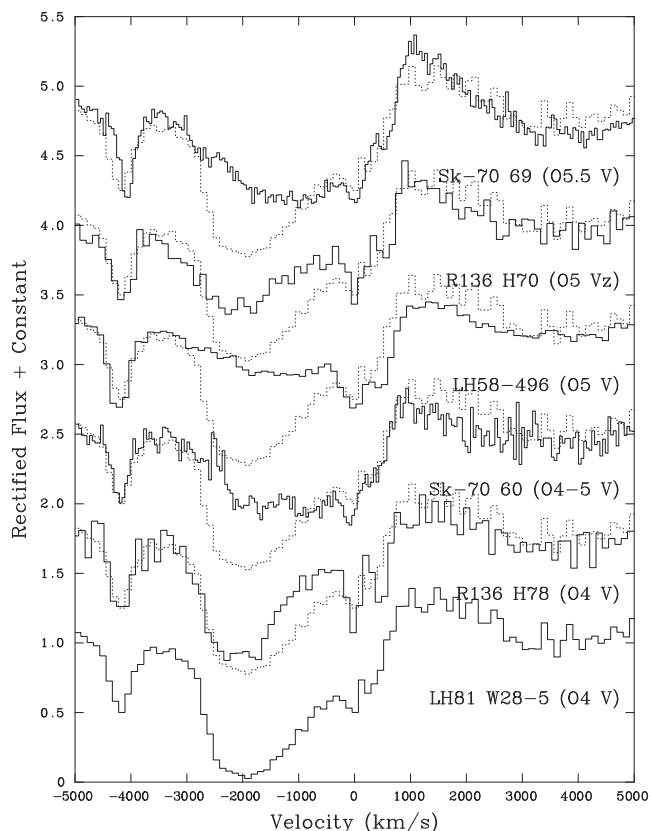
Figure 6. Variation in spectral morphology of C IV 1548–51 amongst O4–5.5 dwarf stars in the LMC. The O4 dwarf LH81/W28-5 (Massey et al. 2004) is shown for reference in each case (dotted lines).

He II λ4686 absorption line (Massey et al. 2004, their fig. 17), it is substantially weaker than He II λ4541, indicating a higher luminosity and/or stronger wind than for typical class V. It is well known that mass-loss rates of O stars at a given temperature and luminosity span a wide range of values (Hillier et al. 2003). Binaries and/or binary evolution may also be relevant contributors to this diversity.

3.2 UV morphology of stars in R136

In Appendix B we present a series of montages of UV spectroscopy of stars in R136 (Figs B1–B9), together with UV templates where appropriate.

In Fig. B1, we present *HST*/STIS spectroscopy of the three luminous WN stars R136a1, a2 and a3 (Crowther et al. 2010). These stars have previously been observed in the UV with *HST*/GHRS (de Koter et al. 1997), although a1 and a2 were blended in the GHRS 0.22 arcsec entrance aperture. Our long-slit STIS spectroscopy was obtained at a position angle of 64° and extracted with MULTISPEC to disentangle a1 from a2. Nevertheless, the UV morphologies of all WN stars are extremely similar to one another, as is the case optically (*HST*/FOS, de Koter et al. 1997) and in the near-IR (VLT/SINFONI, Schnurr et al. 2008). We include an IUE/LORES spectrum of R146 (Brey 88, WN5) for comparison.

In Fig. B2, we present *HST*/STIS spectroscopy of two Of/WN stars, Melnick 37 and Sk–67° 22, together with a5 and b. R136a5 has previously been observed in the UV by *HST*/GHRS and classified as O3f/WN (de Koter et al. 1994). From optical *HST*/FOS spectroscopy, R136a5 has been assigned O3 If/WN (Massey & Hunter 1998) or O2 If* (Crowther & Walborn 2011). The closest

LMC analogue to R136a5 in the UV is Sk–67° 22 (O2 If/WN5). R136b has also previously been observed with *HST*/GHRS (GO 6018/Heap) while Massey & Hunter (1998) assigned O4 If⁺ from *HST*/FOS spectroscopy (see also Crowther & Walborn 2011). From STIS/CCD spectroscopy, the ratio of N IV λ4058/N III λλ4634, 41 is characteristic of O4 and WN8 subtypes (rather than O3.5 and WN7) so O4 If/WN8 is newly inferred here. He II λ1640 and Si IV λλ1394-1402 P Cygni profiles are much stronger in R136b than for conventional LMC O4 supergiants (e.g. Sk–65° 47, Fig. A8).

HST/STIS spectroscopy of O2–3 (super)giants in R136 is presented in Fig. B3, including the LMC O2–3 III and O2 If reference stars R136 H48 and H36, from our new STIS/CCD data set. Massey & Hunter (1998) previously assigned O3 III for H48 while Walborn et al. (2002a) assigned O2–3 If for H36. The O2 supergiant classification of R136a6 is new here, with R136 H46 and H47 assigned O2 III–If, owing to their morphological similarity to the candidate runaway star VFTS 16 (Evans et al. 2010). Another example of a O2–3 III star is observed beyond the central parsec, namely R136 H102 located 4.8 arcsec to the NE.

Fig. B4 presents STIS/MAMA spectroscopy of eight O2–3 V stars in R136 together with the templates BI 237 (O2 V) and R136 H35 (O3 V) based on our new STIS/CCD data sets. All stars exhibit prominent O V λ1371 absorption, P Cygni C IV λλ1548–51, N V λλ1238–42 and negligible/weak absorption at He II λ1640. Of these, six stars have previously been spectroscopically observed with *HST*/FOS by Massey & Hunter (1998), who assigned O3 V or O3 III classifications. R136a4, a8, H31, H50 and H62 are newly classified as O2–3 V in this study.

HST/STIS spectroscopy of seven UV-classified O3–4 dwarfs in R136 is presented in Fig. B5 together with the reference stars R136 H35 (O3 V) and H78 (O4 V) from our STIS/CCD spectroscopy. All O3–4 dwarfs possess weak O V λ1371 absorption, plus prominent, albeit unsaturated C IV λλ1548–51 P Cygni profiles (Fig. A6). Of these, four have previously been spectroscopically observed by Massey & Hunter (1998), who assigned O3 V, except for R136a7 for which O3 III was proposed from *HST*/FOS spectroscopy. R136 H86 and H149 are newly classified here as O3–4 V from STIS/MAMA data sets, although the latter, centrally located in the SE2 slit, suffers from significant He II λ1640 contamination by R136a3 (SE1).

Fig. B6 presents STIS/MAMA spectroscopy for dwarf O4–5 stars in R136 together with new templates R136 H78 (O4 V) and H70 (O5 V) from new STIS/CCD observations. We favour O4 V for R136 H65, H71, H75, H89 and H90 from their morphological similarity to H78, while O4–5 V is preferred for H45, H49, H94 and H119. Classifications are in good agreement with Massey & Hunter (1998) who proposed O3 V for H45, H49 and H94, O5 V for H90 and O3–6 V for H71. Fig. B7 extends this sequence to O5 V and O6 V subtypes, exploiting a STIS/CCD subtype of H123 (O6 V). We propose O5 V subtypes for H64 and H69, O6 V subtypes for H30, H77 and H92, and O5–6 V for H141, again in reasonable agreement with Massey & Hunter (1998) who adopted O7 V for H30 and H64, O3–6 V for H69, O3 V for H92. Massey et al. (2002) obtained O5.5 V+O5.5 V for H77. The UV morphology of R136 H68, located 4.6 arcsec from R136a1, is also consistent with O6 V.

Fig. B8 presents STIS spectroscopy for O7–8 dwarfs in R136, exploiting new optical subtypes of O7 V and O8 V for R136 H134 and H80, respectively. All stars are newly classified except for H112, for which Massey & Hunter (1998) proposed O8.5 III. A very weak wind signature of C IV λλ1548–51 is observed, via either very shallow P Cygni absorption or a clear blueshifted absorption. We assign O9+ V subtypes for the final group of stars, presented in Fig. B9, for which solely photospheric C IV λλ1548–51 absorption is

Table 4. STIS/MAMA-derived properties of R136 stars within a projected distance of 2.05 arcsec (0.5 pc), brighter than $m_{\rm F555W} = 16.0$ mag), sorted by projected distance from R136a1. References to optical (literature) spectral types are provided in Table 2. F_{1500} fluxes are averages for the range 1500 ± 25 Å(estimated values are provided in parentheses). Aside from the WN5 stars (Crowther et al. 2010), temperatures and luminosities are from spectral type calibrations (Doran et al. 2013), while inferred current masses M and ages τ for O stars are from BONNSAI (Schneider et al. 2014a) using the Bonn evolutionary models (Brott et al. 2011; Köhler et al. 2015). Velocities include $v_{\rm edge}$, $v_{\rm black}$ and v_∞ (colons indicate less secure values).

HSH95 (WB85)	Optical Sp type	Ultraviolet Sp type	r (arcsec)	$10^{14} F_{1500}$ (erg s^{-1} cm^{-2} Å)	$M_{\rm F555W}$ (mag)	$T_{\rm eff}$ (kK)	$\log L/L_\odot$	$M_{\rm current}$ (M$_\odot$)	τ (Myr)	$v_{\rm edge}$ (km s^{-1})	$v_{\rm black}$ (km s^{-1})	v_∞ (km s^{-1})	Fig.
3 (a1)	WN5h	WN5	0.00	22.9 ± 1.4	-8.09	53 ± 3	6.94 ± 0.09	315^{+60}_{-50}	$0.0^{+0.3}_{-0.0}$	3270:	2600	2600	B1
5 (a2)	WN5h	WN5	0.08	13.1 ± 1.2	-7.52	53 ± 3	6.63 ± 0.09	195^{+35}_{-30}	$0.3^{+0.4}_{-0.3}$	3440	2425	2425	B1
20 (a5)	O2 If*	O2 If/WN5	0.28	6.9 ± 0.3	-6.65	50^{+4}_{-5}	$6.32^{+0.16}_{-0.15}$	101^{+28}_{-26}	$0.8^{+0.4}_{-0.7}$	3615	3045	3045	B2
24 (a7)	O3 III(f*)	O3–4 V	0.36	4.4 ± 0.4	-6.10	46^{+4}_{-3}	$5.99^{+0.10}_{-0.09}$	69^{+12}_{-10}	$0.5^{+0.1}_{-0.3}$	3385	–	2710:	B5
27 (a8)		O2–3 V	0.39	5.2 ± 0.3	-6.05	51 ± 6	$6.28^{+0.13}_{-0.15}$	96^{+27}_{-22}	$0.8^{+0.5}_{-0.8}$	3550	2980	2980	B4
21 (a4)		O2–3 V	0.43	7.8 ± 0.3	-6.51	51 ± 6	$6.46^{+0.13}_{-0.15}$	124^{+37}_{-31}	$0.3^{+0.2}_{-0.3}$	3275	2475:	2475:	B4
186		–	0.43	(1.3)	-4.62	–	–	–	–	–	–	–	–
86		O3–4 V	0.45	2.1 ± 0.2	-5.91	46^{+4}_{-3}	$5.91^{+0.10}_{-0.08}$	63^{+10}_{-8}	$1.5^{+0.5}_{-0.9}$	3275:	2475	2475	B5
6 (a3)	WN5h	WN5	0.49	16.3 ± 2.1	-7.39	53 ± 3	6.58 ± 0.09	180^{+30}_{-30}	$0.3^{+0.4}_{-0.3}$	2950	2400	2400	B1
66	O3 V	O3–4 V	0.49	2.2 ± 0.2	-5.38	46^{+4}_{-3}	$5.70^{+0.10}_{-0.08}$	51 ± 7	$1.4^{+0.6}_{-1.1}$	3045	2590	2590	B5
119		O4–5 V	0.51	2.7 ± 0.2	-4.46	43 ± 3	$5.24^{+0.08}_{-0.09}$	32^{+4}_{-3}	$0.8^{+1.4}_{-0.8}$	3075	–	2460:	B6
58	O3 III(f*)	O2–3 V	0.59	2.7 ± 0.3	-5.65	51 ± 6	$5.93^{+0.13}_{-0.15}$	63^{+16}_{-12}	$0.6^{+0.9}_{-0.6}$	–	2980	2980	B4
30	O7 V	O6 V	0.62	5.7 ± 0.3	-5.89	38 ± 2	$5.67^{+0.05}_{-0.06}$	42 ± 3	$2.9^{+0.3}_{-0.3}$	3110:	–	2490:	B7
70	O5 Vz	O5 V	0.62	2.6 ± 0.2	-5.32	42 ± 2	$5.57^{+0.07}_{-0.08}$	41^{+5}_{-4}	$2.3^{+0.5}_{-0.7}$	3340:	–	2670:	B6
89		O4 V	0.66	1.3 ± 0.1	-6.25	44 ± 2.5	$5.99^{+0.08}_{-0.07}$	65^{+10}_{-9}	1.7 ± 0.4	2425:	–	1940:	B6
62		O2–3 V	0.66	3.3 ± 0.2	-5.43	51 ± 6	$5.84^{+0.13}_{-0.15}$	58^{+13}_{-12}	$0.4^{+1.2}_{-0.4}$	3340	2770	2770	B4
19 (a6)		O2 If	0.73	11.6 ± 0.4	-6.96	46^{+4}_{-2}	$6.52^{+0.10}_{-0.05}$	150^{+36}_{-40}	$0.9^{+0.5}_{-0.6}$	3440	2650	2650	B3
50		O2–3 V	0.74	3.4 ± 0.2	-5.89	51 ± 6	$6.02^{+0.15}_{-0.13}$	70^{+17}_{-14}	$0.8^{+0.7}_{-0.8}$	3390	2620	2620	B4
90	O5 V	O4 V	0.77	1.7 ± 0.1	-4.68	44 ± 2.5	$5.36^{+0.08}_{-0.07}$	36 ± 4	$1.0^{+0.8}_{-1.0}$	–	2475:	2475:	B6
149		O3–4 V::	0.78	1.0 ± 0.1	-5.01	–	–	–	–	2900	2210	2210	B5
141		O5–6 V	0.78	1.0 ± 0.1	-4.22	41 ± 3	5.09 ± 0.12	27^{+4}_{-3}	$1.0^{+1.5}_{-1.0}$	–	–	–	B7
80	O8 V	O8 V	0.87	2.3 ± 0.1	-4.85	36 ± 2	$5.20^{+0.08}_{-0.10}$	26^{+3}_{-2}	$4.0^{+0.8}_{-0.9}$	2070:	–	1655:	B8
35	O3 V	O3 V	0.88	5.5 ± 0.2	-5.81	48 ± 3	$5.92^{+0.08}_{-0.09}$	66^{+10}_{-9}	$1.2^{+0.5}_{-0.8}$	3440	2770	2770	B4
78	O4: V	O4: V	0.97	1.8 ± 0.2	-4.93	44 ± 2.5	$5.47^{+0.08}_{-0.07}$	40^{+5}_{-4}	$1.5^{+0.7}_{-1.1}$	3000	2375:	2375:	B6
73	O9 V	O9+ V	1.01	2.0 ± 0.1	-5.14	33 ± 2	$5.21^{+0.09}_{-0.10}$	24 ± 2	4.8 ± 0.7	–	–	–	B9
92	O3 V	O6 V	1.05	2.2 ± 0.2	-4.55	40 ± 2	$5.20^{+0.07}_{-0.10}$	30 ± 3	$2.3^{+0.9}_{-1.4}$	–	2080:	2080:	B7
143		O7–8 V	1.05	0.8 ± 0.1	-4.25	39 ± 3	$4.99^{+0.12}_{-0.14}$	24 ± 3	$1.6^{+1.4}_{-1.6}$	1850:	–	1480:	B8
112	O8.5 III(f)	O7+ V	1.06	1.0 ± 0.1	-4.40	36 ± 4	$5.01^{+0.10}_{-0.11}$	23 ± 3	$3.8^{+1.6}_{-2.5}$	–	–	–	B8
135		O9+ V	1.08	1.0 ± 0.1	-4.26	33 ± 2	$4.86^{+0.09}_{-0.10}$	20 ± 2	$5.3^{+1.3}_{-1.7}$	–	–	–	B9
69	O3–6 V	O5 V	1.09	2.2 ± 0.2	-5.16	42 ± 2	$5.49^{+0.07}_{-0.08}$	38 ± 4	$2.2^{+0.6}_{-0.9}$	3225	–	2580	B7
52	O3 V	O3–4 V	1.13	4.0 ± 0.3	-5.48	46^{+4}_{-3}	$5.74^{+0.10}_{-0.08}$	53^{+8}_{-7}	0.3 ± 0.2	3260	2820	2820	B5
48	O2–3 III(f*)	O2–3 III	1.22	2.7 ± 0.2	-5.75	51 ± 6	$5.97^{+0.13}_{-0.15}$	66^{+16}_{-12}	$0.7^{+0.8}_{-0.7}$	3615	3045	3045	B3
77	O5.5 V+O5.5 V	O6 V	1.29	2.4 ± 0.2	-6.15	–	–	–	–	1920:	1510:	1510:	B7
94	O3 V	O4–5 V	1.31	1.5 ± 0.1	-4.61	43 ± 3	$5.31^{+0.08}_{-0.09}$	34 ± 4	$1.3^{+0.9}_{-1.2}$	3110:	–	2490:	B6
115		O9+ V	1.41	1.4 ± 0.1	-4.17	33 ± 2	$4.82^{+0.09}_{-0.10}$	19^{+2}_{-1}	$5.3^{+1.4}_{-1.9}$	–	–	–	B9
132		O9+ V	1.48	1.1 ± 0.1	-4.03	33 ± 2	$4.76^{+0.09}_{-0.10}$	18^{+2}_{-1}	$6.2^{+1.6}_{-0.5}$	–	–	–	B9
36	O2 If*	O2 If*	1.51	3.6 ± 0.2	-5.97	46^{+4}_{-2}	$5.94^{+0.10}_{-0.05}$	66^{+10}_{-9}	$1.5^{+0.4}_{-0.9}$	4625:	3500	3500	B3
173		O9+ V	1.53	0.7 ± 0.1	-4.07	33 ± 2	$4.78^{+0.09}_{-0.10}$	19 ± 1	$6.6^{+1.4}_{-0.8}$	–	–	–	B9
75		O4 V	1.56	2.2 ± 0.2	-5.11	44 ± 2.5	$5.54^{+0.08}_{-0.07}$	42 ± 5	$1.7^{+0.7}_{-1.1}$	3000	2550	2550	B6
114		O7–8 V	1.57	1.6 ± 0.1	-4.25	37 ± 3	$4.99^{+0.12}_{-0.14}$	23 ± 3	$3.1^{+1.4}_{-2.2}$	2215:	–	1770:	B8
108		O7–8 V	1.59	1.5 ± 0.1	-4.65	37 ± 3	$5.15^{+0.12}_{-0.14}$	25^{+4}_{-3}	$3.6^{+1.2}_{-1.9}$	1300:	–	1040:	B8
31		O2–3 V	1.64	6.0 ± 0.3	-6.29	51 ± 6	$6.19^{+0.13}_{-0.15}$	87^{+21}_{-20}	$0.8^{+0.5}_{-0.8}$	3500	2815	2815	B4
49	O3 V	O4–5 V	1.67	0.9 ± 0.1	-5.34	43 ± 3	$5.60^{+0.08}_{-0.09}$	43^{+6}_{-5}	$2.0^{+0.7}_{-1.0}$	3780	2980	2980:	B6
207		–	1.72	0.3 ± 0.1	-4.56	–	–	–	–	4560:	–	3650:	–
46		O2 III-If	1.73	2.3 ± 0.2	-6.07	48 ± 4	$6.02^{+0.12}_{-0.09}$	74^{+14}_{-11}	$1.2^{+0.4}_{-0.4}$	4450:	3440	3440	B3
47	O3 III(f*)	O2 III-If	1.75	2.6 ± 0.3	-5.87	48 ± 4	$5.95^{+0.14}_{-0.13}$	65^{+14}_{-11}	$1.1^{+0.5}_{-0.9}$	3615	3045	3045	B3
40	O3 V	O2–3 V	1.80	4.5 ± 0.2	-5.76	51 ± 6	$5.97^{+0.13}_{-0.15}$	66^{+16}_{-12}	$0.7^{+0.8}_{-0.7}$	3435	2750	2750	B4

Table 4 – *continued*

HSH95 (WB85)	Optical Sp type	Ultraviolet Sp type	r (arcsec)	$10^{14}F_{1500}$ (erg s^{-1} cm^{-2} Å^{-1})	M_{F555W} (mag)	T_{eff} (kK)	$\log L/L_\odot$	$M_{current}$ ($M_\odot$)	τ (Myr)	v_{edge} (km s^{-1})	v_{black} (km s^{-1})	v_∞ (km s^{-1})	Fig.
118		O7–8 V	1.81	1.1 ± 0.2	−4.49	39 ± 3	$5.07^{+0.12}_{-0.14}$	25^{+4}_{-3}	$2.2^{+1.2}_{-1.8}$	1460:	–	1170:	B8
116		O7–8 V	1.81	1.3 ± 0.1	−4.21	37 ± 3	$4.97^{+0.12}_{-0.14}$	23 ± 3	$3.0^{+1.4}_{-2.2}$	1200:	–	960:	B8
42	O3 V+O3 V	O3–4 V	1.83	3.5 ± 0.2	−5.22	46^{+4}_{-3}	$5.64^{+0.10}_{-0.08}$	48^{+7}_{-6}	$0.3^{+0.2}_{-0.3}$	3045	2245	2245	B5
55	O3 V	O2–3 V	1.84	3.6 ± 0.2	−5.66	51 ± 6	$5.93^{+0.13}_{-0.15}$	63^{+15}_{-12}	$0.6^{+0.9}_{-0.6}$	3390	2880	2880	B4
39	O3V+O5.5V	–	1.95	(3.7)	−5.75	–	–	–	–	–	–	–	–
137		–	1.97	(1.0)	−4.03	–	–	–	–	–	–	–	–
71	O3–6 V	O4 V	2.03	2.4 ± 0.2	−5.00	44 ± 2.5	$5.49^{+0.08}_{-0.07}$	40^{+5}_{-4}	$1.6^{+0.7}_{-1.1}$	3030	2475	2475	B6
121	O9.5 V	O9.5 V	2.05	1.2 ± 0.1	−4.22	33 ± 1.5	$4.84^{\pm}0.07$	19^{+2}_{-1}	$5.3^{+1.1}_{-1.3}$	–	–	–	B9

Table 5. STIS/MAMA-derived properties of R136 stars beyond a projected distance of 2.05 arcsec (0.5 pc) from R136a1, brighter than $m_{F555W} = 16.0$ mag). References to optical (literature) spectral types are provided in Table 3. F_{1500} fluxes are averages for the range 1500 ± 25 Å. Aside from the WN5 stars (Crowther et al. 2010), temperatures and luminosities are from spectral type calibrations (Doran et al. 2013), while inferred current masses M and ages τ for O stars are from BONNSAI (Schneider et al. 2014a) using the Bonn evolutionary models (Brott et al. 2011; Köhler et al. 2015). Velocities include v_{edge}, v_{black} and v_∞ (colons indicate less secure values).

HSH95 (WB85)	Optical Sp type	Ultraviolet Sp type	r(arcsec)	$10^{14}F_{1500}$ (erg s^{-1} cm^{-2} Å^{-1})	M_{F555W} (mag)	T_{eff} (kK)	$\log L/L_\odot$ ($L_\odot$)	M ($M_\odot$)	τ (Myr	v_{edge} (km s^{-1})	v_{black} (km s^{-1})	v_∞ (km s^{-1})	Fig.
9 (b)	O4 If/WN8	O4 If/WN8	2.12	7.5 ± 0.6	−7.31	41 ± 3	$6.30^{+0.11}_{-0.12}$	93 ± 19	1.5 ± 0.3	2080	1400	1400	B2
65		O4 V	2.20	1.9 ± 0.2	−5.20	44 ± 2.5	$5.56^{+0.08}_{-0.07}$	43 ± 5	$1.7^{+0.6}_{-1.0}$	3110	2540	2540	B6
134	O7 Vz	O7 V	2.28	1.2 ± 0.1	−3.97	38 ± 2	$4.91^{+0.05}_{-0.06}$	23 ± 2	$1.8^{+1.3}_{-1.6}$	1465	–	1170:	B8
64	O7 V((f))	O5 V	2.44	1.7 ± 0.1	−5.42	42 ± 2	$5.60^{+0.07}_{-0.08}$	42^{+5}_{-4}	$2.3^{+0.5}_{-0.6}$	2215:	–	1770:	B7
45	O3 V	O4–5 V	2.45	3.0 ± 0.2	−5.61	43 ± 3	$5.76^{+0.08}_{-0.09}$	50^{+7}_{-6}	$2.0^{+0.6}_{-0.7}$	3275:	–	2620:	B6
123	O6 V	O6 V	2.47	1.1 ± 0.1	−4.16	40 ± 2	$5.04^{+0.07}_{-0.08}$	27 ± 2	$1.2^{+1.1}_{-1.2}$	2020	–	1615:	B7
68		O6 V	4.61	1.6 ± 0.1	−5.22	–	–	–	–	2390	–	1910:	B7
102		O2–3 III	4.83	0.6 ± 0.1	−5.24	–	–	–	–	2865:	2540	2540	B3

observed, in common with H121 for which O9.5 V is obtained from our STIS/CCD spectroscopy. Low S/N becomes increasingly problematic for these stars, whose far-UV fluxes are typically $F_{1500} \sim 10^{-14}$ erg s^{-1} cm^{-2} Å^{-1} or lower.

Of the remaining stars within 2.05 arcsec of R136a1 that are listed in Table 4 two lie beyond our *HST*/STIS slit spectroscopy, namely R136 H39 and H137, of which H39 has been observed previously by Massey et al. (2002) and classified O3 V+O5.5 V. Properties of 8 bright sources beyond the central region of R136a are included in Table 5. Finally, H186 lies close to a much brighter source (H86), within its slit, so we are unable to isolate its UV spectrum.

3.3 Wind velocities for R136 stars

The presence of strong, saturated P Cygni profiles amongst the O stars of R136a allows us to measure their wind velocities. To date, wind velocities for large numbers of Galactic OB stars have been obtained from IUE SWP/HIRES spectroscopy (Prinja et al. 1990; Howarth et al. 1997), whereas wind velocities for O stars in the Magellanic Clouds have been relatively scarce (e.g. Prinja & Crowther 1998; Massey et al. 2004, 2005).

Here we measure the maximum blueward extend of saturated P Cygni absorption lines (usually C IV $\lambda\lambda$1548–51), v_{black}, and use it as a probe of terminal wind velocity, i.e. $v_\infty = v_{black}$ (Prinja et al. 1990). The velocity at which the violet absorption meets the continuum, the edge velocity v_{edge}, is usually larger than v_{black} as a result of turbulent motions in the outflow. Such stochastic motions cause some of the material to move at speeds beyond the local flow

speed, hence, will cause absorption beyond the terminal speed if the line is fully saturated. If P Cygni profiles are not fully saturated, v_∞ can be approximated as a function of v_{edge}. In such cases, the terminal velocity could be underestimated because the ion may no longer be present in the outer wind.

We measure v_{black} and/or v_{edge} with respect to (LMC) interstellar absorption lines C IV $\lambda\lambda$1548–51 and/or Si II λ1527 (e.g. Howarth & Phillips 1986). The systemic radial velocity of R136 is ~268 km s^{-1} (Hénault-Brunet et al. 2012). Individual measurements should be reliable to ±100 km s^{-1}, so v_∞ should be accurate to ±200 km s^{-1}.

For this sample, C IV $\lambda\lambda$1548–51 exhibits one of three spectral morphologies. A significant subset, typically O2–4 stars and supergiants, exhibit saturated P Cygni profiles, from which v_{black} (and v_{edge}) can be measured, as shown for R136 H36 in the top panel of Fig. 7. A further subset possess strong P Cygni profiles, albeit without saturated absorption features, from which v_{edge} can be measured, typical of O5–6 dwarfs, as shown for R136 H70 in the central panel of Fig. 7. O7–8 dwarfs tend not to exhibit prominent P Cygni profiles, but some show blue absorption that are sufficiently distinct from interstellar C IV, as shown in the lower panel of Fig. 7 for H80.

Individual results are presented in Tables 4 and 5. The highest terminal wind velocities are $v_\infty \sim 3500$ km s^{-1} for the O2 (super)giants H36 and H46, while late O dwarfs often possess $v_{edge} \leq 1500$ km s^{-1}, or no wind measurements are possible. Fig. 8 shows edge and black velocities for 28 R136 stars, from which we obtain $v_{black}/v_{edge} = 0.8 \pm 0.05$, which is adopted to estimate wind velocities for stars in which solely edge velocities are measured. For reference, Prinja & Crowther (1998) obtained $v_{black}/v_{edge} \sim 0.7$ for

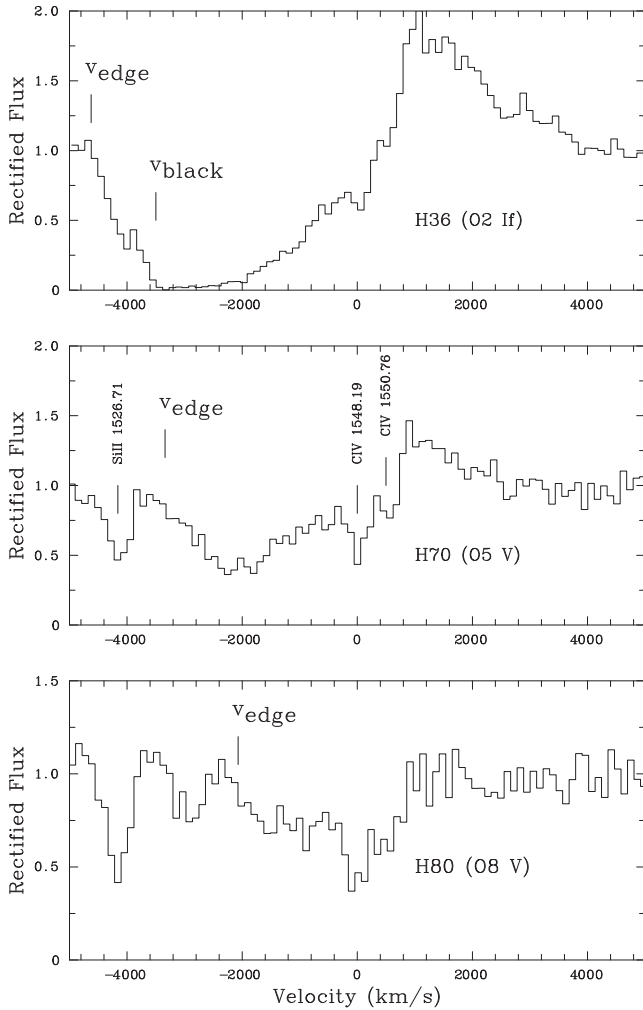**Figure 7.** Representative *HST*/STIS C IV λλ1548–51 profiles for stars with saturated P Cygni profiles (top), unsaturated P Cygni profiles (centre) and non-P Cygni profiles (bottom). Profiles are shown in velocity space in the LMC rest frame of interstellar C IV 1548.2 Å in all cases.

LMC stars and $v_{black}/v_{edge} \sim 0.9$ for 6 R136 stars (in common with this sample).

In Table 6, average values of wind velocities in R136 are provided for O2–3, O3–4, O4–5, O5–6, O7–8 dwarfs, plus early O giants and supergiants, including cases for which wind velocities are based upon $v_\infty = (0.8 \pm 0.05)v_{edge}$. Amongst dwarfs, the trend towards lower wind velocities for later subtypes is apparent. The standard deviation at O5–6 is unusually large since individual estimates span a wide range from 1510 km s^{-1} (H77, O6 V from UV morphology) to 2580 km s^{-1} (H69, O5 V from UV morphology). Statistics of wind velocities for 'field' O stars elsewhere in the LMC are included, drawn from Walborn et al. (1995), de Koter et al. (1998), Prinja & Crowther (1998), Massa et al. (2003), Massey et al. (2004, 2005, 2009), Evans et al. (2010) and Bestenlehner et al. (2014), with individual measurements from the literature and comparisons with present results provided in Table C1 in Appendix C.

The wind velocity of 1400 km s^{-1} for R136b (O4 If/WN8) is extremely low, even with respect to O2–3.5 If/WN stars in the LMC (Table C1). In contrast, O2–3 supergiants within R136 possess higher wind velocities than dwarfs, which is the reverse of O2–3 stars elsewhere in the LMC, albeit based on low-number statistics. For completeness, we obtain an average wind terminal velocity of
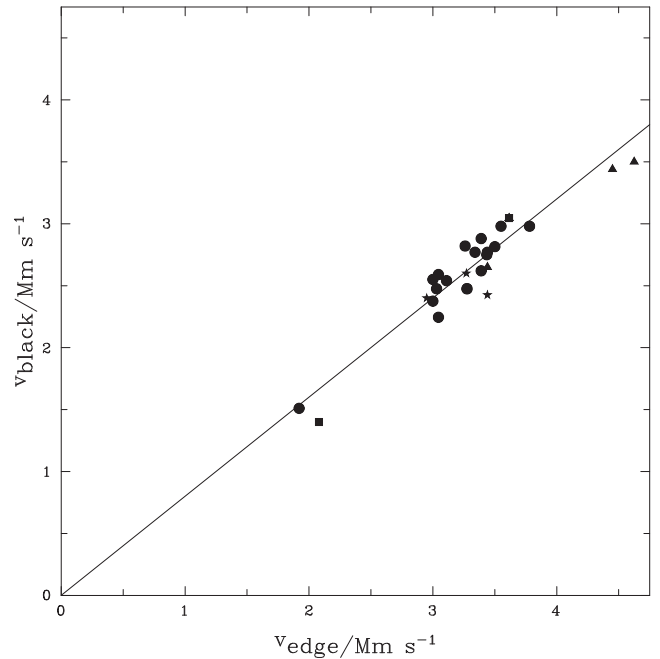

Figure 8. Comparison between edge and black velocities (in Mm s^{-1}) for R136 WN (stars), Of/WN (squares), (super)giants (triangles) and dwarfs (circles), together with the best-fitting $v_{black} = (0.8 \pm 0.05)v_{edge}$ relationship for those stars without saturated black absorption troughs (solid line).

Table 6. Terminal wind velocities (km s^{-1}) and standard deviations (σ) for O stars in R136 (this study) and other O stars in the LMC (Walborn et al. (1995); Massa et al. (2003); Massey et al. (2004, 2005, 2009), Evans et al. (2010); Bestenlehner et al. (2014). N is the sample size for each category.

Subtype	Dwarf			Giants			Supergiants		
	v_∞	σ	N	v_∞	σ	N	v_∞	σ	N
	– R136 (*HST*/STIS) –								
O2–3	2780	160	9	3020	370	4	3065	425	3
O3–4	2525	235	8	–	–	–	1400	–	1
O4–5	2475	245	11	–	–	–	–	–	–
O5–6	2095	415	8	–	–	–	–	–	–
O7–8	1320	315	7	–	–	–	–	–	–
	– LMC field (HST FOS/STIS/COS; FUSE) –								
O2	3290	155	2	3310	180	7	2600	345	4
O3–3.5	2950	375	4	2880	450	2	2000	–	1
O4–5	2510	205	5	2360	245	3	1900	130	5
O6.5–8	1950	–	1	2675	1025	4	1950	70	2
O8.5–9.7	–	–	–	–	–	–	1375	375	6

2475 ± 110 km s^{-1} for the three WN5 stars within R136a. Crowther et al. (2010) obtained $v_\infty = 2200$–2600 km s^{-1} for these stars from their UV to near-IR spectroscopic analysis.

Our new data set effectively double the sample of LMC early O stars with measured wind velocities. It is important to note that a range of wind velocities have been obtained for individual stars. In part this arises from the methodology, either direct measurement as applied here or line fitting based on the Sobolev with Exact Integration method (SEI; Groenewegen & Lamers 1989). Still, different authors applying the same approach to the same data set have obtained significantly different wind velocities. By way of example, de Koter et al. (1998) obtained $v_\infty = 3000$ km s^{-1} from *HST* GHRS spectroscopy of R136a5, while Massey et al. (2004) obtained 3400 km s^{-1} from the same data set; we find 3045 ± 200 km s^{-1}
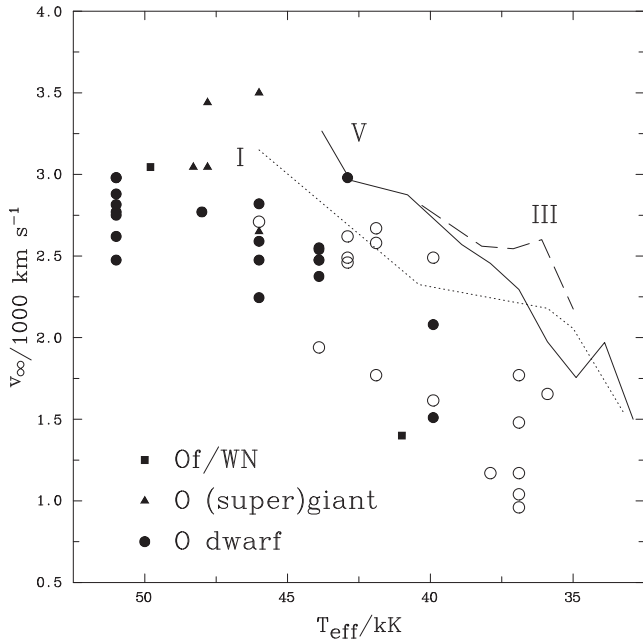
Figure 9. Wind velocities (in km s^{-1}) versus estimated stellar temperature [Of/WN stars: squares, (super)giants: triangles, dwarfs: circles] based on v_{black} (filled) or v_{edge} (open) assuming the temperature scale of Doran et al. (2013). Average velocities versus stellar temperature for Galactic O stars from Prinja et al. (1990) are indicated as dotted lines (supergiants), dashed lined (giants) and solid lines (dwarfs), incorporating the updated classification scheme of Walborn et al. (2002a) and temperature scale of Martins et al. (2005) plus T_{eff} (O2 I) = 46 kK.

from STIS spectroscopy. Mindful of concerns about systematic differences between alternative approaches, an SEI analysis of H36 was carried out (Prinja, private communication) revealing $v_\infty = 3500$ km s^{-1}, $v_{turb}/v_\infty = 0.15$ for a $\beta = 1$ velocity law, in agreement with the v_{black} result. This does not imply that all such measurements will be entirely consistent, although it does suggest that there is no inherent systematic offset.

Despite the low-number statistics, wind velocities of O2–4 dwarfs in R136 are somewhat lower than elsewhere in the LMC. By way of example, the average wind velocity of 8 R136 O3–4 dwarfs is 2525 km s^{-1}, versus 2900 km s^{-1} for five counterparts elsewhere in the LMC (and 3040 km s^{-1} for Galactic O3–4 dwarfs). The reason for this is not clear, if not simply due to small sample sizes. If physical, it is likely not the result of a lower metallicity in 30 Doradus ($v_\infty \propto Z^{0.13}$; Leitherer, Robert & Drissen 1992) relative to the rest of the LMC, although youth may be a factor, recalling the discussion linked to Fig. 6.

Wind velocities for individual R136 stars are presented as a function of stellar temperature in Fig. 9, based on UV-derived subtypes and the temperature calibration of LMC O stars of Doran et al. (2013), in which results from v_{black} (filled symbols) and v_{edge} (open symbols) are distinguished. We have included average UV-derived wind velocities for Galactic O stars from Prinja et al. (1990) – based on the same methodology as used here – updated for O2–4 stars following Walborn et al. (2002a), and adopting the Martins, Schaerer & Hillier (2005) Galactic observational temperature calibration adapted for LMC O stars by Doran et al. (2013).

To date, comparisons of empirical (reduced) wind momenta of O stars with theoretical predictions either adopt wind velocities or are based on calibrations. Pre-empting our stellar mass estimates from Section 3.4, we are able to compare terminal wind velocities
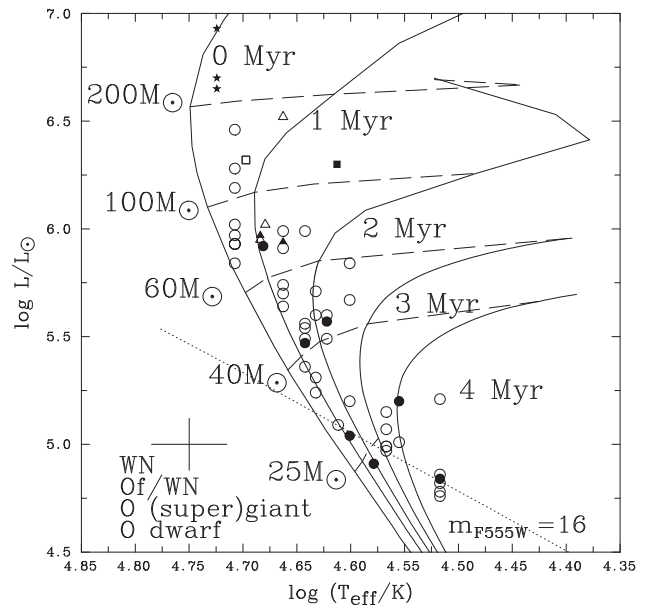

Figure 10. Hertzsprung–Russell diagram [WN: stars; Of/WN stars: squares; (super)giants: triangles; dwarfs: circles] brighter than $m_{F555W} = 16.0$ mag within 0.6 pc from R136a1, based on either optically-derived (filled) or UV-derived (open) spectral types using the temperature calibrations from Doran et al. (2013). LMC isochrones for slowly rotating stars ($v_{eq} = 100$ km s^{-1}) at ages of 0, 1, 2, 3 and 4 Myr are overlaid (solid), together with individual tracks for 25, 40, 60, 100 and 200 M$_\odot$ stars (dashed), from Brott et al. (2011) and Köhler et al. (2015). Representative uncertainties are indicated in the lower left. A dotted line marking $m_{F555W} = 16.0$ mag for an adopted $A_{F555W} = 1.72$ mag is indicated, emphasizing that our census is sensitive to all luminous stars in R136a.

with escape velocities. Lamers et al. (1995) obtained $v_\infty/v_{esc} = 2.65 \pm 0.2$ for 16 Galactic O stars earlier than O7. From 35 O2–6 stars in R136, we find $v_\infty/v_{esc} = 2.5 \pm 0.4$, in agreement with the Galactic sample. Therefore, although R136 early O stars possess ∼15 per cent lower wind velocities than Galactic counterparts, the ratio v_∞/v_{esc} is unchanged. Still, considerable variation *is* observed for other O stars in metal-poor galaxies (Garcia et al. 2014).

3.4 Physical parameters for R136 stars

De Koter et al. (1998) provided UV-derived parameters of the brightest dozen or so members in R136, while Massey & Hunter (1998) provided a more complete Hertzsprung–Russell diagram from *HST*/FOS spectroscopy. Since then, Doran et al. (2013) have provided updated physical parameters for stars within R136 using contemporary calibrations for O stars in the LMC, based on the Galactic scale from Martins et al. (2005).

We defer more robust R136 O-type classifications until future papers in this series, but already our UV morphological classification allows us to present a preliminary, near complete Hertzsprung–Russell diagram for luminous stars within a radius of 2.5 arcsec (0.6 parsec) of R136a1. Temperatures and bolometric corrections of O stars are adopted from tables 5–7 of Doran et al. (2013), while properties of Of/WN stars are adopted from their Appendix A. *HST*/WFC3 photometry (de Marchi et al. 2011), except in particularly crowded regions (recall a1/a2, a4/a8), and interstellar extinctions provide absolute magnitudes as set out in Section 2.3.

In Fig. 10, we present the first spectroscopically derived Hertzsprung–Russell diagram for stars brighter than

$m_{\rm F555W} = 16.0$ mag within 0.6 pc from R136a1. A dotted line corresponding to $m_{\rm F555W} = 16.0$ mag for an adopted $A_{\rm F555W} = 1.72$ mag is indicated, highlighting the region where our sample is complete. A total of 25 stars (26 including R136c), mostly early O dwarfs, are more massive than ~ 50 $M_\odot$. The remaining stars are mid- to late O dwarfs with initial masses above ~ 20 $M_\odot$.

3.5 Ages and masses of individual stars in R136

LMC isochrones for rotating stars with $v_{\rm eq} = 100$ km s^{-1} from Brott et al. (2011) and Köhler et al. (2015) are included, together with tracks for non-rotating 25, 40, 60, 100 and 200 $M_\odot$. These tracks were selected as representative since they closely match the average rotation rate of O stars in 30 Doradus (Ramírez-Agudelo et al. 2013), though do not differ significantly from non-rotating models. It is apparent that, R136b aside, all stars with initial masses above 100 $M_\odot$ lie between the 0–1 Myr isochrones, whereas stars with masses between 40 and 100 $M_\odot$ span 0–2.5 Myr, and those below 40 $M_\odot$ typically span 0–4 Myr, although uncertainties in physical parameters do not exclude ages below ~ 2 Myr, with the exception of R136 H73 (O9+ V) for which an age of ~ 5 Myr is favoured.

For quantitative mass and age determinations, we have exploited BONNSAI[2] (Schneider et al. 2014a) which implements a Bayesian method of quantifying ages and masses from comparison between UV-estimated temperatures and luminosities and evolutionary models, involving two key priors: a Salpeter mass function and an adopted rotation distribution of O stars from VLT Flames Tarantula Survey (VFTS, see Ramírez-Agudelo et al. 2013). Individual age and mass estimates are presented in Tables 4 and 5, and include results for the WN5h stars solely based upon their positions in the HR diagram, i.e. for consistency initially neglecting their He-abundances.

As suggested by Fig. 10, application of the Bonn evolutionary models (via BONNSAI) to the three WN5h stars implies very young ages of ≤ 0.3 Myr in all cases. Low initial rotation rates – favoured by observations of O stars in 30 Dor (Ramírez-Agudelo et al. 2013) – will lead to a redward evolution on the main sequence in evolutionary models, so young ages are required to explain the blue location of the WN5h stars. The next most luminous stars are extreme O supergiants, R136a5 (O2 If/WN5), a6 (O2 If) and b (O4 If/WN8), each with current masses of 100–150 $M_\odot$, plus O2–3 V stars R136a4 and a8. Once again, young ages of 0.6 ± 0.3 Myr are inferred for these stars, with the exception of R136b whose lower temperature suggests an age of ~ 1.5 Myr. Schnurr et al. (2009) have previously argued that R136b, offset by a projected distance of 0.5 pc is more evolved than other core members of R136 (though see appendix of Hainich et al. 2014).

Consequently, the HR diagram positions of the WN5h stars and the most luminous O stars in R136a favours very young ages. However, it should be emphasized that envelope inflation is implemented in the Bonn models, which is most pronounced for the most massive models (≥ 50 $M_\odot$), since these lie closest to the Eddington limit (Sanyal et al. 2015). Inflation moves isochrones to lower temperatures, such that younger ages are inferred for stars with models accounting for inflation, compared with those that do not.

Turning to the lower mass stars, all O2–6 stars lie between the 0–3 Myr isochrones in Fig. 10, although all stars do not lie along a

single isochrone. This is unsurprising given the approximate physical parameters of individual stars, initial rotation rate distributions, and uncertain binarity. For an extreme mass ratio system, the primary would completely dominate the spectrum of the system, so its location in the HR diagram would not be significantly displaced. In contrast, for a mass ratio of unity, individual stars would lie 0.3 dex lower in the HR diagram than the composite system, so the age would be overestimated. The effect would be modest for the highest mass systems at very young ages, but would become more significant for lower mass systems. Indeed, later O stars possess higher age estimates (3–6 Myr), although the inferred properties for such stars are least secure of the entire sample.

Our STIS/CCD data sets will help identify close binaries in R136 (Caballero-Nieves et al., in prep), while new *HST* Fine Guidance Sensor (FGS) observations – currently being analysed (GO 13477, PI, S.E. de Mink) – seek to reveal binaries with separations down to 0.02 arcsec (1000 AU), following on from Cycle 3 FGS observations of R136 (Lattanzi et al. 1994).

Individual age estimates follow solely from the position of stars in the HR diagram. We are in the process of analysing STIS/CCD data sets of R136a members, from which rotational velocities and helium abundances can be obtained. For the moment, He abundances for the WN5h stars are available (Crowther et al. 2010). From their luminosities and He-rich atmospheres, we can infer minimum ages since the surface helium mass fraction sets a lower limit to the core helium mass fraction. The minimum ages of R136a1–3 are 1–1.3 Myr, in reasonable agreement with results for the O stars. In order to simultaneously reproduce the high surface temperatures of the WN5hs stars, Bonn evolutionary models favour rapid initial rotation (~ 400 km s^{-1}), and ages of 1.1–1.6 Myr, as shown in Table 7. These results compare favourably with Crowther et al. (2010) who applied Geneva evolutionary models for VMS (Yusof et al. 2013), also requiring rapid rotation ($v_{\rm rot}/v_{\rm crit} = 0.4$ or $v_{\rm rot} \sim 400$ km s^{-1}) and ages of ~ 1.5 Myr (see Table 7). Details of the Bonn and Geneva codes differ significantly regarding the consideration of mixing, core overshooting and the treatment of envelope inflation. Both employ the metallicity-dependent Vink, de Koter & Lamers (2001) prescription for mass-loss on the main sequence, so estimates of $M_{\rm init}$ from current luminosities ought to be consistent, even if there are uncertainties in their validity for VMS (see Crowther et al. 2010; Gräfener & Vink 2013).

3.6 R136 cluster age and mass

Early estimates of the age of R136 were 3–4 Myr on the basis that the WN stars were classical He-burning stars. Subsequently, a lower age of <1–2 Myr was obtained once it was recognized that the WN stars are core H-burning stars, supported by a rich early O-type population (de Koter et al. 1998, Crowther & Dessart 1998). The most extensive study of massive stars to date has been by Massey & Hunter (1998) who inferred a very young age of ≤ 1 Myr using the Vacca, Garmany & Shull (1996) O star temperature scale, or ≤ 2 Myr from the Chlebowski & Garmany (1991) scale, although the majority of their sample was drawn from the R136 region, rather than R136a itself.

Here, we have combined the age estimates of 52 O stars in R136a (excluding WN5h stars) from BONNSAI to produce a probability density distribution, presented in Fig. 11, from which an age of $1.5^{+0.3}_{-0.7}$ Myr is obtained. The $\pm 1\sigma$ estimate represents the standard deviation in each bin of the age distribution computed with a bootstrapping method. As discussed above, lower ages are obtained

---

[2] BONNSAI is available at http://www.astro.uni-bonn.de/stars/bonnsai

Table 7. Comparison of mass and age estimates for the WN5h stars in R136a from Geneva (Crowther et al. 2010; Yusof et al. 2013) and Bonn (Köhler et al. 2015) based on physical and chemical abundances obtained by Crowther et al. (2010), incorporating the adjustment to the absolute magnitude for R136a2, as discussed in the present study.

| Star	T_* (kK)	$\log L$ ($L_\odot$)	X_H (per cent)	Code	M_{init} ($M_\odot$)	v_{init} (km s^{-1})	$M_{current}$ ($M_\odot$)	τ (Myr)
R136a1	53 ± 3	6.94 ± 0.09	–	Bonn	325^{+55}_{-45}	100^{+180}_{-60}	315^{+60}_{-50}	$0.0^{+0.3}_{-0.0}$
	53 ± 3	6.94 ± 0.09	40 ± 10	Bonn	315^{+50}_{-20}	440^{+20}_{-85}	280^{+35}_{-30}	0.8 ± 0.2
	53 ± 3	6.94 ± 0.09	40 ± 5	Geneva	320^{+100}_{-40}	400	265^{+80}_{-35}	$1.4^{+0.2}_{-0.1}$
R136a2	53 ± 3	6.63 ± 0.09	–	Bonn	195^{+35}_{-30}	100^{+325}_{-55}	190^{+35}_{-35}	$0.3^{+0.4}_{-0.3}$
	53 ± 3	6.63 ± 0.09	35 ± 5	Bonn	160^{+25}_{-20}	380^{+85}_{-20}	130^{+20}_{-20}	1.6 ± 0.2
	53 ± 3	6.63 ± 0.09	35 ± 5	Geneva	180^{+35}_{-30}	400	150^{+30}_{-25}	1.7 ± 0.1
R136a3	53 ± 3	6.58 ± 0.09	–	Bonn	180 ± 30	100^{+330}_{-55}	175^{+35}_{-35}	$0.3^{+0.4}_{-0.3}$
	53 ± 3	6.58 ± 0.09	40 ± 5	Bonn	155^{+25}_{-20}	370^{+80}_{-30}	130^{+25}_{-15}	1.5 ± 0.2
	53 ± 3	6.58 ± 0.09	40 ± 5	Geneva	165 ± 30	400	135^{+25}_{-20}	1.7 ± 0.1
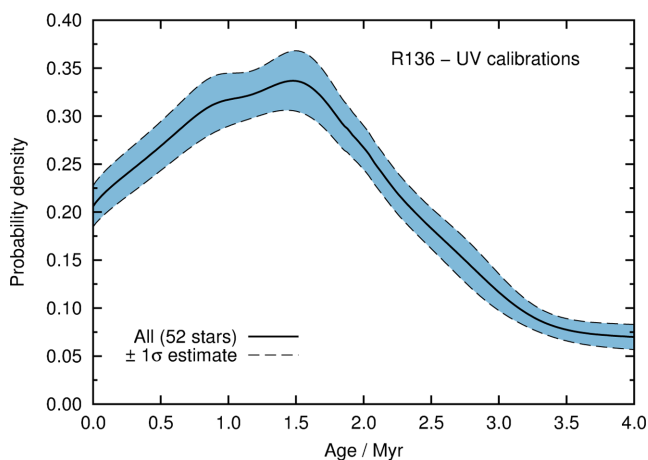
Figure 11. Probability density distribution of the apparent ages of UV-derived spectral types of individual O stars (excluding R136a1, a2, a3) based on BONNSAI (Schneider et al. 2014a) and main-sequence evolutionary models (Brott et al. 2011; Köhler et al. 2015), favouring an age of $1.5^{+0.3}_{-0.7}$ Myr. The shaded area is a bootstrapped $\pm 1\sigma$ estimate of the age distribution.

for the highest luminosity stars, although the treatment of envelope inflation for the most massive stars ($\gg 50 M_\odot$) remains uncertain.

Discrepant age estimates for massive stars in other young massive star clusters (e.g. Arches and Quintuplet in Galactic Centre) have been obtained from their Wolf–Rayet and O star contents, in the sense that the luminous WR stars possess apparent ages which are younger than O stars by 1–2 Myr (Martins et al. 2008; Liermann, Hamann & Oskinova 2012). Schneider et al. (2014b) have interpreted this as rejuvenation of the most massive stars through stellar mergers. Banerjee et al. (2012) have suggested the very luminous WN5h stars in R136 are post-merger systems. If this were the case, one might anticipate younger (apparent) age estimates for these rejuvenated stars with respect to the massive O star population.

R136 differs from the Quintuplet and Arches clusters in the sense that the luminous O stars also appear young, yet the He-enrichment of WN5h stars favours ages of ∼1.5 Myr and unusually rapid rotation, the latter predicted by stellar mergers (de Mink et al. 2013). According to Schneider et al. (2014b), the probability that the most massive star in a $5 \times 10^4 M_\odot$ star cluster is a binary product rises from 50 per cent at 1 Myr to 100 per cent at 3 Myr. However,

only the most massive system is anticipated to have merged after 1.5 Myr (four are anticipated after 3 Myr) for a Salpeter-type mass function in the core. Therefore, the youth of R136a does not support a scenario in which all the VMS are merger products. Indeed, as we discuss below, the mass within the central parsec is significantly lower than $5 \times 10^4 M_\odot$ further strengthening this conclusion. A more definitive answer to this question is deferred until the analysis of STIS/CCD data sets, but the apparent youth of the most luminous stars likely arises from the treatment of inflation in single star models than the physics of binary mergers.

A variety of mass estimates of R136 have been obtained. Hunter et al. (1995) infer a mass of $2.2 \times 10^4 M_\odot$ for stars with $>2.8 M_\odot$ out to a radius of 5 pc from *HST*/WFPC2, suggesting a total mass of ∼$5 \times 10^4 M_\odot$, while Andersen et al. (2009) derived a mass of $5 \times 10^4 M_\odot$ down to 2.1 $M_\odot$ out to a radius of 7 pc from *HST*/NICMOS. The actual mass of the R136 cluster may be somewhat lower, as it may suffer contamination from the surrounding halo of NGC 2070, for which Cignoni et al. (2015) infer a global mass of $9 \times 10^4 M_\odot$. Indeed, the two components contribute equally to the surface brightness at a radius of ∼5 pc from R136a1 according to Mackey & Gilmore (2003).

For a total cluster mass of $5 \times 10^4 M_\odot$, an initial mass function following Kroupa (2001) with an upper mass limit of 300 $M_\odot$, we would anticipate $10^4/1250 = 40$ stars with initial masses in excess of 50 $M_\odot$. Since only 25 stars with such high masses are observed within the central 0.5 pc radius, the actual R136a cluster mass may be somewhat lower. Of course, some massive stars may have been ejected from the cluster (e.g. VFTS 16; Evans et al. 2010). Fujii & Portegies Zwart (2011) suggest a few per cent of stars with ∼50 $M_\odot$ would be dynamically ejected from dense clusters of this mass. If we were to consider a radius of 5 pc, analogous to the region surveyed by Hunter et al. (1995), there are another ∼30 stars with masses in excess of 50 $M_\odot$ (from the census of Doran et al. 2013), supporting their high enclosed mass for the R136 'region'.

Sabbi et al. (2012) have proposed that R136 forms part of an ongoing merging binary cluster system within NGC 2070, on the basis of a clump of older stars located ∼5 pc to its NE (see also Cignoni et al. 2015). If this clump were to reflect stars in the process of dynamically accreting, one might expect older stars to have already merged with R136 itself (see Gieles 2013). Indeed, some of the apparently older O stars in R136 (e.g. R136 H73) may arise from this clump, although the determination of physical parameters for these late-type O stars awaits detailed spectroscopic analysis of

Table 8. Census of the most luminous ($\log (L/L_\odot) \geq 6.2$) objects in 30 Doradus, sorted by projected distance from R136a1, drawn from the present study, Crowther et al. (2010), Doran et al. (2013) or Bestenlehner et al. (2014). Initial mass estimates from BONNSAI (based upon estimated temperatures and luminosities) are limited to apparently main-sequence stars.

Star, Alias	r (pc)	Subtype	$\log L/L_\odot$	$M/M_\odot$	Ref
R136a1, H3	0.00	WN5h	6.94 ± 0.09	325^{+55}_{-45}	a
R136a2, H5	0.02	WN5h	6.63 ± 0.09	195^{+35}_{-30}	a, e
R136a5, H20	0.07	O2 If/WN5	$6.32^{+0.15}_{-0.16}$	106^{+30}_{-24}	e
R136a8, H27	0.10	O2–3 V	$6.28^{+0.13}_{-0.15}$	102^{+26}_{-22}	e
R136a4, H21	0.11	O2–3 V	$6.46^{+0.13}_{-0.15}$	132^{+37}_{-29}	e
R136a3, H6	0.12	WN5h	6.58 ± 0.09	180 ± 30	a, e
R136a6, H19	0.18	O2 If	$6.52^{+0.10}_{-0.05}$	158^{+35}_{-28}	e
R136b, H9	0.52	O4 If/WN8	$6.30^{+0.11}_{-0.12}$	100^{+22}_{-17}	e
R136c, H10	0.83	WN5h	6.75 ± 0.11	230^{+50}_{-45}	a
Mk 42, H2	1.96	O2 If	6.56 ± 0.1	170^{+40}_{-30}	d
Mk 34, H8	2.61	WN5h	6.85 ± 0.1	275^{+55}_{-45}	c
R134, BAT99-100	2.86	WN6(h)	6.2	–	d
Mk 37Wa, H11	2.86	O4 If	6.34 ± 0.1	110 ± 20	d
Mk 37Wb, H44	2.94	O2 If/WN5	6.21 ± 0.1	100 ± 15	d
Mk 39, VFTS 482	3.01	O2.5 If/WN6	6.4 ± 0.1	125^{+25}_{-20}	d
Mk 37, H14	3.02	O3.5 If/WN7	6.48 ± 0.1	140^{+40}_{-25}	d
Mk 35, VFTS 545	3.07	O2 If/WN5	6.3 ± 0.1	110 ± 20	d
Mk 30, VFTS 542	4.15	O2 If/WN5	6.16 ± 0.1	90 ± 15	d
Mk 25, VFTS 506	10.9	ON2 V((f*))	6.24 ± 0.1	100^{+20}_{-15}	d
R140b, BAT99-103	12.0	WN5(h)+O	6.4	–	d
Mk 51, VFTS 457	12.6	O3.5 If/WN7	6.2 ± 0.1	90 ± 15	d
R139, VFTS 527	16.2	O6.5 Iafc	6.3	>78	b
		O6 Iaf		>66	b
R145, VFTS 695	19.6	WN6h+	6.5	–	d
R135, VFTS 402	21.6	WN7h+OB	6.2	–	c
VFTS 682	29.8	WN5h	6.51 ± 0.1	155^{+30}_{-25}	d
R144, BAT99-118	62.3	WN5–6	6.4	–	c
		WN6–7		–	c
R147, VFTS 758	71.7	WN5h	6.36 ± 0.1	125^{+25}_{-20}	d
R146, VFTS 617	84.7	WN5ha	6.29 ± 0.1	115 ± 20	d
VFTS 16	120:	O2 III-If	6.23 ± 0.1	105^{+20}_{-15}	d

Notes. (a): Crowther et al. (2010); (b): Taylor et al. (2011); (c): Doran et al. (2013); (d): Bestenlehner et al. (2014); (e): This work.

our optical STIS/CCD data sets. The evolutionary status of some stars in the NE clump (e.g. Mk 33Sb, WC5) implies an apparent age of 3–4 Myr, providing these are coeval (Melnick 1985; Walborn & Blades 1997). The age of this region may be higher, should the highest luminosity stars be rejuvenated binary products.

3.7 Census of very luminous stars in 30 Doradus

Doran et al. (2013) have undertaken a study of the massive-star content of 30 Doradus, together with the contribution of R136 to the ionizing and mechanical feedback of the entire star-forming region, albeit reliant upon an incomplete census of R136 itself. We are now able to reassess the total number of very luminous stars in 30 Doradus, updated to include tailored parameters of massive stars from Bestenlehner et al. (2014) based on VFTS observations (Evans et al. 2011). Table 8 lists 29 stars within 30 Doradus which are more luminous than $\log (L/L_\odot) \approx 6.2$, corresponding to initial masses of $\sim 100\,M_\odot$ or more for zero age main-sequence stars. Only 9 (31 per cent) of the most luminous stars in 30 Doradus lie within R136 itself!

A similar number (10) of very luminous stars are located in the halo around R136, at projected distances of 1.5–5 pc[3] The other (11) high-luminosity stars in 30 Doradus lie $\geq$10 pc away from R136a1, approximately half within NGC 2070 and the remainder elsewhere. The majority of these are luminous WN-type stars (see also Bestenlehner et al. 2014; Hainich et al. 2014).

The overwhelming majority of the VMS in 30 Doradus are early O supergiants, transition Of/WN stars or luminous WN stars. Crowther et al. (2010) proposed that VMS may possess O-supergiant spectral appearances on the main sequence, owing to their proximity to the (classical) Eddington limit. However, R136 a4, a8 and Mk 25 indicate that very luminous O2–3 dwarf stars do exist despite having classical Eddington parameters of $\Gamma_e \sim 0.5$, based upon BONNSAI-derived masses.

4 INTEGRATED FAR-UV SPECTROSCOPY

UV spectroscopy of the central region of NGC 2070 was first obtained with IUE (e.g. Koornneef & Mathis 1981; Vacca et al. 1995), while the advent of *HST*/GHRS-permitted high-resolution spectroscopy (Walborn et al. 1992). The integrated R136 spectrum revealed prominent He II λ1640 emission, together with strong N V $\lambda\lambda$1238–42 and C IV $\lambda\lambda$1548–51 P Cygni features, with stellar Si IV $\lambda\lambda$1393–1402 absent.

Fig. 12 presents the integrated far-UV spectrum of R136 considering all sources up to 0.5 pc from R136a1. Its appearance closely reflects earlier descriptions, He II λ1640 emission is relatively strong ($W_\lambda \sim 4.5$ Å) and broad (FWHM $\sim$ 10 Å or 1800 km s^{-1}), so the integrated spectral morphology is closer to an Of/WN supergiant than a genuine WN star – recall fig. 4 of Walborn et al. (1992) which compares R136a to Melnick 42 (O2 If). A comparison between the 2 arcsec $\times$ 2 arcsec aperture GHRS/G140L observation of R136a from 1991 April (GO 1188, PI D.C. Ebbetts) and an equivalent region of our STIS data set reveals excellent agreement, and is morphologically identical to the integrated spectrum shown in Fig. 12 aside from a 30 per cent lower continuum flux.

Fig. 12 includes the co-added spectrum of all 70 stars for which $F_{1500} \geq 5 \times 10^{-15}$ erg s^{-1} cm^2 Å^{-1}, which collectively contribute $\sim$77 per cent of the integrated continuum flux, with the difference resulting from UV faint late O-type stars, plus the unresolved early B population. The cumulative spectrum of the seven most luminous members of R136a – each with inferred initial masses in excess of 100 $M_\odot$ – comprising three WN stars (a1–a3), one Of/WN star (a5), an O2 supergiant (a6) plus two O2–3 dwarfs (a4, a8) – is also included in Fig. 12. Collectively, these most closely resemble a weak lined mid-WN integrated star. It is apparent that the He II λ1640 emission line flux, and one third of the continuum flux originates from these few stars, the former dominated by R136a1–a3. The remaining 63 far-UV bright stars cumulatively resemble an early

---

[3] We have excluded VFTS 512 (O2 V) from the Doran et al. (2013) statistics since the luminosity obtained by Bestenlehner et al. (2014) is $\log (L/L_\odot) = 6.0$. Source 1222 from Parker (1993) has also been excluded owing to its O9 V spectral type from Walborn, Maíz Apellániz & Barbá (2002b), as has VFTS 1014 (Parker 863) despite Bestenhehner et al. obtaining $\log (L/L_\odot) = 6.2$ since this ARGUS spectrum is likely composite (O3 V + mid-/late O). Similarly, we favour the lower luminosities ($\log L/L_\odot = 6.0 - 6.1$) inferred by Doran et al. (2013) for R140a2 (WN5+O), Mk 49 (WN6) and BAT99-96 (WN8) over those by Hainich et al. (2014), who obtained significantly higher values by assuming the WR dominated the continuum flux (R140a2) or on the basis of high interstellar extinctions (Mk 49, BAT99-96).
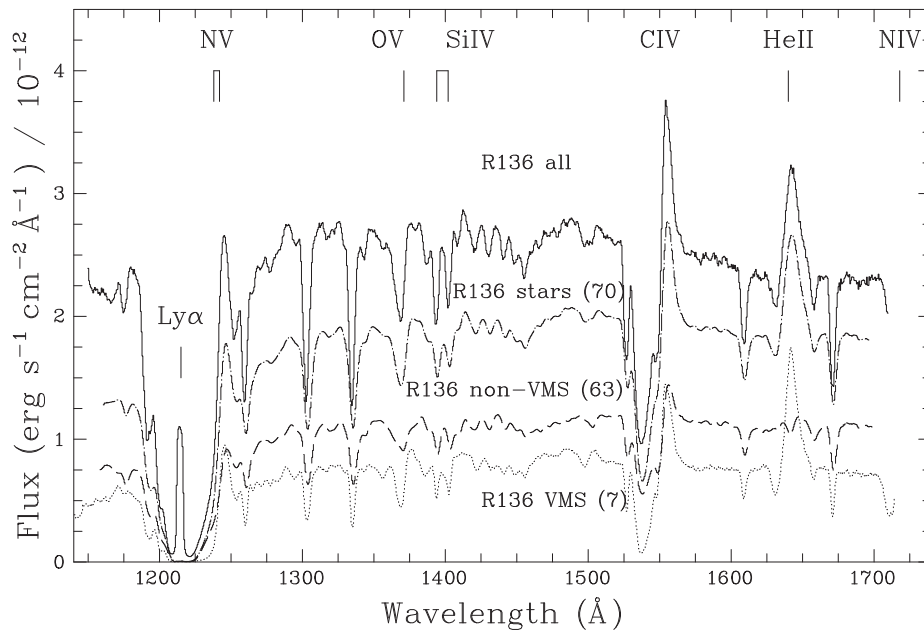
Figure 12. Integrated *HST*/STIS spectrum of all sources within 0.5 parsec of R136a1 (solid, all stars), the composite spectrum of all 70 bright stars with $F_{1500} \geq 5 \times 10^{-15}$ erg s^{-1} cm^{-2} Å^{-1} (dot–dashed), comprising seven very massive stars (VMS, dotted), and the remaining 63 far-UV bright stars (dashed). He II $\lambda 1640$ emission in R136 is totally dominated by VMS. The difference between the 'stars' and 'all' arises from the contribution from UV faint O late-type stars and unresolved early B stars.

non-supergiant O star, with prominent O V $\lambda 1371$, and P Cygni N V $\lambda\lambda 1238$–42, C IV $\lambda\lambda 1548$–51.

It is apparent that prominent He II $\lambda 1640$ emission in R136 arises from the presence of VMS (initial masses $\geq 100\,\mathrm{M_\odot}$). Usually, the upper mass limit assumed in population synthesis models is $100\,\mathrm{M_\odot}$, so a synthetic model for R136 would fail to reproduce its He II $\lambda 1640$ emission. Indeed, if this feature is observed in the integrated light of sufficiently young (unresolved) high-mass star clusters, one might legitimately conclude that the stellar mass function extends well beyond 100 $\mathrm{M_\odot}$.

At very young ages, early O stars will dominate the UV appearance of massive clusters, so strong O V $\lambda 1371$ absorption will be present. The absence of mid- to late O supergiants will ensure that P Cygni Si IV $\lambda\lambda 1393$–1402 is absent. At later ages (3–5 Myr) O V will weaken while Si IV will strengthen, plus He II $\lambda 1640$ from classic WR stars will appear. Therefore, the simultaneous presence of O V absorption, He II emission together with the absence of P Cygni Si IV would suggest both a very young age and the presence of VMS. To date, the most promising example of such a star cluster is A1 within NGC 3125 (Chandar et al. 2004; Hadfield & Crowther 2006; Wofford et al. 2014).

In addition, since our data sets enable spatially resolved spectroscopy of the constituents of R136, we are able to quantify the contribution of individual stars to the integrated UV continuum. five stars brighter than $m_{F555W} = 17.0$ mag located within 2.05 arcsec of R136a1 lie beyond our STIS slit spectroscopy, so we have estimated their fluxes by adopting an average F_{1500}/F_{F555W} ratio from cluster members; they are presented in parentheses in Tables 4 and B1. We estimate ~ 2 per cent of the integrated UV flux originates from these stars, primarily R136 H39 (O3 V+O5.5 V, Massey et al. 2002).

Fig. 13 presents the cumulative 1500 Å flux of R136a to a radius of 0.5 pc, versus a ranked list of the 70 far-UV brightest stars in this region. The three brightest sources alone (R136a1-a3) contribute 20 per cent of the far-UV continuum flux, while the 18 brightest
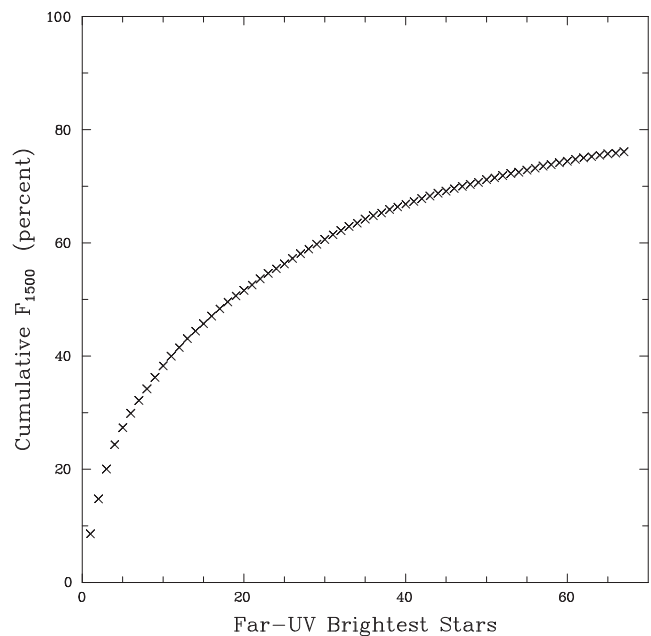

Figure 13. Cumulative F_{1500} flux for the brightest 70 far-UV sources within 2.05 arcsec (0.5 pc) of R136a1, including estimates for stars beyond our slit spectroscopy. The three WN stars R136a1–a3 contribute 20 per cent of the total, while collectively the 18 brightest far-UV sources provide 50 per cent of the integrated continuum flux.

far-UV sources provide 50 per cent of the integrated far-UV flux. Walborn et al. (1992) cite an higher (pre-COSTAR) estimate of 40 per cent for R136a1–a3 from GHRS acquisition images, according to D. Ebbets and E. Malumuth.

5 SUMMARY

We have introduced a census of the visually brightest members of the R136 star cluster based on new long-slit *HST*/STIS spectroscopy. We have obtained UV, blue visual and Hα spectroscopic data sets using 17 contiguous 52 arcsec × 0.2 arcsec slits sampling the core of R136. In this study, we reveal the following.

(i) We classify 51 of the 57 stars brighter than $m_{F555W} = 16.0$ mag within a radius of 0.5 pc of R136a1 based on their UV spectroscopic morphology. We confirm previous results of Massey & Hunter ([1998](#)) that the bulk of the visually brightest members of R136 are O2–3 stars. For the first time, we classify all Weigelt & Baier ([1985](#)) stars within R136a, which comprise three WN5 stars (a1–a3), two O supergiants (a5–a6) and three early O dwarfs (a4, a7–a8). Eight additional sources are spectrally classified within the central ∼pc, including R136b (O4 If/WN8).

(ii) We obtain wind terminal velocities from measurements of v_{black} (or v_{edge}) from P Cygni C IV λλ1548–51 profiles, from which we obtain average O2–3 wind velocities of 2750 and 3120 km s^{-1} for dwarfs and (super)giants, respectively. Comparisons with early O dwarfs elsewhere in the LMC and Milky Way indicate somewhat lower wind velocities in R136.

(iii) We estimate physical parameters for the visually brightest members of R136 based on the temperature calibration of LMC O-type stars from Doran et al. ([2013](#)) and exploit BONNSAI (Schneider et al. [2014a](#)) to estimate masses and ages based on rotating evolutionary models appropriate for the LMC (Brott et al. [2011](#); Köhler et al. [2015](#)). Three WN stars (R136a1–a3), two Of/WN stars (R136a5 and R136b), newly identified O2 If R136a6 and O2–3 V stars R136a4 and a8 possess initial masses ≥100 M$_\odot$.

(iv) We obtain a cluster age of $1.5^{+0.3}_{-0.7}$ Myr from the O star content, which is consistent with that estimated for the luminous WN5h stars by Crowther et al. ([2010](#)), although apparent ages of these and other luminous O stars is 0.6 ± 0.3 Myr, likely to arise from the treatment of envelope inflation in evolutionary models (Sanyal et al. [2015](#)), rather than rejuvenation following binary mergers. The mass and youth of R136a indicate that no more than the most massive system is potentially a binary product (Schneider et al. [2014b](#)). More definitive conclusions await analysis of STIS/CCD spectroscopy, permitting rotation rates and He abundances of O stars to be obtained. We identify 25 stars more massive than 50 M$_\odot$ within 0.5 pc of R136a1 indicating a lower enclosed mass than previous estimates, although reasonable consistency is achieved with respect to Hunter et al. ([1995](#)) and Andersen et al. ([2009](#)) in the R136 'region' from the total number of high-mass stars within a 5 pc radius.

(v) Incorporating results from our earlier VFTS-based census (Doran et al. [2013](#); Bestenlehner et al. [2014](#)) we estimate a total of 29 stars more luminous than $\log(L/L_\odot) = 6.2$ in the entire 30 Doradus nebula, of which 26 possess O2–4 If, Of/WN or WN subtypes. Only 9 stars are located within R136 itself, with an additional 9 stars within the extended halo, 1.5–5 pc away from R136a1 (Melnick [1985](#)) and another 11 stars at much greater distance (10–120 pc).

(vi) We have also considered the integrated UV spectrum of R136a in the context of its constituent members. The prominent He II λ1640 emission feature arises primarily from the most massive stars. Specifically, close to 100 per cent of the He II λ1640 flux and 32 per cent of the far-UV continuum originates in the seven stars for which we estimate (initial) masses above 100 M$_\odot$, the former dominated by from R136a1–a3. Usually, such stars are neglected in conventional population synthesis models. Prominent He II λ1640 emission in the integrated spectrum of suitably young star clusters – prominent O V λ1371 absorption without strong Si IV λλ1393, 1402P

Cygni emission – would favour a mass function that extends well above this value. Indeed, extremely strong λ1640 emission in cluster A1 within NGC 3125 favours extremely massive stars therein (Chandar et al. [2004](#); Hadfield & Crowther [2006](#); Wofford et al. [2014](#)).

In future papers in this series, we will present the corresponding blue, visual and Hα STIS/CCD spectroscopic data sets. These will be used to refine spectral classifications, obtain more robust physical and wind properties, and search for close binary systems. These will enable a refined Hertzsprung–Russell diagram for R136a. The multi-epoch nature of the CCD data sets will enable an attempt at identifying close binaries (see Cottaar & Hénault-Brunet [2014](#)), together new *HST* FGS observations of R136a (S.E. de Mink, P.I.).

REFERENCES

Andersen M., Zinnecker H., Moneti A., McCaughrean M. J., Brandl B., Brandner W., Meylan G., Hunter D., 2009, ApJ, 707, 1347

Banerjee S., Kroupa P., Oh S., 2012, MNRAS, 426, 1416

Bestenlehner J. et al., 2011, A&A, 530, L14

Bestenlehner J. et al., 2014, A&A, 570, A38

Bostroem K. A., Proffitt C., 2011, STIS Data Handbook v6.0. Baltimore, STScI

Brott I. et al., 2011, A&A, 530, A115

Campbell M. A., Evans C. J., Mackey A. D., Gieles M., Alves J., Ascenso J., Bastian N., Longmore A. J., 2010, MNRAS, 405, 421

Cassinelli J. P., Mathis J. S., Savage B. D., 1981, Science, 212, 1497

Chandar R., Leitherer C., Tremonti C. A., 2004, ApJ, 604, 153

Chlebowski T., Garmany C. D., 1991, ApJ, 368, 241

Cignoni M. et al., 2015, ApJ, 811, 76

Conti P. S., Garmany C. D., Massey P., 1986, AJ, 92, 48

Cottaar M., Hénault-Brunet V., 2014, A&A, 562, A20

Crowther P. A., Dessart L., 1998, MNRAS, 296, 622

Crowther P. A., Walborn N. R., 2011, MNRAS, 416, 1311

Crowther P. A., Hillier D. J., Evans C. J., Fullerton A. W., De Marco O., Willis A. J., 2002, ApJ, 579, 774

Crowther P. A., Schnurr O., Hirschi R., Yusof N., Parker R. J., Goodwin S. P., Kassim H. A., 2010, MNRAS, 408, 731

de Koter A., Hubeny I., Heap S. R., Lanz T., 1994, ApJ, 435, L71

de Koter A., Heap S. R., Hubeny I., 1997, ApJ, 477, 792

de Koter A., Heap S. R., Hubeny I., 1998, ApJ, 509, 879

de Marchi G., Nota A., Leitherer C., Ragazzoni R., Barbieri C., 1993, ApJ, 419, 658

de Marchi G. et al., 2011, ApJ, 739, 27

de Mink S. E., Langer N., Izzard R. G., Sana H., de Koter A., 2013, ApJ, 764, 166

Doran E. I. et al., 2013, A&A, 558, A134

Evans C. J. et al., 2010, ApJ, 715, L74

Evans C. J. et al., 2011, A&A, 530, A108

Feast M. W., Thackeray A. D., Wesselink A. J., 1960, MNRAS, 121, 337

Feitzinger J. V., Schlosser W., Schmidt-Kaler T., Winkler C., 1980, A&A, 84, 50

Feitzinger J. V., Hanuschik R. W., Schmidt-Kaler T., 1983, A&A, 120, 269

Figer D. F., 2005, Nature, 434, 192

Fujii M. S., Portegies Zwart S., 2011, Science, 334, 1380

Garcia M., Herrero A., Najarro F., Lennon D. J., Urbaneja M. A., 2014, ApJ, 788, 64

Gieles M., 2013, in proc. Massive Stars: From α to Ω, (available at: http://a2omega-conference.net/Presentations/Session1/SessionI_3_Gieles.pdf)

Gondhalekar P. M., Willis A. J., Morgan D. H., Nandy K., 1980, MNRAS, 193, 875

Gräfener G., Vink J. S., 2013, A&A, 560, A6

Groenewegen M. A. T., Lamers H. J. G. L. M., 1989, A&AS, 79, 359

Groenewegen M. A. T., Lamers H. J. G. L. M., Pauldrach A. W. A., 1989, A&A, 221, 78

Hadfield L. J., Crowther P. A., 2006, MNRAS, 368, 1822

Hainich R. et al., 2014, A&A, 565, A27

Hénault-Brunet V. et al., 2012, A&A, 546, A73

Hillier D. J., Lanz T., Heap S. R., Hubeny I., Smith L. J., Evans C. J., Lennon D. J., Bouret J. C., 2003, ApJ, 580, 1039

Howarth I. D., 1983, MNRAS, 203, 301

Howarth I. D., Phillips A. P., 1986, MNRAS, 222, 809

Howarth I. D., Siebert K. W., Hussain G. A. J., Prinja R. K., 1997, MNRAS, 284, 265

Hunter D. A., Shaya E. J., Holtzman J. A., 1995, ApJ, 448, 179

Knigge C., Dieball A., Maíz Apellániz J., Long K. S., Zurek D. R., Shara M. M., 2008, ApJ, 683, 1006

Köhler K. et al., 2015, A&A, 573, A71

Koornneef J., Mathis J. S., 1981, ApJ, 245, 49

Kroupa P., 2001, MNRAS, 322, 231

Lamers H. J. G. L. M., Snow T. P., Lindholm D. M., 1995, ApJ, 455, 289

Lattanzi M. G. et al., 1994, ApJ, 327, L21

Leitherer C., Robert C., Drissen L., 1992, ApJ, 401, 596

Leitherer C., Tremonti C. A., Heckman T. M., Calzetti D., 2011, AJ, 141, 37

Liermann A., Hamann W.-R., Oskinova L. M., 2012, A&A, 540, A14

Mackey A. D., Gilmore G. F., 2003, MNRAS, 338, 85

Maíz Apellániz J., 2004, PASP, 116, 859

Maíz Apellániz J., 2005, HST Instrument Science Report STIS 2005-02

Maíz Apellániz J. et al., 2014, A&A, 564, A63

Martins F., Schaerer D., Hillier D. J., 2005, A&A, 436, 1049

Martins F., Hillier D. J., Paumard T., Eisenhauer F., Ott T., Genzel R., 2008, A&A, 478, 219

Massa D., Fullerton A. W., Sonneborn G., Hutchings J. B., 2003, ApJ, 586, 996

Massey P., Hunter D. A., 1998, ApJ. 493, 180

Massey P., Penny L. R., Vukovich J., 2002, ApJ, 565, 982

Massey P., Bresolin F., Kudritzki R.-P., Puls J., Pauldrach A. W. A., 2004, ApJ, 608, 1001

Massey P., Puls J., Pauldrach A. W. A., Bresolin F., Kudritzki R.-P., Simon T., 2005, ApJ, 627, 477

Massey P., Zangari A. M., Morrell N. I., Puls J., DeGioia-Eastwood K., Bresolin F., Kudritzki R.-P., 2009, ApJ, 692, 618

Melnick J., 1985, A&A, 152, 235

Pietrzyński G. et al., 2013, Nature, 495, 76

Portegies Zwart S. F., McMillan S. L. W., Gieles M., 2010, ARA&A, 48, 431

Prinja R. K., Crowther P. A., 1998, MNRAS, 300, 828

Prinja R. K., Barlow M. J., Howarth I. D., 1990, ApJ, 361, 607

Ramírez-Agudelo O. H. et al., 2013, A&A, 560, A29

Robert C., Pellerin A., Aliosi A., Leitherer C., Hoopes C., Heckman T. M., 2003, ApJS, 144, 21

Sabbi E. et al., 2012, ApJ, 754, L37

Sanyal D., Grassitelli L., Langer N., Bestenlehner J. M., 2015, A&A, 580, A20

Schneider F. R. N., Langer N., de Koter A., Brott I., Izzard R. G., Lau H. B. B., 2014a, A&A, 570, A66

Schneider F. R. N. et al., 2014b, ApJ, 780, 117

Schneider F. R. N., Izzard R. G., Langer N., de Mink S. E., 2015, ApJ, 805, 20

Schnurr O., Caroli J., Chené A.-N., Moffat A. F. J., St-Louis N., 2008, MNRAS, 389, L38

Schnurr O., Chené A.-N., Casoli J., Moffat A. F. J., St-Louis N., 2009, MNRAS, 397, 2049

Seaton M. J., 1979, MNRAS, 187, P73

Selman F. J., Melnick J., 2013, A&A, 552, A94

Shapley A. E., Steidel C. C., Adelberger K. L., Pettini M., 2003, ApJ, 588, 65

Smith Neubig M. M., Bruhweiler F. C., 1999, AJ, 117, 2856

Tatton B. L. et al., 2013, A&A, 554, A33

Taylor W. D. et al., 2011, A&A, 530, L10

Vacca W. D., Robert C., Leitherer C., Conti P. S., 1995, ApJ, 444, 647

Vacca W. D., Garmany C. D., Schull J. M., 1996, ApJ, 460, 914

Vink J. S., de Koter A., Lamers H. J. G. L. M., 2001, A&A, 369, 574

Walborn N. R., 1973, ApJ, 182, L21

Walborn N. R., 1977, ApJ, 215, 53

Walborn N. R., Blades J. D., 1997, ApJS, 112, 457

Walborn N. R., Nichols-Bohlin J., Panek R. J., 1985, International Ultraviolet Explorer Atlas of O-Type Spectra from 1200 to 1900 Å, NASA RP 1155

Walborn N. R., Ebbets D. C., Parker J.Wm, Nichols-Bohin J., White R. L., 1992, ApJ, 393, L13

Walborn N. R., Lennon D. J., Haser S. M., Kudritzki R.-P., Voels S. A., 1995, PASP, 107, 104

Walborn N. R. et al., 2002a, AJ, 123, 2754

Walborn N. R., Maíz Apellániz J., Barbá R. H., 2002b, AJ, 124, 1601

Walborn N. R., Fullerton A. W., Crowther P. A., Bianchi L., Hutchings J. B., Pellerin A., Sonneborn G., Willis A. J., 2002c, ApJS, 141, 433

Walborn N. R., Morrell N. I., Howarth I. D., Crowther P. A., Lennon D. J., Massey P., Arias J. I., 2004, ApJ, 608, 1028

Walborn N. R. et al., 2010, AJ, 139, 1283

Weigelt G., Baier G., 1985, A&A, 150, L18

Wofford A., Leitherer C., Chandar R., Bouret J.-C., 2014, ApJ, 781, 122

Yusof N. et al., 2013, MNRAS, 433, 1114

APPENDIX A: UV ATLAS OF LMC O STARS

In this appendix, we present an UV atlas of LMC O stars, primarily obtained with the FOS or STIS instruments of *HST*. A log of observations is presented in Table A1 , with morphological sequences for O dwarfs, giants and supergiants presented in Figs A1–A4. Luminosity sequences for O2–O9+ stars are presented in Figs A5–A11. More extensive IUE SWP/LORES atlases for LMC OB stars are presented by Smith Neubig & Bruhweiler (1999).

Table A1. Log of ultraviolet spectroscopic observations used in the LMC O star montages.

Star	Alias	Sp type	Ref	Tel	Inst	*HST* GO/PI	Ref	Fig.
BI 237		O2 V	W02b	*HST*	STIS/G140L	9412/Massey	M04	A1, A5
R136 H35		O3 V	CN16	*HST*	STIS/G140L	12465/Crowther	This study	A1, A6
LH 81/W28-23		O3.5 V((f+))	M05	*HST*	STIS/G140L	9412/Massey	M05	A1, A7
LH 81/W28–5		O4 V((f+))	M04	*HST*	STIS/G140L	8633/Massey	M04	6
R136 H78		O4: V	CN16	*HST*	STIS/G140L	12465/Crowther	This study	A1, A8
Sk-70° 60		O4–5 V((f))	M09	*HST*	FOS/G130H	5444/Robert	PC98	6
LH 58-496	LH58-10a	O5 V(f)	M05	*HST*	STIS/G140L	9412/Massey	M05	6
R136 H70		O5 Vz	CN16	*HST*	STIS/G140L	12465/Crowther	This study	A1, A2
Sk–70° 69		O5.5 V((f))	M09	*HST*	FOS/G130H	2233/Kudritzki	W95	6
R136 H123		O6 V	CN16	*HST*	STIS/G140L	12465/Crowther	This study	A2, A9
R136 H134		O7 Vz	CN16	*HST*	STIS/G140L	12465/Crowther	This study	A2, A10
R136 H80		O8 V	CN16	*HST*	STIS/G140L	12465/Crowther	Ths study	A2, A10
R136 H121		O9.5 V	CN16	*HST*	STIS/G140L	12465/Crowther	This study	A2, A11
HDE 269810	Sk–67° 211	O2 III(f)	W02b	*HST*	FOS/G130H	4110/Kudritzki	W95	A3, A5
R136 H48		O2–3 III	CN16	*HST*	STIS/G140L	12465/Crowther	This work	A3, A6
LH90 ST2-22		O3.5 III(f+)	M05	*HST*	STIS/G140L	9412/Massey	M05	A3, A7
HDE 269676	Sk–71° 45	O4–5 III	W77	IUE	SWP/HIRES	Nandy	G80	A3, A8
Sk–66° 100		O6 II(f)	W95	*HST*	FOS/G130H	2233/Kudritzki	W95	A3, A9
Sk–67° 101		O8 II(f)	R03	*HST*	STIS/E140M	7299/Bomans	M03	A3, A10
R136 H36		O2 If	CN16	*HST*	STIS/G140L	12465/Crowther	This study	A4, A5
Sk–65° 47	LH 43-18	O4 I(n)f+p	W10	*HST*	STIS/G140L	9412/Massey	M05	A4, A8
Sk–67° 111		O6 Ia(n)fpv	W02a	*HST*	STIS/E140M	12218/Massa		A4, A9
HDE 270952	Sk–65° 22	O6 Iaf+	W77	IUE	SWP/HIRES		C02	A9
Sk–69° 50		O7(n)(f)p	W10	*HST*	STIS/E140M	12218/Massa		A10
HDE 269702	Sk–67° 168	O8 I(f)p	W10	*HST*	STIS/E140M	12218/Massa		A4, A10
Sk–69° 124		O9 Ib	C86	*HST*	FOS/G130H	5444/Robert	PC98	A11
Sk–66° 169		O9.7 Ia+	F88	IUE	SWP/HIRES	Patriarchi	C02	A4, A11
Sk–68° 41		B0.5 Ia	F88	*HST*	FOS/G130H	4110/Kudritzki	W95	A11
Sk–67° 22		O2 If/WN5	CW11	*HST*	STIS/G140L	9412/Massey	M05	A5
Mk 39	R136 H7	O2.5 If/WN6	CW11	*HST*	STIS/G140L	9412/Massey	M05	A6
Mk 37	R136 H14	O3.5 If/WN7	CW11	*HST*	STIS/G140L	9412/Massey	M05	A7

Notes. C86: Conti, Garmany & Massey 1986; C02: Crowther et al. 2002; CW11: Crowther & Walborn 2011; CN16: Caballero-Nieves et al. (in preparation); G80: Gondhalekar et al. 1980; M03: Massa et al. 2003; M04: Massey et al. 2004; M05: Massey et al. 2005; M09: Massey et al. 2009; PC98: Prinja & Crowther 1998; R03: Robert et al. 2003; W77: Walborn 1977; W95: Walborn et al. 1995; W02a: Walborn et al. 2002c; W02b: Walborn et al. 2002a; W10: Walborn et al. 2010.
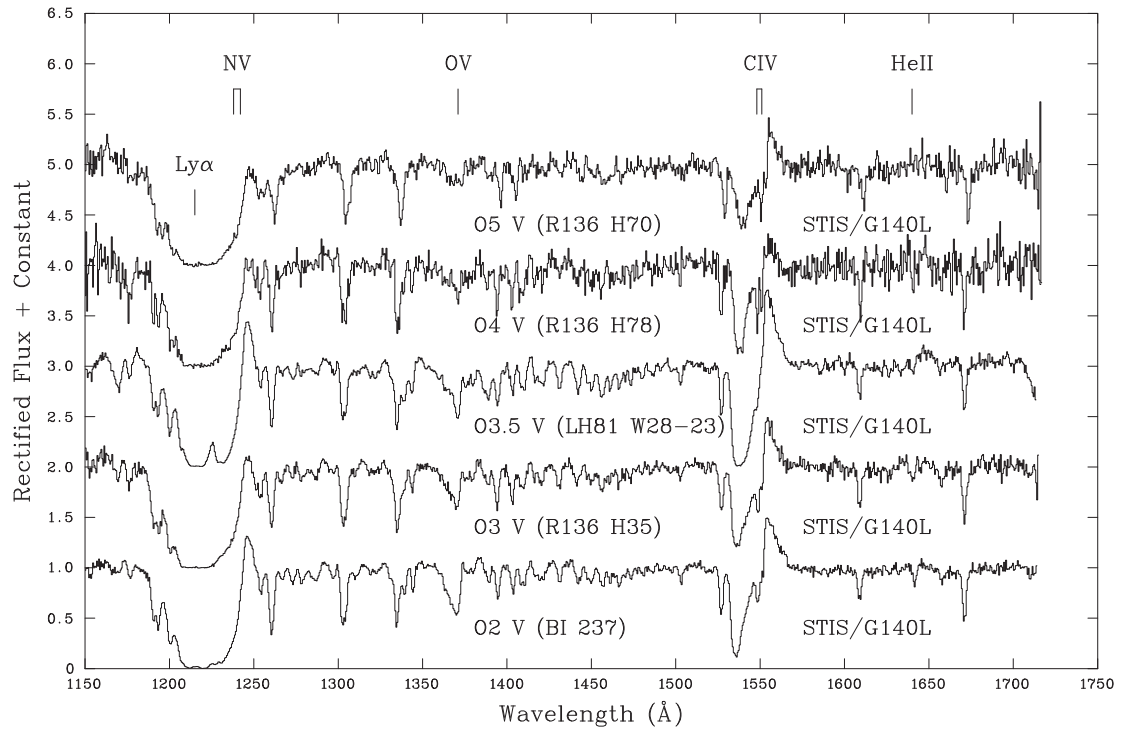
Figure A1. Ultraviolet morphological progression of O2–5 dwarfs, showing strong, broad O v λ1371 absorption at O2–3, together with strong P Cygni N v λλ1238–42 and C IV λλ1548-51. O v weakens at O3.5 and disappears at O4, while C IV P Cygni weakens at O5.
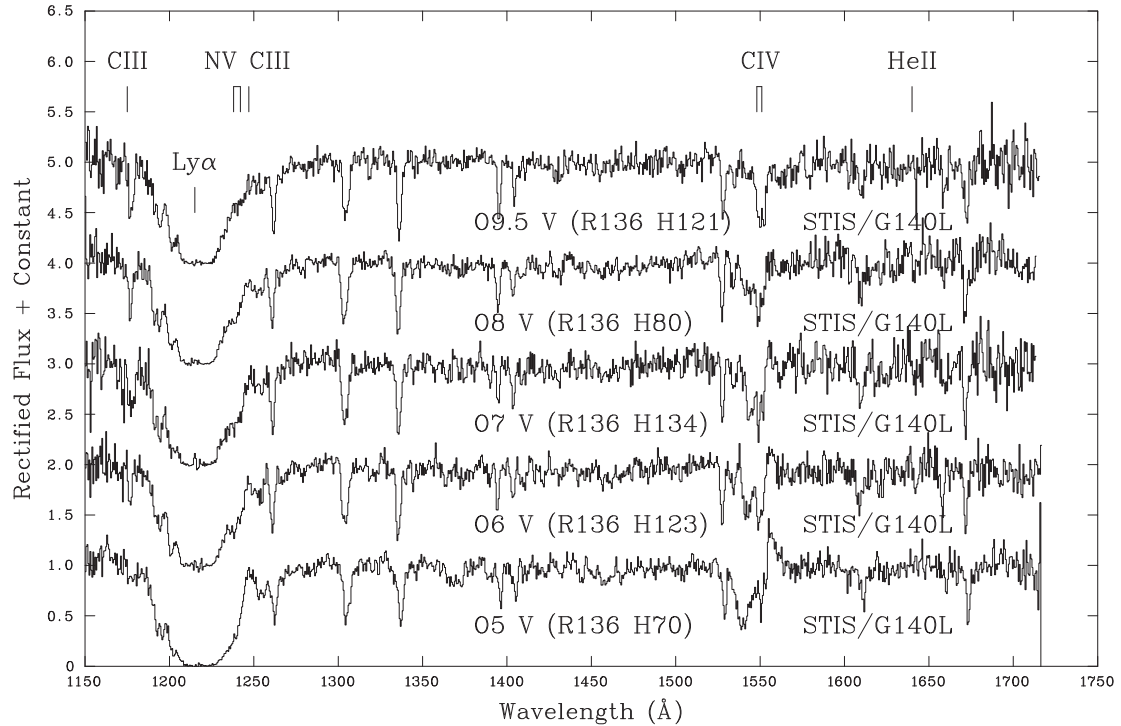

Figure A2. Ultraviolet morphological progression of O5–9.5 dwarfs, showing prominent broad, unsaturated P Cygni C IV λλ1548–51 at O5 V, which weakens in both emission strength and absorption width at O6–7 V and becomes photospheric at O9.5V. N v λλ1238–42 is apparent at O5 V but also weakens at O6–8 V and is undetected at O9.5 V.
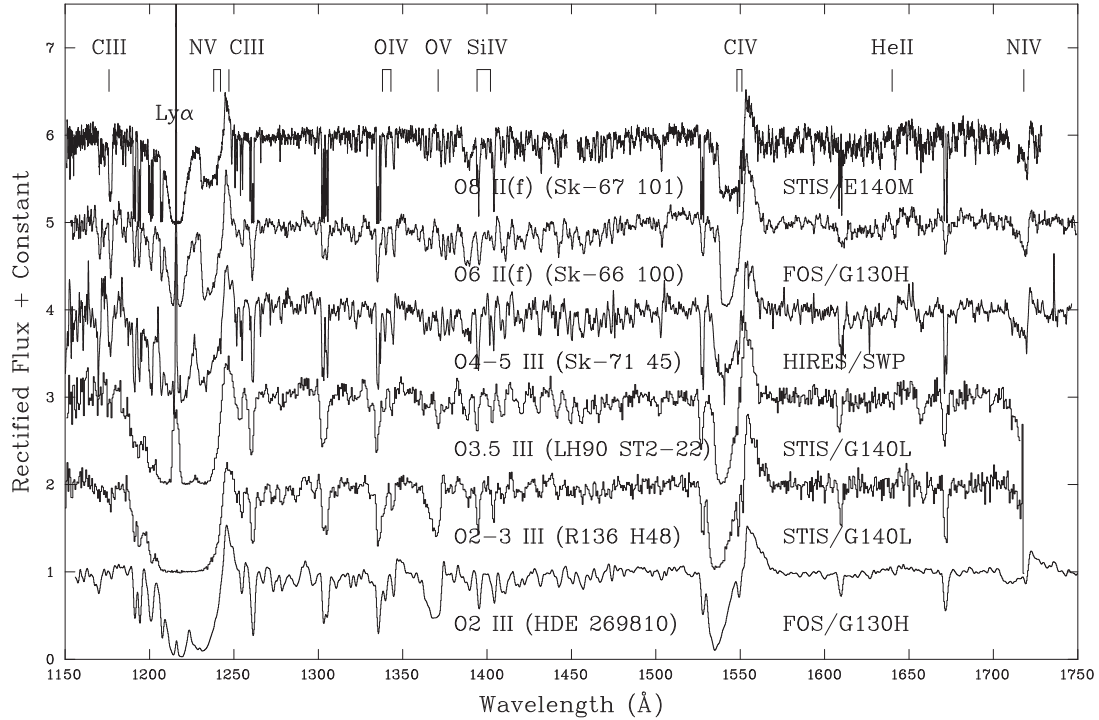
Figure A3. Ultraviolet morphological progression of O2–8 giants, showing strong, broad O v λ1371 absorption at O2–3, with prominent N v λλ1238–42 and C IV λλ1548–51 P Cygni profiles until O6 giants, and unsaturated thereafter.
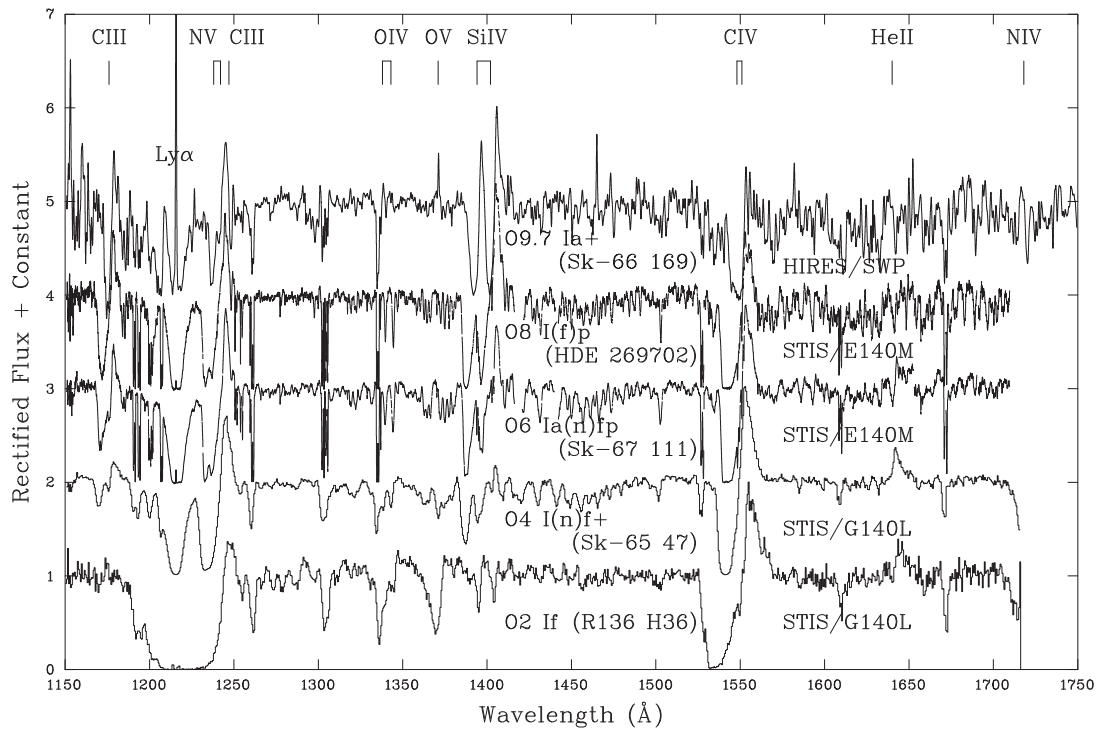

Figure A4. Ultraviolet morphological progression of O2–9.7 supergiants, showing prominent O v λ1371 absorption at O2, strong, saturated C IV λλ1548–51 P Cygni profiles until O8 supergiants, Si IV λλ1393–1402 P Cygni appearing weakly at O4 and saturating for O6 and later subtypes. He II λ1640 emission is prominent between O2 and 6, but thereafter blended with iron forest features.
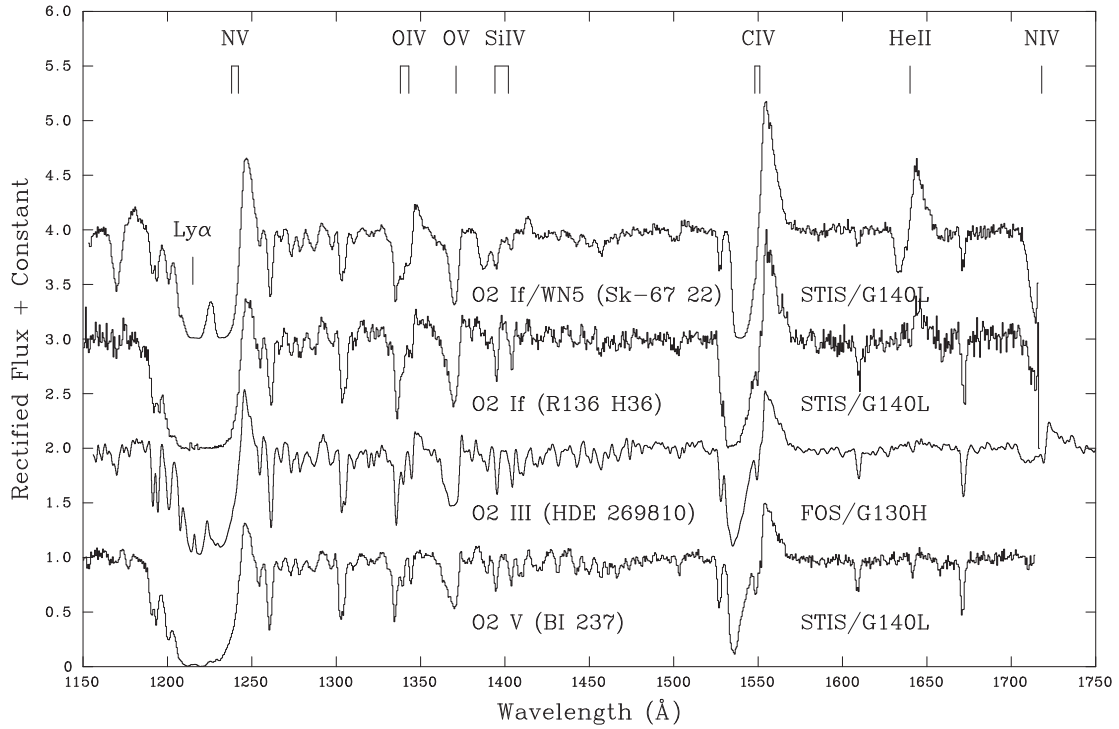
Figure A5. Montage of O2 luminosity sequence. Strong/broad O v λ1371 absorption is common to all O2 subtypes. C iv λλ1548–51 and N v λλ1238–42 are prominent P Cygni profiles at all luminosity classes, although the former is unsaturated in dwarfs/giants. Note the reversal in the He ii λ1640 line from absorption to strong P Cygni emission from dwarf to Of/WN.
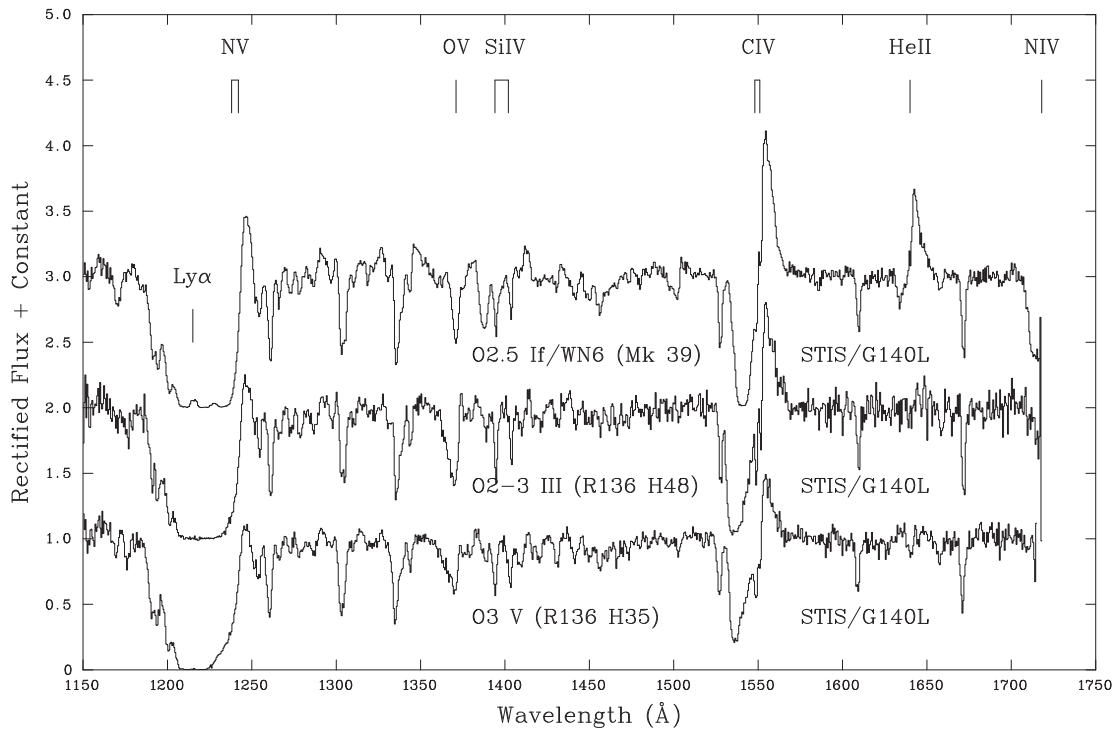
Figure A6. Montage of O2–3 luminosity sequence. O v λ1371 absorption is common to all luminosity classes. Note the reversal in the He ii λ1640 line from absorption to strong P Cygni emission from dwarf to Of/WN.
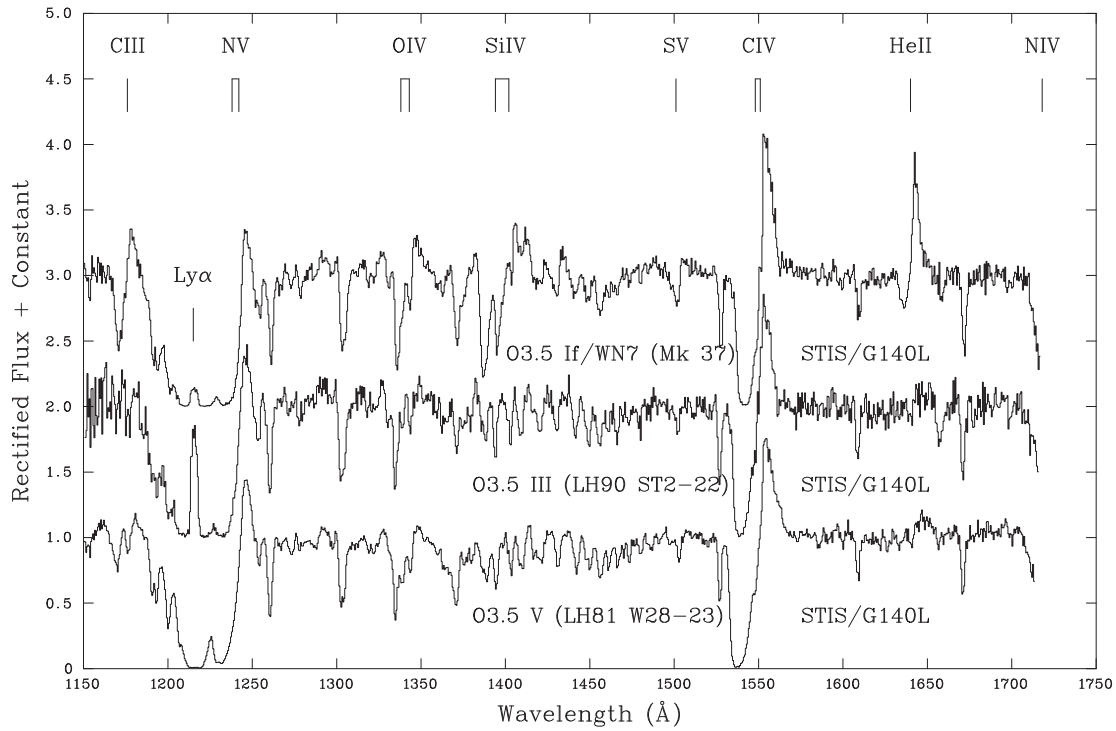
Figure A7. Montage of O3.5 luminosity sequence. O v λ1371 absorption weakly is present, with Si IV λλ1393–1402 P Cygni appearing in Of/WN stars together with prominent He II λ1640 P Cygni emission.
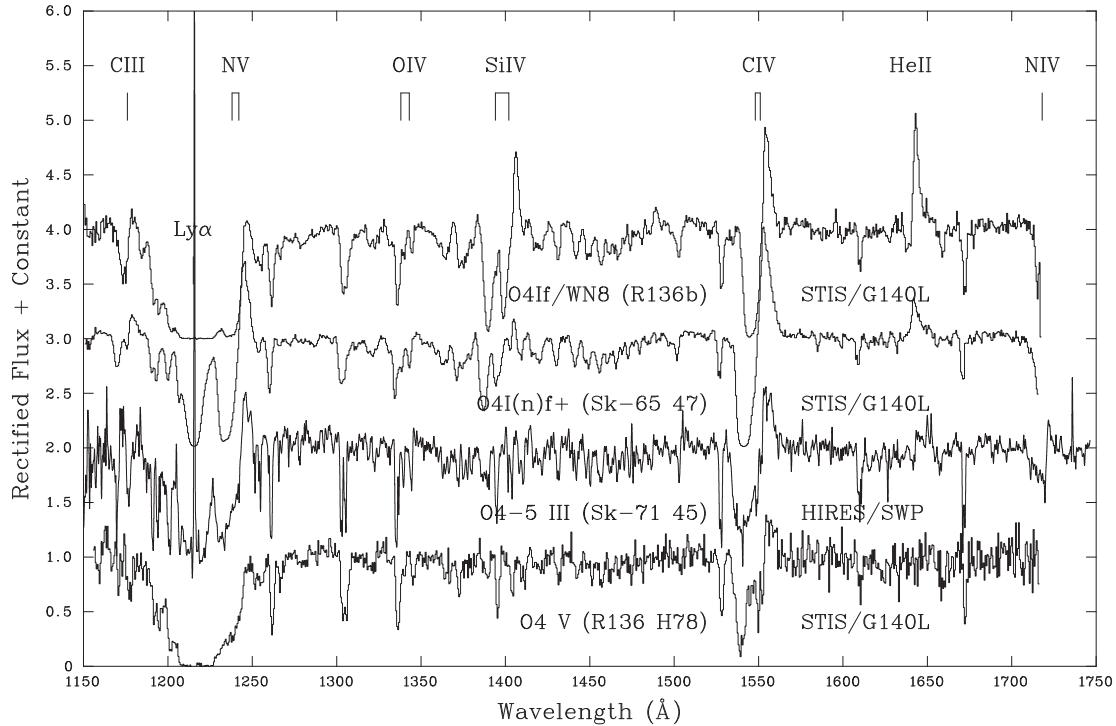
Figure A8. Montage of O4–5 luminosity class. O v λ1371 absorption is absent, although P Cygni N v λλ1238–42 and C IV λλ1548–51 remain prominent for all classes, albeit unsaturated in dwarfs/giants. P Cygni Si IV λλ1393–1402 and He II λ1640 emission are seen in O4 supergiants.
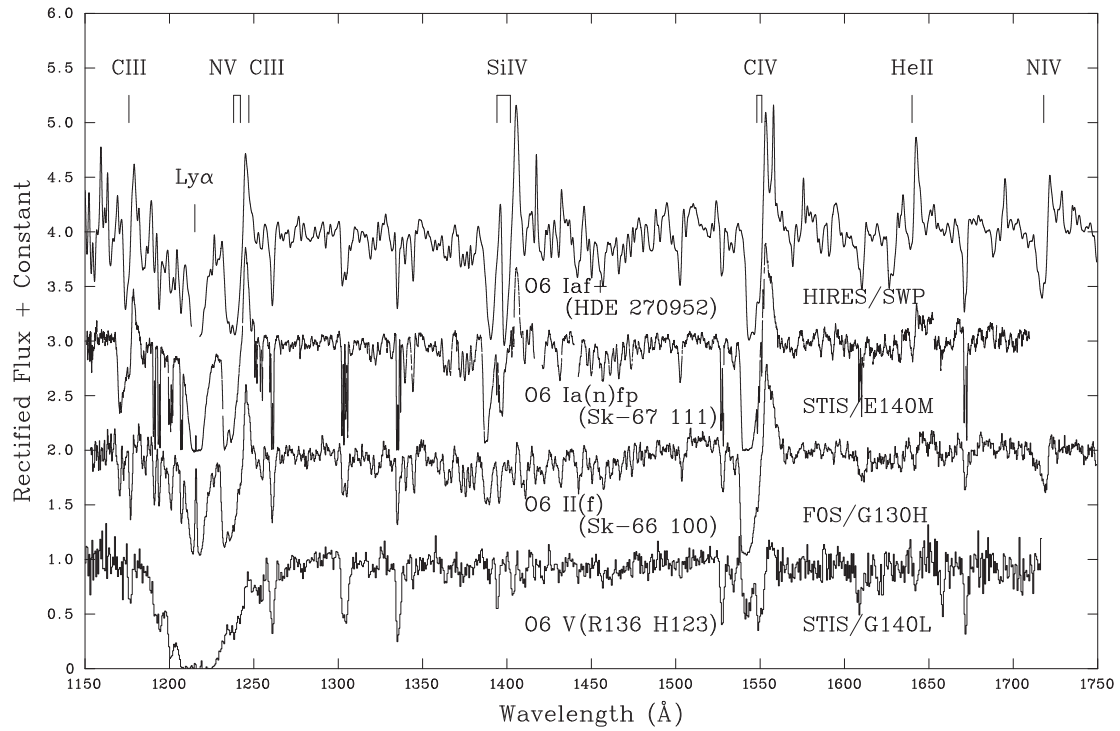
Figure A9. Montage of O6 luminosity sequence. C IV λλ1548–51 and N V λλ1238–42 exhibit a weak P Cygni profile for dwarfs, in contrast to strong P Cygni profiles at class II–I, with Si IV λλ1393–1402 also exhibiting saturated P Cygni profiles for supergiants. Narrow He II 1640 emission is also observed in supergiants.
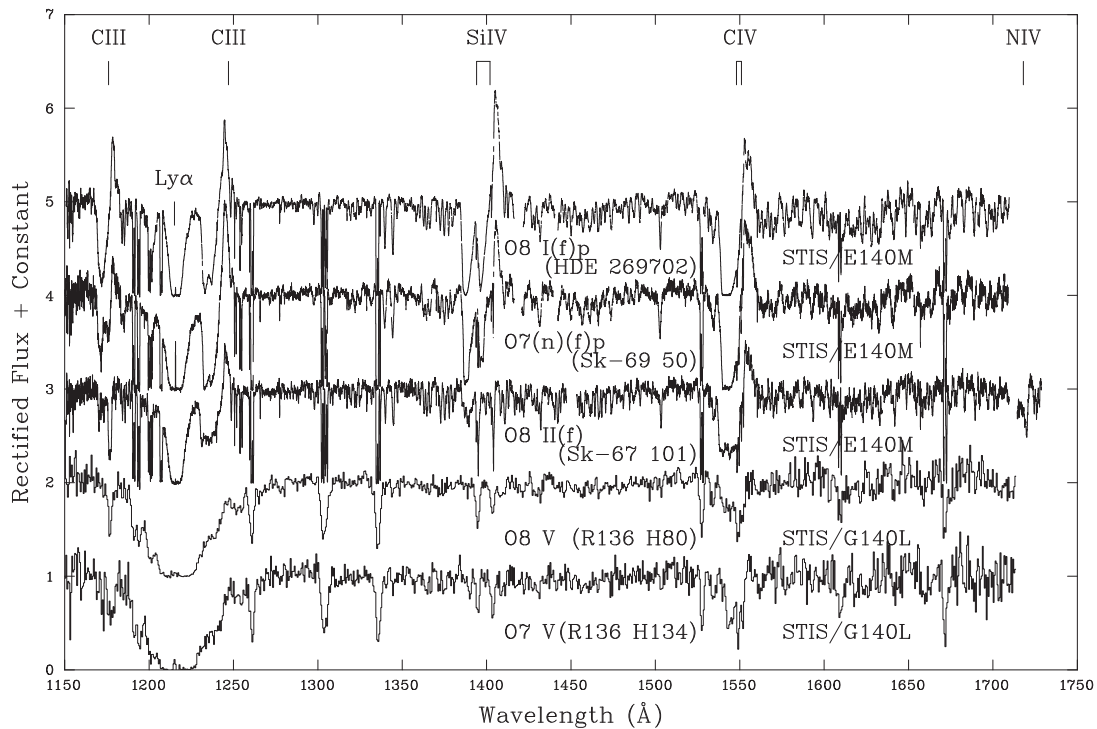
Figure A10. Montage of O7–8 luminosity sequence. C IV λλ1548–51 exhibits a narrow, weak P Cygni profile for dwarfs, with N V λλ1238–42 barely present. Both lines display a prominent P Cygni profile at Class II (unsaturated for N V), while Si IV λλ1393–1402 exhibit saturated P Cygni profiles amongst supergiants.
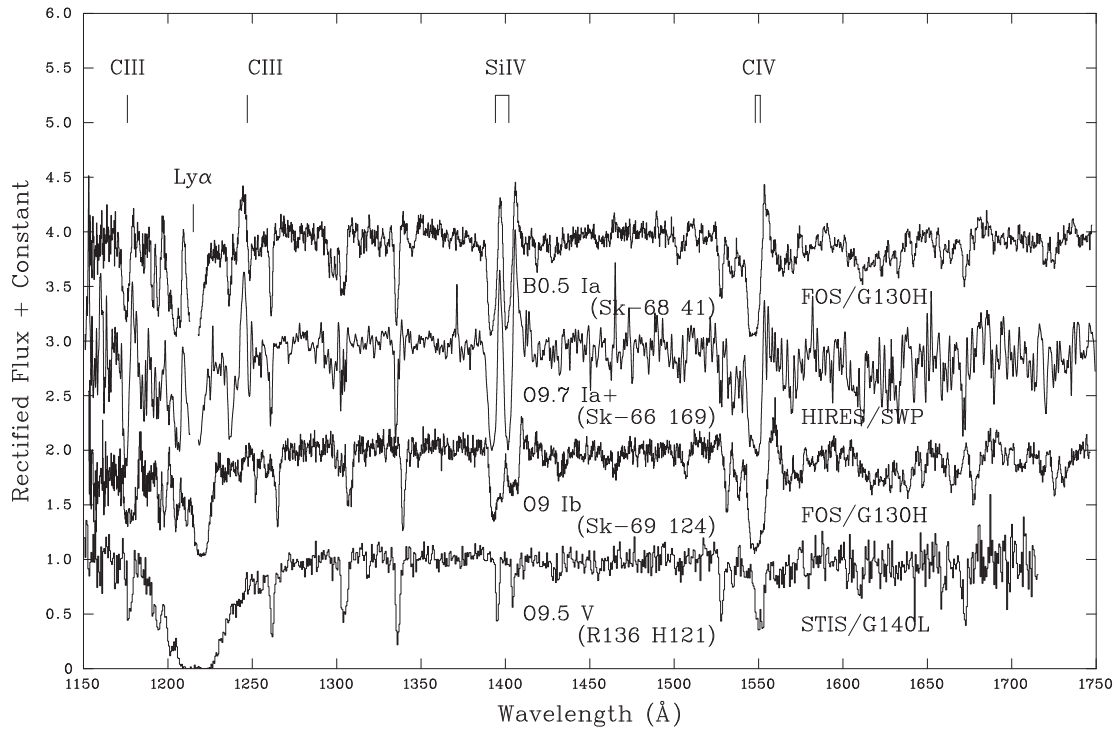
Figure A11. Montage of O9–B0.5 luminosity sequence. C IV λλ1548–51 is photospheric in dwarfs, N V λλ1238–42 absent, while C IV and Si IV λλ1393–1402 are saturated P Cygni profiles in luminous supergiants. C III λ1247 is also prominent in luminous supergiants.

APPENDIX B: ULTRAVIOLET ATLAS OF EARLY-TYPE STARS IN R136
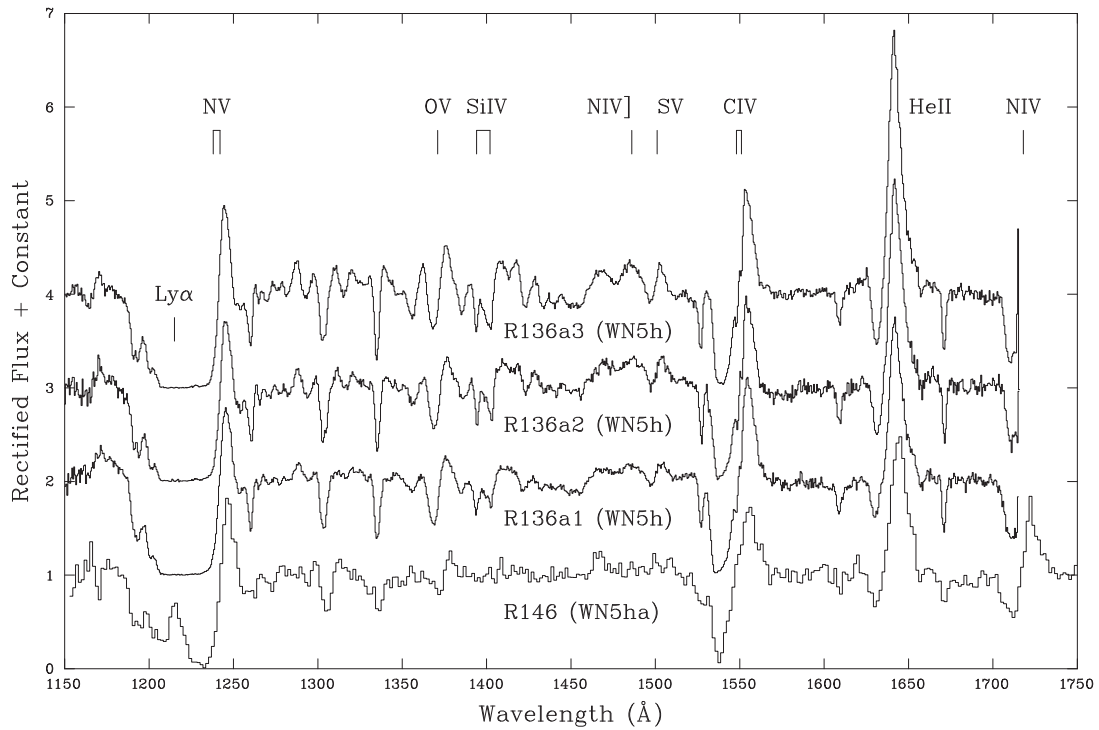
Figure B1. *HST*/STIS ultraviolet spectroscopy of WN stars in R136, together with an LMC template WN5 star R146 (Brey 88=BAT99-117, IUE SWP/LORES).
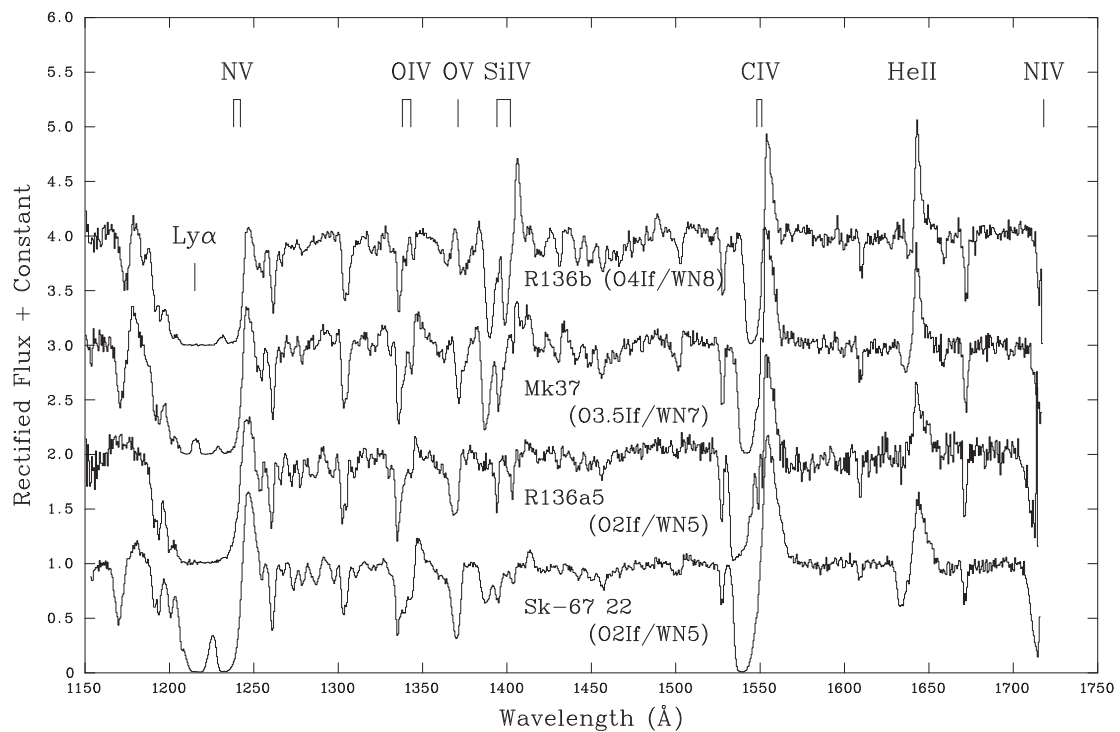
Figure B2. *HST*/STIS ultraviolet spectroscopy of Of/WN stars in R136, together with LMC templates Sk–67° 22 and Melnick 37 (see Table A1).
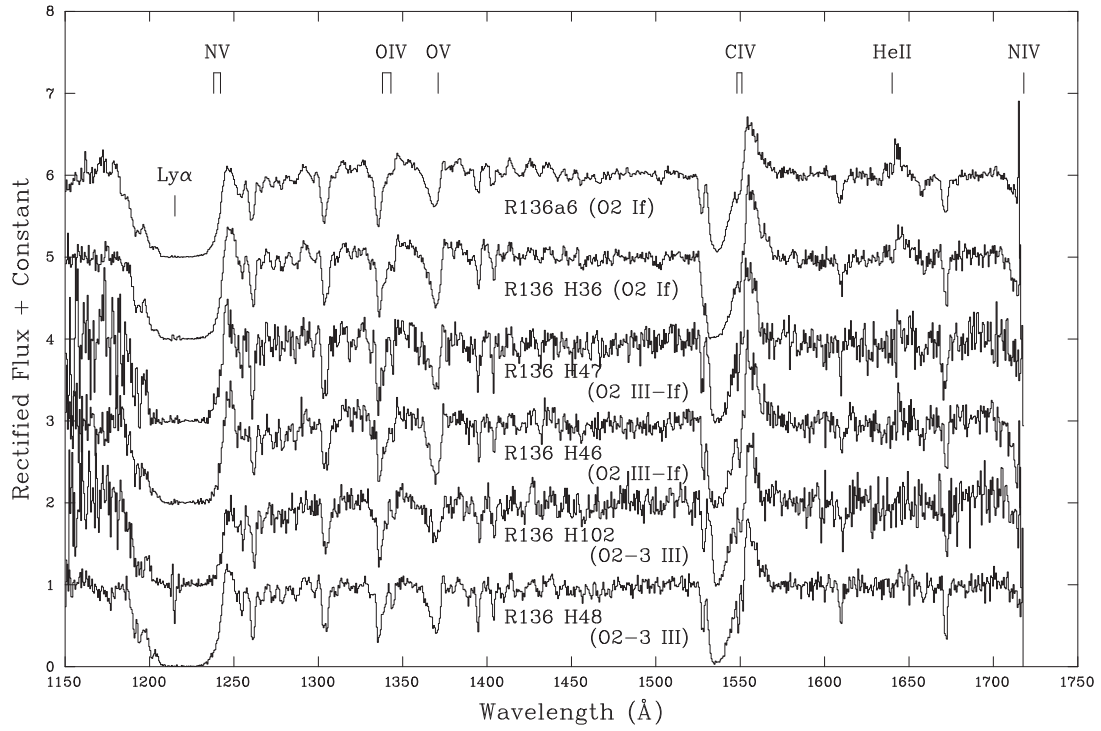
Figure B3. *HST*/STIS ultraviolet spectroscopy of O2–3 (super)giants in R136, together with LMC templates R136 H48 (O2–3 III) and H36 (O2 If), see Table A1.
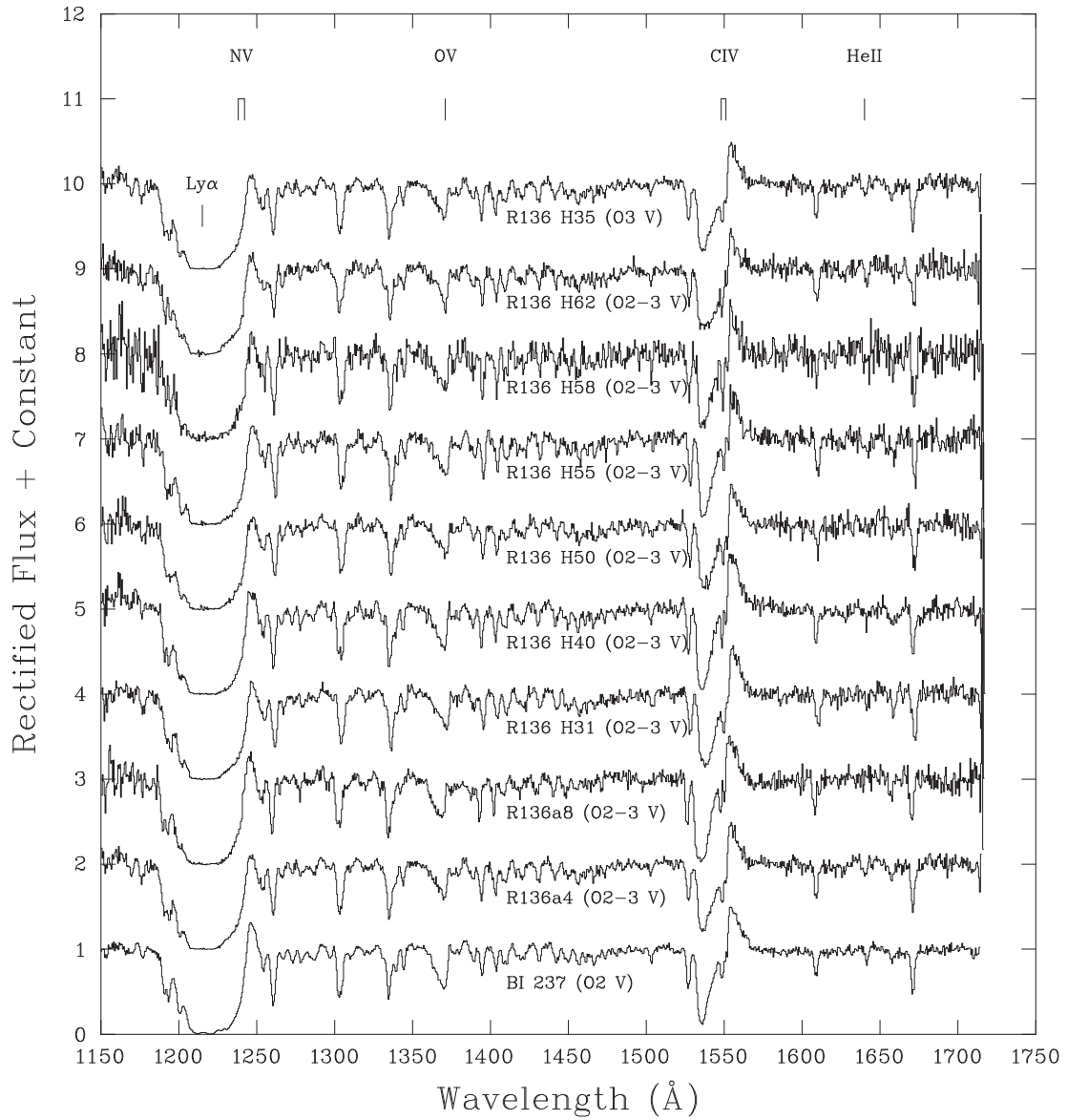
Figure B4. *HST*/STIS ultraviolet spectroscopy of O2–3 dwarfs in R136, together with templates BI 237 (O2 V) and R136 H35 (O3 V), see Table A1.
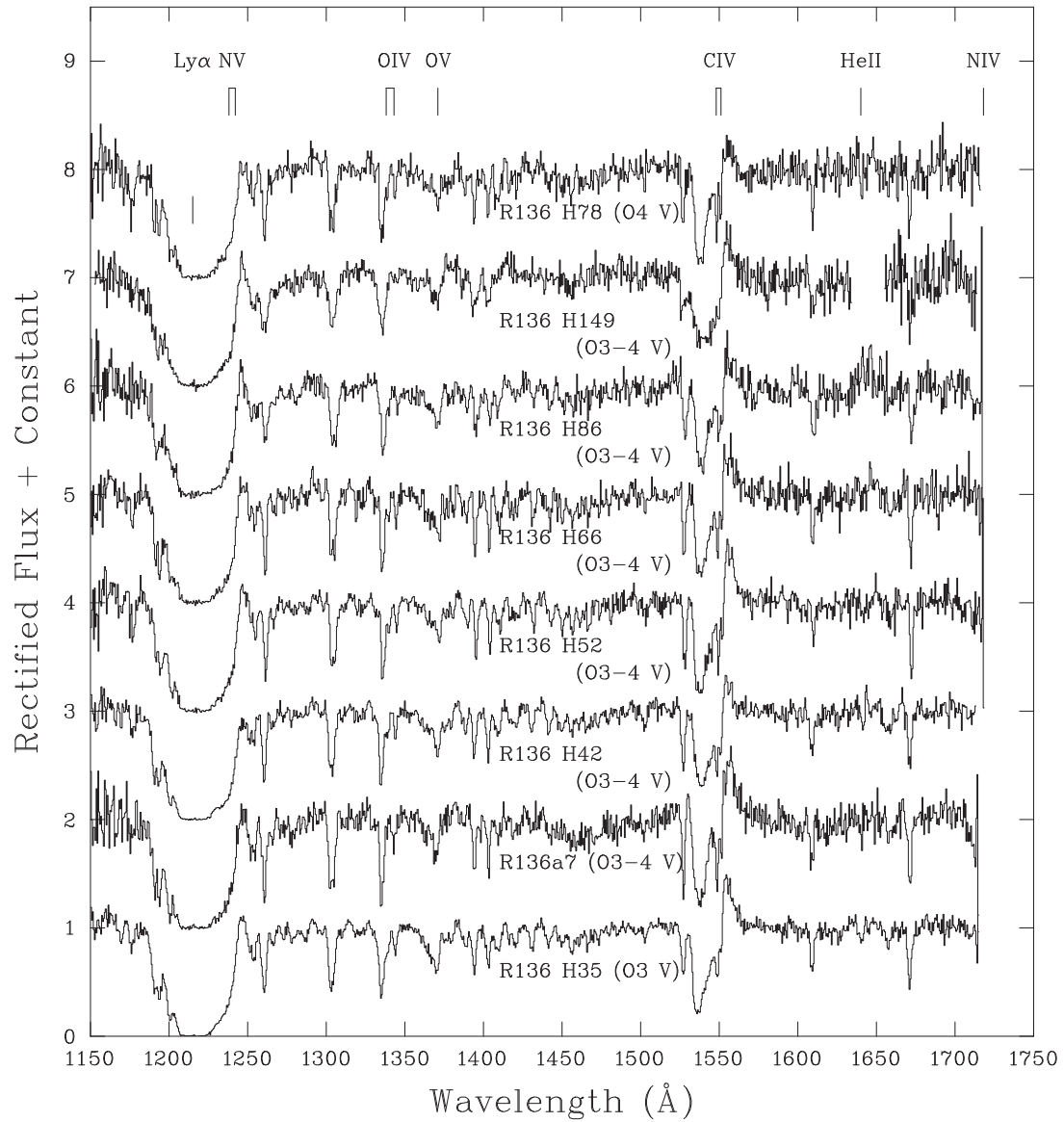
Figure B5. *HST*/STIS ultraviolet spectroscopy of O3–4 dwarfs in R136, together with LMC templates R136 H35 (O3 V) and H78 (O4 V); see Table A1.
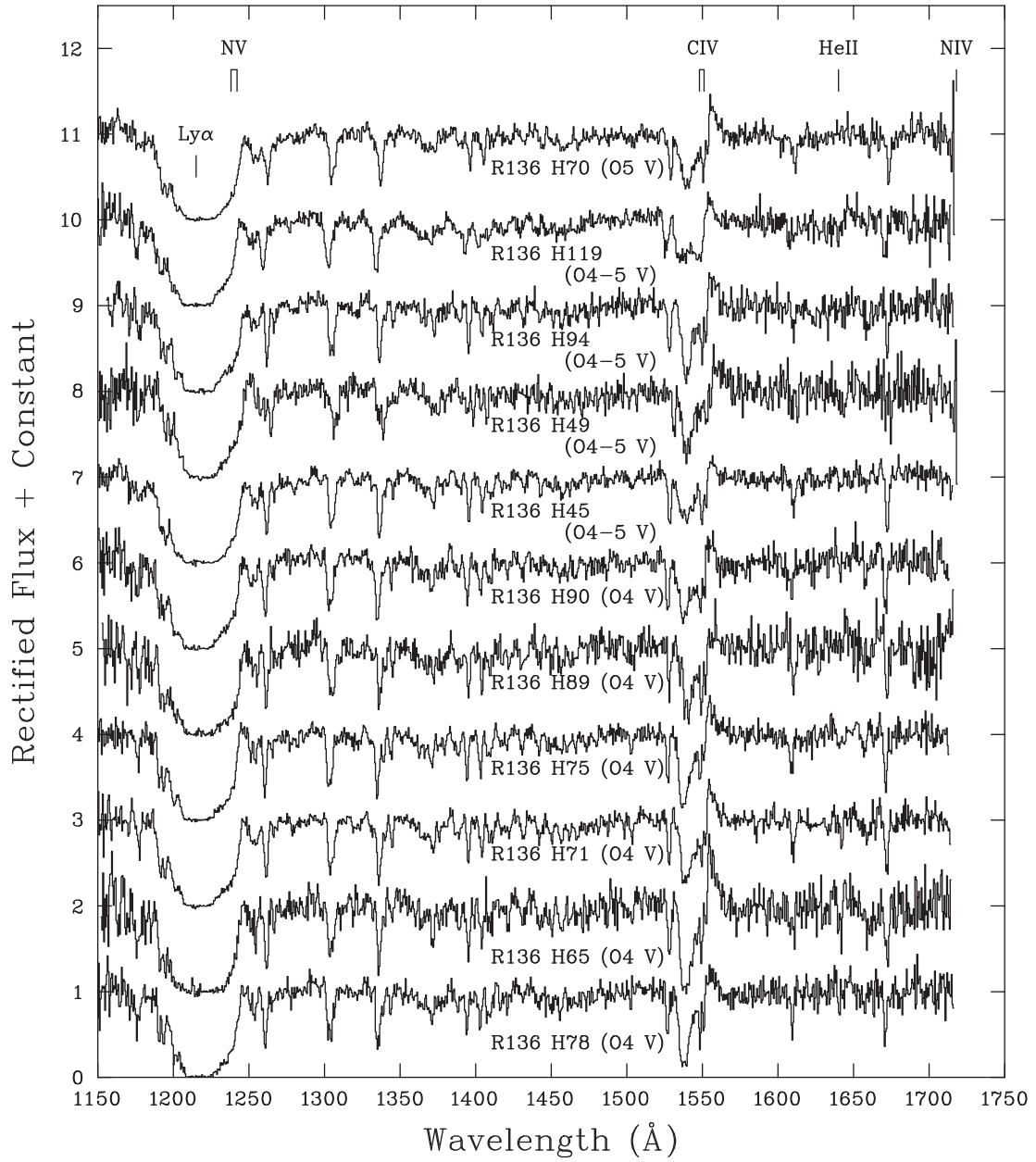
Figure B6. *HST*/STIS ultraviolet spectroscopy of O4–5 dwarfs in R136, together with LMC templates R136 H78 (O4 V) and H70 (O5 Vz); see Table A1.
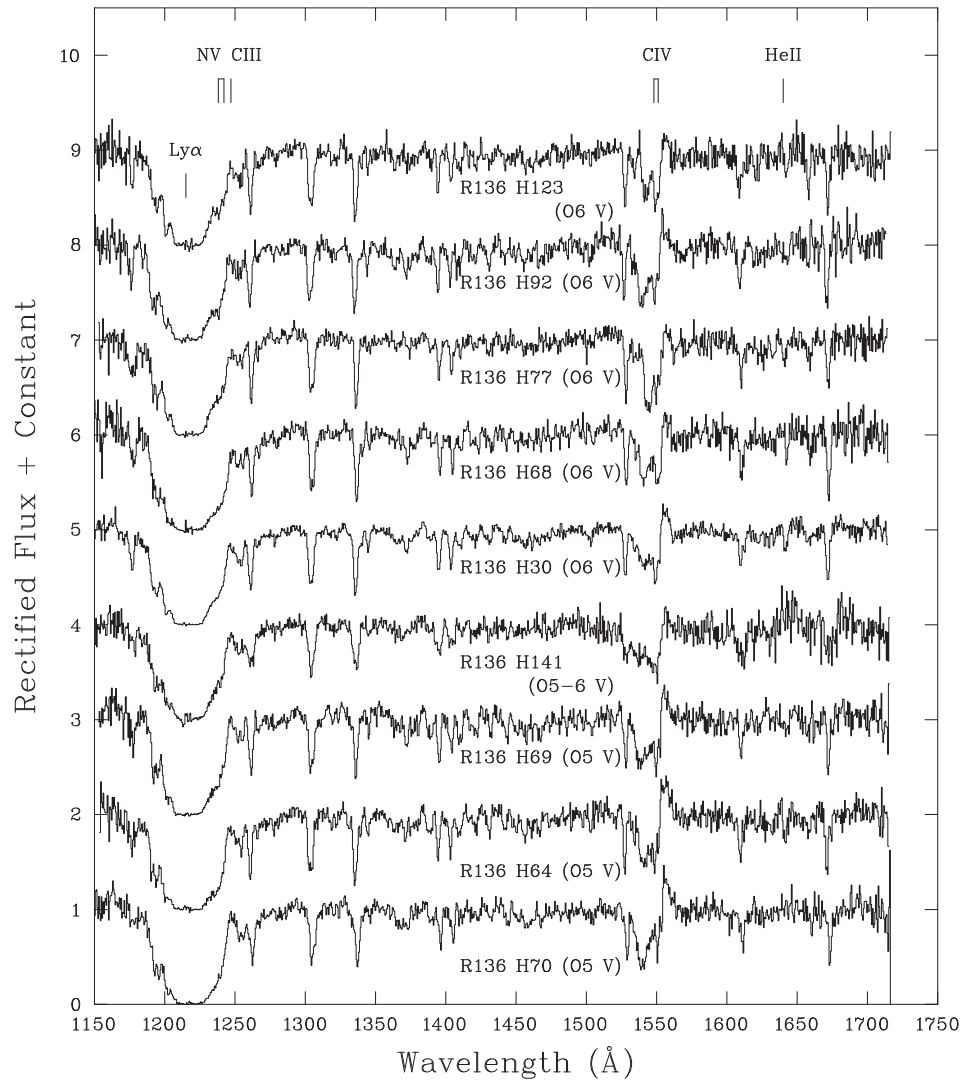
Figure B7. *HST*/STIS ultraviolet spectroscopy of O5–6 dwarfs in R136, together with LMC templates R136 H70 (O5 Vz) and H123 (O6 V); see Table A1.
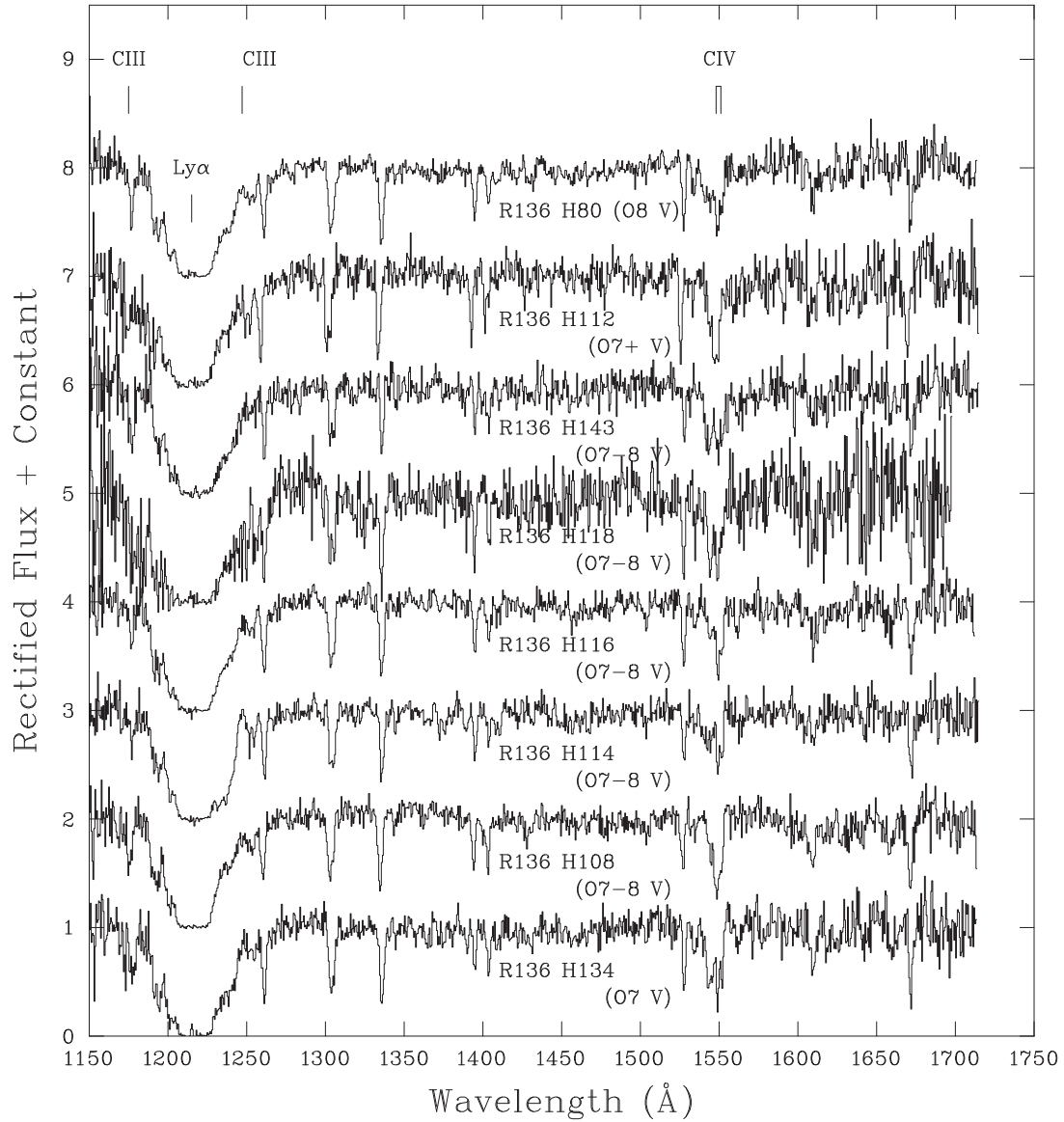
Figure B8. *HST*/STIS ultraviolet spectroscopy of O7–8 dwarfs in R136, together with LMC templates R136 H134 (O7 V) and H80 (O8 V); see Table A1.

Figure B9. *HST*/STIS ultraviolet spectroscopy of O9+ dwarfs in R136, together with LMC template R136 H121 (O9.5 V); see Table A1.

APPENDIX C: WIND VELOCITIES OF LMC O-TYPE STARS

Table C1. Comparison of terminal wind velocities (km s^{-1}) of LMC O stars in the present study (indicated with a colon if via v_{edge}) with literature values from far-UV spectroscopy (direct measurement or Sobolov with Exact Integral SEI approach).
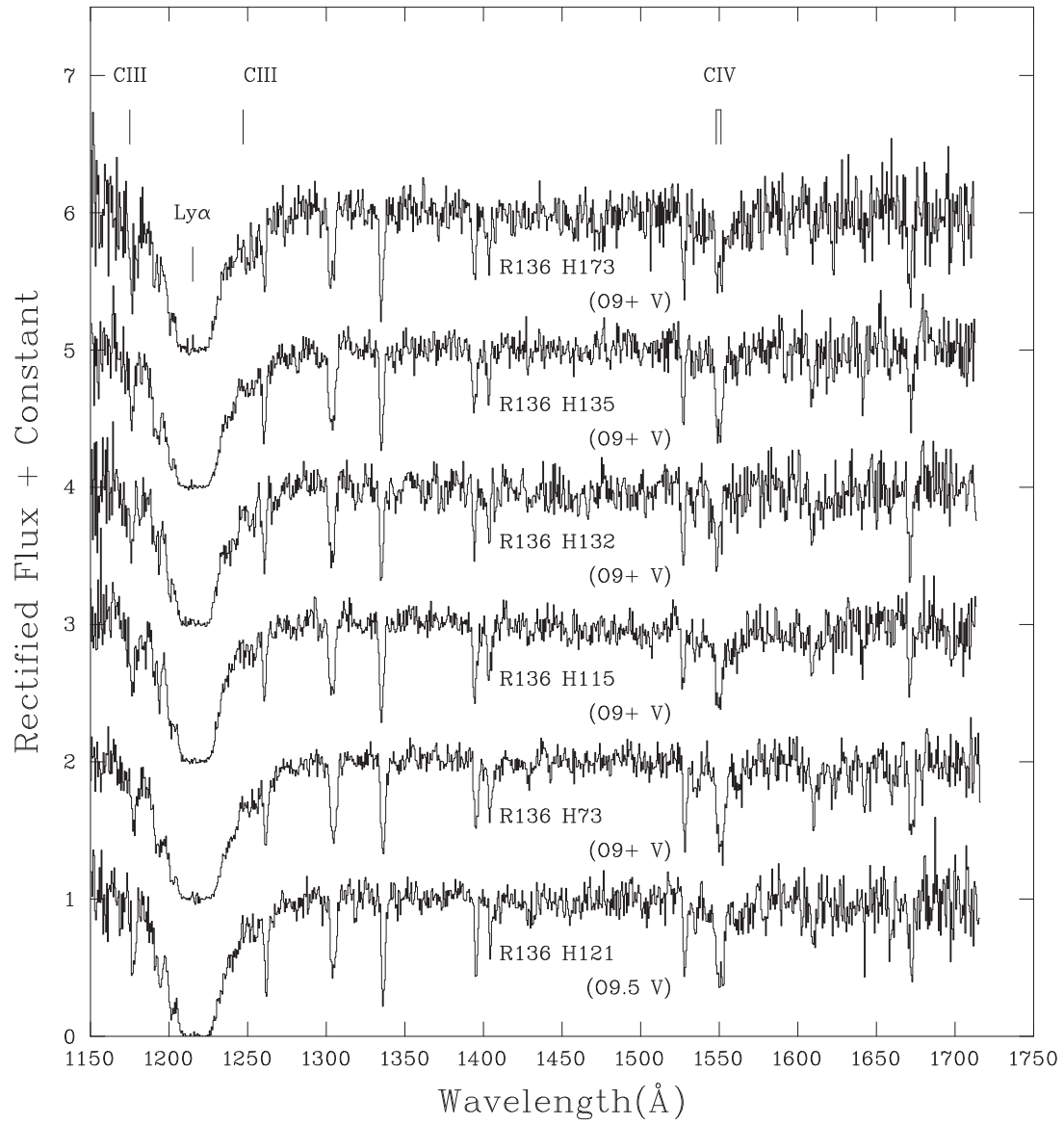
Star	Alias	Sp type	v_∞ (km s^{-1}) (this study)	Data set/diagnostic (this study)	v_∞ (km s^{-1})	Data set/diagnostic (literature)	Reference
BI 237		O2 V			3400	*HST* STIS/C IV	f
BI 253	VFTS 72	O2 V			3180	*HST* STIS/C IV	f
R136 H40		O2–3 V	2750	*HST* STIS/C IV	3400, 3000, 3400	*HST* GHRS/C IV	b, c, e
R136 H50		O2–3 V	2620	*HST* STIS/C IV	3125	*HST* GHRS/C IV	b
R136 H55		O2–3 V	2880	*HST* STIS/C IV	3150, 2955, 3250	*HST* GHRS/C IV	b, c, e
R136 H58		O2–3 V	2980	*HST* STIS/C IV	3050, 2840	*HST* GHRS/C IV	b, c
LH 101/W3-14		O3 V			3100	*HST* STIS/C IV	f
R136 H33		O3 V			3250	*HST* STIS/C IV	f
LH 101/W3-24		O3 V			2400	*HST* STIS/C IV	e
R136 H39		O3 V+O5.5 V			2900	*HST* GHRS/C IV	b
LH 81/W28-23		O3.5 V((f+))			3050	*HST* STIS/C IV	f
R136a7	R136 H24	O3–4 V	2710:	*HST* STIS/C IV	2900, 3100	*HST* GHRS/C IV	b, e
R136 H42		O3–4 V	2245	*HST* STIS/C IV	2850	*HST* GHRS/C IV	b
LH 81/W28-5		O4 V((f+))			2700	*HST* STIS/C IV	e
Sk–70° 60		O4–5 V((f))			2300	FUSE/SEI	d
LMC 054383		O4–5 V			2380	*HST* STIS/C IV	g
LH 58-496		O5 V(f)			2400	*HST* STIS/C IV	f
Sk–70° 69		O5.5 V((f))			2750	FUSE/SEI	d
BI 229		O7 V–III			1950	FUSE/SEI	d
Sk–67° 191		O8 V			1950	FUSE/SEI	d
HDE 269810	Sk–67° 211	O2 III(f)			3600	FUSE/SEI	d
Sk–66° 172		O2 III			3100	FUSE/SEI	d
Sk–70° 91	LH 62-1	O2 III			3150	FUSE/SEI	d
Sk—68° 137		O2 III			3400	*HST* FOS/SEI	a
LH 64–16		ON2 III			3250	*HST* STIS/C IV	g
VFTS 16		O2 III–If			3250	*HST* COS/SEI	h
R136 H46		O2 III–If	3440	*HST* STIS/C IV	3550, 3355	*HST* GHRS/C IV	b, c
R136 H47		O2 III–If	3045	*HST* STIS/C IV	3625, 3305, 3500	*HST* GHRS/C IV	b, c, e
R136 H18	Melnick 33S	O3 III			3200	*HST*/STIS/C IV	f
LH 90 ST2-22		O3.5 III(f+)			2560	*HST* STIS/C IV	f
Sk–67° 69		O4 III			2500	FUSE/SEI	d
HDE 269676	Sk–71° 45	O4–5 III			2500	FUSE/SEI	d
Sk–66° 100		O6 II(f)			2075	FUSE/SEI	d
BI 272		O7: III–II			3400	FUSE/SEI	d
Sk–67° 101	LH 54-21	O8 II(f)			2300	FUSE/SEI	d
BI 173		O8 II			2850	FUSE/SEI	d
LH 101/W3-19		O2 If			2850	*HST* STIS/C IV	f
Melnick 42	R136 H2	O2 If			2800	*HST* STIS/C IV	i
R136 H36		O2 If	3500	*HST* STIS/C IV	3640, 3700, 3750	*HST* GHRS/C IV	b, c, e
Sk–65° 47	LH 43–18	O4 I(n)f+p			2100	*HST* STIS/C IV	f
HDE 269698	Sk–67° 166	O4 If+			1900	*HST* FOS/SEI	a
Sk–67° 167	LH 76-21	O4 Inf+			2150	*HST* FOS/SEI	a
Sk–67° 111	LH 60-53	O6 Ia(n)fp var			2000	FUSE/SEI	d
HDE 270952	Sk–65° 22	O6 Iaf+			1350	FUSE/SEI	d
HDE 270145	Sk–70° 115	O6.5 Iaf			2200	FUSE/SEI	d
BI 170		O9.5 Ib			1700	FUSE/SEI	d
Sk–69° 124		O9 Ib			1600	FUSE/SEI	d
Sk–65° 21		O9.7 Iab			1700	FUSE/SEI	d
Sk–66° 169		O9.7 Ia+			800	FUSE/SEI	d
HDE 269896	Sk–68° 135	ON9.7 Ia+			1050	FUSE/SEI	d
HDE 268605	Sk–67° 05	O9.7 Ib			1400	FUSE/SEI	d
Sk–67° 22		O2 If/WN5			2650	*HST* STIS/C IV	f
R136a5	R136 H20	O2 If/WN5	3045	*HST* STIS/C IV	3000, 3400	*HST*/GHRS C IV	b, e
Melnick 39	R136 H7	O2.5 If/WN6			2100	*HST* STIS/C IV+Si IV	f
Melnick 37	R136 H14	O3.5 If/WN7			2000	*HST* STIS/C IV+Si IV	f
LH 90 Brey 58	AB4	O3.5 If/WN7			1900	*HST* STIS/Si IV	f

Notes. (a) Walborn et al. (1995); (b) de Koter et al. (1998); (c) Prinja & Crowther (1998); (d) Massa et al. (2003); (e) Massey et al. (2004); (f) Massey et al. (2005); (g) Massey et al. (2009); (h) Evans et al. (2010); (i) Bestenlehner et al. (2014).

APPENDIX D: ADDITIONAL R136 SOURCES

Table D1. *HST*/WFC3 photometry (de Marchi et al. 2011) for additional R136 sources brighter than $m_{F555W} = 17.0$ mag within a projected distance of 4.1 arcsec (1 parsec) from R136a1. Identifications are from Weigelt & Baier (1985, WB85) or Hunter et al. (1995, HSH95). A_{F555W} is calculated from observed colours for an adopted reddening law of $R_{5495} = 4.1$, and DM = 18.49 (Pietrzyński et al. 2013). F555W-band photometry shown in italics is from Hunter et al. (1995) offset by –0.17 mag (see Section 2.3). R136 H351 is included since it is one of the 70 far-UV brightest sources in R136a1.

HSH95 (WB85)	Sp type	Ref	r (arcsec)	m_{F555W} (mag)	$m_{F336W}-m_{F438W}$ (mag)	$m_{F438W}-m_{F555W}$ (mag)	$m_{F555W}-m_{F814W}$ (mag)	A_{F555W} (mag)	M_{F555W} (mag)	$10^{14}F_{1500}$ (erg s^{-1} cm^{-2} Å)	Slit
379			0.41	16.51 ± 0.05	-0.97 ± 0.06	0.01 ± 0.06	0.60 ± 0.08	1.87	-3.85	0.5 ± 0.1	SE2
235			0.50	*16.63*				1.72	-3.58	1.2 ± 0.1	SE2
210			0.54	*16.47*				1.72	-3.74	1.2 ± 0.1	NW3
378			0.56	16.06 ± 0.03				1.72	-4.15	1.0 ± 0.1	SE2
306			0.70	16.42 ± 0.05			0.33 ± 0.08	1.81	-3.88	0.5 ± 0.1	NW4
196			0.74	*16.36*				1.72	-3.85		NW5
231			0.88	16.66 ± 0.06	-1.23 ± 0.08	0.11 ± 0.08	0.34 ± 0.11	1.58	-3.41	0.4 ± 0.1	NW2
305			0.91	*16.96*				1.72	-3.25		NW4
291			0.94	16.67 ± 0.05	-1.20 ± 0.07	0.16 ± 0.07	0.42 ± 0.08	1.72	-3.54	0.4 ± 0.1	SE4
259			1.00	*16.75*				1.72	-3.46	0.4 ± 0.1	NW5
217			1.01	16.52 ± 0.04	-1.36 ± 0.06	0.18 ± 0.06		1.48	-3.45	0.5 ± 0.1	NW1
274			1.06	16.87 ± 0.07			0.29 ± 0.12	1.72	-3.34	0.4 ± 0.1	NW4
187			1.07	16.16 ± 0.03	-1.31 ± 0.04	0.11 ± 0.05	0.27 ± 0.05	1.44	-3.77	1.0 ± 0.1	SE4
203			1.21	16.33 ± 0.04	-1.27 ± 0.06	0.17 ± 0.06	0.32 ± 0.07	1.61	-3.77	0.6 ± 0.1	NW3
233			1.24	16.76 ± 0.05	-1.25 ± 0.08	0.15 ± 0.08	0.32 ± 0.09	1.61	-3.34	0.3 ± 0.1	SE2
293			1.26	16.99 ± 0.07	-1.03 ± 0.11	0.17 ± 0.10	0.30 ± 0.11	2.05	-3.55	0.3 ± 0.1	NW7
159			1.34	16.14 ± 0.03	-1.24 ± 0.04	0.10 ± 0.04	0.33 ± 0.04	1.65	-4.00	0.7 ± 0.1	SE6
176			1.35	16.14 ± 0.03	-1.36 ± 0.04	0.13 ± 0.04	0.22 ± 0.05	1.36	-3.71	0.9 ± 0.1	NW7
179			1.40	16.23 ± 0.03	-1.31 ± 0.05	0.13 ± 0.05		1.47	-3.73	0.9 ± 0.1	NW6
254			1.43	16.87 ± 0.05	-1.25 ± 0.08	0.10 ± 0.08	0.32 ± 0.09	1.51	-3.13	0.5 ± 0.1	NW3
302			1.48	16.98 ± 0.06	-1.28 ± 0.09	0.10 ± 0.09	0.18 ± 0.12	1.47	-2.98	0.9 ± 0.1	NW8
223			1.53	16.61 ± 0.04	-1.30 ± 0.06	0.15 ± 0.06	0.26 ± 0.07	1.51	-3.39	0.6 ± 0.1	NW2
285			1.58	16.82 ± 0.05	-1.23 ± 0.08	0.17 ± 0.07	0.53 ± 0.08	1.72	-3.39	0.4 ± 0.1	NW2
288			1.62	16.80 ± 0.04	-1.18 ± 0.06	0.13 ± 0.06	0.29 ± 0.07	1.69	-3.38		–
281			1.63	16.71 ± 0.04	-1.21 ± 0.06	0.14 ± 0.05	0.39 ± 0.06	1.65	-3.43	0.5 ± 0.1	SE1
139			1.65	16.02 ± 0.02			0.22 ± 0.04	1.72	-4.19	1.1 ± 0.1	SE3
162			1.72	*16.06*				1.72	-4.15	0.8 ± 0.1	SE2
386			1.75	16.87 ± 0.05	-0.97 ± 0.09	0.12 ± 0.07	0.36 ± 0.08	2.07	-3.69	0.2 ± 0.1	NW4
311			1.78	16.87 ± 0.05	-0.97 ± 0.08	0.12 ± 0.07	0.36 ± 0.08	2.07	-3.69	0.3 ± 0.1	NW4
211			1.78	16.52 ± 0.03	-1.31 ± 0.04	0.07 ± 0.04	0.22 ± 0.06	1.72	-3.69		–
181			1.87	*16.17*				1.72	-4.04	0.7 ± 0.1	NW1
240			2.11	*16.66*				1.72	-3.55		–
237			2.18	16.66 ± 0.03	-1.04 ± 0.04	0.09 ± 0.04	0.30 ± 0.05	1.90	-3.73		–
416			2.20	16.95 ± 0.04	-0.90 ± 0.06	0.11 ± 0.05	0.44 ± 0.06	2.18	-3.72		–
213			2.23	16.68 ± 0.03	-1.10 ± 0.05	0.12 ± 0.05	0.36 ± 0.05	1.83	-3.64		–
253			2.30	16.89 ± 0.04	-1.27 ± 0.05	0.14 ± 0.05	0.27 ± 0.06	1.56	-3.16		–
392			2.33	16.73 ± 0.03	-1.11 ± 0.07	0.07 ± 0.07	0.46 ± 0.06	1.72	-3.48	0.3 ± 0.1	SE8
205			2.37	16.37 ± 0.02	-1.22 ± 0.03	0.19 ± 0.03	0.46 ± 0.03	1.75	-3.87		–
258			2.39	16.74 ± 0.03		0.17 ± 0.05	0.44 ± 0.05	1.72	-3.47		–
189			2.42	16.31 ± 0.02	-1.23 ± 0.03	0.18 ± 0.03	0.32 ± 0.03	1.72	-3.89	1.0 ± 0.2	SE8
97			2.42	15.46 ± 0.01	-1.31 ± 0.02	0.18 ± 0.02	0.34 ± 0.02	1.76	-4.79		–
87			2.47	15.25 ± 0.01	-1.32 ± 0.01	0.13 ± 0.01	0.32 ± 0.02	1.65	-4.89		–
145			2.47	16.10 ± 0.01	-1.30 ± 0.02	0.10 ± 0.02	0.28 ± 0.03	1.42	-3.81	0.8 ± 0.1	NW2
547			2.51	16.75 ± 0.03			0.64 ± 0.04	1.72	-3.46		–
255			2.55	16.77 ± 0.03	-1.17 ± 0.04	0.18 ± 0.04	0.48 ± 0.04	1.81	-3.53		–
267			2.60	16.90 ± 0.02	-1.19 ± 0.03	0.12 ± 0.03	0.27 ± 0.04	1.68	-3.27		–
206			2.63	16.53 ± 0.02		0.16 ± 0.03	0.23 ± 0.04	1.72	-3.68		–
127			2.67	15.94 ± 0.02	-1.33 ± 0.02	0.11 ± 0.02	0.30 ± 0.03	1.59	-4.15		–
177			2.80	16.26 ± 0.02	-1.18 ± 0.02	0.26 ± 0.02	0.52 ± 0.03	1.94	-4.17	0.4 ± 0.1	NW5
33	O3 V	b	2.80	14.36 ± 0.01	-1.36 ± 0.01	0.06 ± 0.01	0.28 ± 0.01	1.45	-5.58		–
251			2.81	16.83 ± 0.02		0.13 ± 0.03		1.72	-3.38		–
184			2.82	16.40 ± 0.02	-1.32 ± 0.02	0.17 ± 0.02	0.29 ± 0.03	1.52	-3.61		–
294			2.86	17.00 ± 0.03	-1.24 ± 0.04	0.17 ± 0.04	0.46 ± 0.04	1.67	-3.16		–
236			2.90	16.73 ± 0.02	-1.24 ± 0.03	0.13 ± 0.03	0.35 ± 0.04	1.59	-3.35		–
241			2.92	16.80 ± 0.02			0.17 ± 0.04	1.72	-3.41		–

Table D1 *– continued*

HSH95 (WB85)	Sp type	Ref	r (arcsec)	m_{F555W} (mag)	$m_{F336W}-m_{F438W}$ (mag)	$m_{F438W}-m_{F555W}$ (mag)	$m_{F555W}-m_{F814W}$ (mag)	A_{F555W} (mag)	M_{F555W} (mag)	$10^{14}F_{1500}$ (erg s^{-1} cm^{-2} Å)	Slit
272			2.93	16.95 ± 0.02	-1.08 ± 0.04	0.21 ± 0.04	0.54 ± 0.04	2.03	-3.57		–
170			2.97	16.25 ± 0.01	-1.23 ± 0.02	0.07 ± 0.02	0.33 ± 0.03	1.50	-3.74		–
216			2.99	16.60 ± 0.01	-1.23 ± 0.02	0.10 ± 0.02	0.27 ± 0.03	1.55	-3.44		SE7
222			3.06	16.71 ± 0.02	-1.15 ± 0.03	0.22 ± 0.03	0.55 ± 0.03	1.92	-3.70	0.1:	SE8
250			3.09	16.95 ± 0.02	-1.09 ± 0.02	0.22 ± 0.03	0.46 ± 0.03	2.04	-3.58	0.2 ± 0.1	NW1
277			3.22	16.96 ± 0.02	-1.13 ± 0.03	0.25 ± 0.03	0.62 ± 0.03	2.01	-3.54	0.2 ± 0.1	SE6
317			3.27	16.25 ± 0.02	-1.50 ± 0.02	0.63 ± 0.02		2.03	-4.27		–
120			3.29	15.88 ± 0.01	-1.23 ± 0.02	0.05 ± 0.02	0.32 ± 0.02	1.65	-4.26	1.1 ± 0.1	SE4
10 (c)	WN5h	a	3.44	13.43 ± 0.01	-1.20 ± 0.02	0.31 ± 0.01	0.82 ± 0.01	2.33	-7.39		–
128			3.52	16.00 ± 0.01	-1.28 ± 0.01	0.07 ± 0.02	0.28 ± 0.02	1.41	-3.90		–
136			3.64	15.96 ± 0.01	-1.15 ± 0.02	0.23 ± 0.02	0.62 ± 0.02	1.94	-4.47		–
150			3.74	16.11 ± 0.01	-1.30 ± 0.02	0.16 ± 0.02	0.32 ± 0.02	1.54	-3.92		–
165			3.81	16.16 ± 0.01	-1.27 ± 0.02	0.18 ± 0.02	0.35 ± 0.02	1.63	-3.98		–
57			3.87	14.80 ± 0.01	-1.16 ± 0.01	0.26 ± 0.01	0.66 ± 0.01	2.17	-5.86		–
197			4.00	16.38 ± 0.01	-1.17 ± 0.02	0.13 ± 0.02	0.45 ± 0.02	1.72	-3.83		–
183			4.07	16.33 ± 0.01	-1.26 ± 0.02	0.24 ± 0.02	0.49 ± 0.02	1.76	-3.92		–
140			4.09	15.99 ± 0.01	-1.29 ± 0.02	0.11 ± 0.02	0.26 ± 0.02	1.47	-3.97		–
246			4.11	16.75 ± 0.01	-1.36 ± 0.02	0.12 ± 0.02	0.15 ± 0.02	1.36	-3.10		–
351			0.55	*17.18*				1.72	-3.03	0.5 ± 0.1	SE2

Notes. (a) Crowther & Dessart (1998); (b) Massey et al. (2005).

[1] *Department of Physics and Astronomy, University of Sheffield, Sheffield S3 7RH, UK*

[2] *Space Telescope Science Institute, 3700 San Martin Drive, Baltimore, MD 21218, USA*

[3] *Department of Physics, University of California, Davis, 1 Shields Ave, Davis, CA 95616, USA*

[4] *Centro de Astrobiologiá, CSIC/INTA, Campus ESAC, Apartado Postal 78, E-28 691 Villanueva de la Cañada, Madrid, Spain*

[5] *Department of Physics, University of Oxford, Denys Wilkinson Building, Keble Road, Oxford OX1 3RH, UK*

[6] *Argelanger-Institut für Astronomie der Universität Bonn, Auf dem Hügel 71, D-53121 Bonn, Germany*

[7] *Department of Physics, University of Warwick, Gibbet Hill Rd, Coventry CV4 7AL, UK*

[8] *Institute for Astrophysics, Tuerkenschanzstr. 17, A-1180 Vienna, Austria*

[9] *Institute of Astronomy and Astrophysics, National Observatory of Athens, I. Metaxa and Vas. Pavlou St, P. Penteli 15236, Greece*

[10] *Astronomical Institute Anton Pannekoek, University of Amsterdam, Kruislaan 403, NL-1098 SJ, Amsterdam, the Netherlands*

[11] *Institute of Astronomy, KU Leuven, Celestijnenlaan 200 D, B-3001 Leuven, Belgium*

[12] *UK Astronomy Technology Centre, Royal Observatory Edinburgh, Blackford Hill, Edinburgh EH9 3HJ, UK*

[13] *Armagh Observatory, College Hill, Armagh BT61 9DG, UK*

[14] *Instituto de Astrofísica de Canarias, E-38200 La Laguna, Tenerife, Spain*

[15] *Departamento de Astrofísica, Universidad de La Laguna, E-38205 La Laguna, Tenerife, Spain*

[16] *Department of Physics and Astronomy, University College London, Gower St, London WC1E 6BT, UK*

[17] *European Space Astronomy Centre, ESA, Villanueva de la Cañada, Madrid, Spain*

[18] *Uiniversitäts-Sternwarte, Scheinerstrasse 1, D-81679 München, Germany*

This paper has been typeset from a TEX/LATEX file prepared by the author.